Computational Relativistic Electrodynamics: New Algorithms, Parallel Software, and Applications to Accelerator Design

A Dissertation Presented

by

Kwang Min Yu

to

The Graduate School

in Partial Fulfillment of the Requirements

for the Degree of

Doctor of Philosophy

in

Applied Mathematics and Statistics

Stony Brook University

May 2016

Stony Brook University

The Graduate School

Kwang Min Yu

We, the dissertation committee for the above candidate for the
Doctor of Philosophy degree, hereby recommend
acceptance of this dissertation.

Roman V. Samulyak - Dissertation Advisor
Professor, Department of Applied Mathematics and Statistics

James Glimm - Chairperson of Defense
Distinguished Professor, Department of Applied Mathematics and Statistics

Xiangmin Jiao - Member
Associate Professor, Department of Applied Mathematics and Statistics

Meifeng Lin - Outside Member
Assistant Computational Scientist, Brookhaven National Laboratory

This dissertation is accepted by the Graduate School.

Charles Taber
Dean of the Graduate School

Abstract of the Dissertation

Computational Relativistic Electrodynamics: New Algorithms, Parallel Software, and Applications to Accelerator Design

by

Kwang Min Yu

Doctor of Philosophy

in

Applied Mathematics and Statistics

Stony Brook University

2016

A parallel, fully relativistic, 3D electromagnetic particle-in-cell (EM-PIC) code, named SPACE, has been developed for the simulation of relativistic particle beams, beam - plasma interaction, and plasma chemistry. New algorithms such as atomic processes in plasma, proper boundary conditions, and an efficient method for highly-relativistic beams in non-relativistic plasma have been developed. Algorithms for atomic process include ionization of neutral atoms by electron impact, recombination of plasma, and electron attachment on dopants in dense neutral gases. The code has been used for the simulation of processes in high-pressure radio-frequency (RF) cavity (HPRF) program at

Fermilab. Advanced numerical simulations resolve all physically relevant processes in RF cavity filled with high-pressure gases and interacting with proton beams. Simulations also support broader research on the design of muon cooling devices. From simulation studies of microphysics processes, macroscopic and experimentally measurable quantities have been derived. Through comparison with experiments in the MTA, simulations quantified several uncertain values of plasma properties such as effective recombination rates and the attachment time of electrons to dopant molecules. Simulations have achieved very good agreement with experiments on plasma loading and related processes. The experimentally validated code SPACE will be used for simulations of muon cooling devices in regimes beyond current experimental capabilities. In addition, the code is used to study advanced coherent electron cooling (ACeC) for the e-RHIC project at BNL. Simulations study the modulation effect of highly relativistic ions of gold on co-propagating electron plasma and the amplification of modulation. Parallel simulations were able to track every real electron in physically relevant domains.

DEDICATED
to

My Parents
My Wife Eunsuk
Inhye and Insang

Table of Contents

List of Figures

List of Tables

Acknowledgements

First and foremost, I would like to express my sincere appreciation and thanks to my advisor Doctor Roman V. Samulyak for the continuous support of my Ph.D study, for his motivation, and for his insightful and prospective ideas. His guidance was essential to me in all the time of research and writing of this thesis. His advice on my research as well as on my career has been irreplaceable.

Besides my advisor, I would like to appreciate Doctor James Glimm, Doctor Xingmin Jiao, and Doctor Meifen Lin, for being on my dissertation committee. My sincere gratitude also goes to Mr. Nicholas D'Imperio, chair of the Computational Sciences Laboratory, who provided me an opportunity to join the Computational Science Initiative in Brookhaven National Laboratory and to do research on high performance computing which is an important part of my PH.D study. I thank to my colleague Jun Ma. His limitless effort for research inspires me during our collaboration.

Throughout my academic career and life, ceaseless support of my parents and my wife, Eunsuk, has always motivated me to go forward and helped me to enjoy my work. Without Eunsuk, I could never have been able to be granted my Ph.D degree. My dissertation is dedicated to them.

Chapter 1

Introduction

Particle methods for the simulation of electrodynamic systems are used for a wide range of problems occurring in high energy and nuclear physics, laser and plasmas physics. In particle accelerators, various versions of the Particle-in-Cell (PIC) method are used. In order to resolve collective effects of particle beams such as the space charge, electrostatic approximation can be made in the beam frame. The corresponding electrostatic PIC methods require solving elliptic (Poisson) equations that often involve complex geometries and adaptive meshes. For complex particle dynamics and their interaction with other beams, external fields, or matter, electrostatic approximation is impossible. Therefore solving the full system of Maxwell equations (hyperbolic PDE's) coupled with particles is necessary. The need to resolve the long term dynamics places special requirements on conservative and symplectic properties of algorithms. In laser or plasma physics, particle methods are used when continuum models fail due to discrete properties of matter on small scales. This research deals with particle methods coupled with hyperbolic and elliptic partial differential equation's problems.

Direct numerical simulation of plasma in the presence of atomic processes such as formation of plasma from neutral and recombination of plasma is a complex multi-scale problem. Plasma number density may change by orders of magnitude during relevant time scales, creating difficulties in representing secondary plasma particles by macroparticles within the Particle-in-Cell (PIC) method. Another difficulty is in the presence of different time scale, as in the case of plasmas interacting with relativistic particle beams. Evolution of atomic physics processes may be orders of magnitude longer compared to passing times of short relativistic bunches. Novel algorithms for the simulation of plasma undergoing atomic processes and relativistic particle beams have been developed and implemented in SPACE, a parallel 3D electromagnetic PIC code. The SPACE code uses known state-of-art algorithms for computational electromagnetism, complements them with our new methods for plasma chemistry and relativistic processes, and implements them in scalable parallel software optimized for modern multi-core supercomputers. The code has been applied to a number of problems relevant to advanced particle cooling mechanisms such as coherent electron cooling at BNL [1] and muon cooling by high pressure RF cavity (HPRF) at Fermilab [2].

Chapter 2

Review of Particle-in-Cell Method

The Particle-in-Cell (PIC) method [3] is a hybrid particle - mesh technique for solving partial differential equations, in particular Vlasov-Maxwell and Vlasov-Poisson problems for the evolution of the density distribution function for matter (plasma, particle beam etc.), coupled to electromagnetic fields. In the PIC method, the density distribution function is discretized using a particle distribution. The force acting on the particles is computed simultaneously using Eulerian mesh points.

In a system of particles interacting with a field, the field is solved by Eulerian mesh and particle dynamics is solved in mesh free Lagrangian frame. When the motion is affected by its background field and the motion also affects to the field, the field evolution should be taken into account. The field computation is done by mesh grid.

Especially, a collisionless plasma is described by the Vlasov equation

$$\frac{\partial f_s}{\partial t} + \mathbf{v} \cdot \frac{\partial f_s}{\partial \mathbf{x}} + \frac{q_s}{m_s}(\mathbf{E} + \mathbf{v} \times \mathbf{B}) \cdot \frac{\partial f_s}{\partial \mathbf{v}} = 0 \tag{2.1}$$

where f_s denotes a charge distribution function of species s in six-dimensional phase space with the spacial coordinate $\mathbf{x}$ and the velocity coordinate $\mathbf{v}$. That is, $f_s = f_s(\mathbf{x}, \mathbf{v}, t)$. Also, q_s, m_s, $\mathbf{E}$, and $\mathbf{B}$ are charge of species s, mass of species s, electric field intensity, and magnetic flux density, respectively. Here, the Vlasov equation can be written as following:

$$\frac{D}{Dt} f_s(\mathbf{x}(t), \mathbf{v}(t), t) = \frac{\partial f_s}{\partial t} + \frac{d\mathbf{x}}{dt} \cdot \frac{\partial f_s}{\partial \mathbf{x}} + \frac{d\mathbf{v}}{dt} \cdot \frac{\partial f_s}{\partial \mathbf{v}} = 0 \tag{2.2}$$

where $\frac{d\mathbf{x}}{dt} = \mathbf{v}$, $\frac{d\mathbf{x}}{dt} = \frac{q_s}{m_s}(\mathbf{E} + \mathbf{v} \times \mathbf{B})$. This equation means the total derivative of f_s is constant along the characteristic curve when charge densities move by Newton-Lorentz equation.

The PIC method solves charge density and current density rather than solving directly the Vlasov equation. The charge density ρ and the current density $\mathbf{J}$ are described by the charge distribution f_x as following:

$$\rho(\mathbf{x}, t) = \sum_s q \int f_s d\mathbf{v} \tag{2.3}$$

and

$$\mathbf{J}(\mathbf{x}, t) = \sum_s q \int \mathbf{v} f_s d\mathbf{v}. \tag{2.4}$$

The charge density is coupled with Poisson's equation

$$\nabla \cdot \mathbf{E} = \frac{\rho}{\epsilon_0} \tag{2.5}$$

and the current density is coupled with the Ampère's law

$$\nabla \times \mathbf{B} = \mu_0 \mathbf{J} + \frac{1}{c^2}\frac{\partial \mathbf{E}}{\partial t} \tag{2.6}$$

where ϵ_0, μ_0, and c denote the permittivity of free space, the permeability of free space, and the light speed, respectively.

Therefore, the Vlasov equation can be solved by solving both the Maxwell's equations and the Newton-Lorentz equation. In PIC method, the charge density and current density are represented by macroparticles. Each macroparticle usually represents a number of particles that belongs to the same species, which means a particle in the PIC method represents a number of particles having same mass and electric charge. Since the acceleration acting on particles is determined by the ratio of mass to charge of particles, the trajectory of a macroparticle is same with the one of real particle when other conditions are same because macro particles conserve the ratio of mass to charge of real particles in a species.

When the effect of current density is negligible because of, usually, low relative velocity of moving charges, the equation (2.6) vanishes and the Maxwell's equations can be replaced by the Poisson's equation. In order to couple equations for field and the Newton-Lorentz, the charge of macroparticles should be assigned to field. This is called charge assigning to mesh. On the other hand, force by field computation on mesh is interpolated to macroparticles, which is not usually on the mesh where the field value computed numerically. This method, called charge interpolation, and charge assigning to mesh is described in the following section.

2.1 Charge Assign and Field Interpolation

When charge of particle is assigned on mesh, one of three charge assigning functions, shown schematically in Fig. 2.1, are usually used. Three functions are called Nearest Grid Point (NGP), Cloud-in-Cell (CIC), and Triangular Shape Cloud (TSC) in the order of Fig. 2.1. They are zeroth order, first order, and second order shape function respectively [3, 4]. The NGP, CIC, and TSC are defined in 1D as follows:

$$NGP \quad S_0(x) = \begin{cases} 1, & \text{for } \dfrac{|x|}{\Delta x} \le \dfrac{1}{2} \\ 0, & \text{otherwise} \end{cases} \tag{2.7}$$

$$CIC \quad S_1(x) = \begin{cases} 1 - \dfrac{|x|}{\Delta x}, & \text{for } \dfrac{|x|}{\Delta x} \le 1 \\ 0, & \text{otherwise} \end{cases} \tag{2.8}$$

$$TSC \quad S_2(x) = \begin{cases} \dfrac{3}{4} - \left(\dfrac{|x|}{\Delta x}\right)^2, & \text{for } \dfrac{|x|}{\Delta x} \le \dfrac{1}{2} \\ \dfrac{1}{2}\left(\dfrac{3}{2} - \dfrac{|x|}{\Delta x}\right)^2, & \text{for } \dfrac{1}{2} \le \dfrac{|x|}{\Delta x} \le \dfrac{3}{2} \\ 0, & \text{otherwise} \end{cases} \tag{2.9}$$

The shape functions in higher dimensions can be easily obtained by multiplying single-coordinate shape functions. For example, a three dimensional CIC can be obtained as $S_2(\mathbf{x}) = S_2(x_1)S_2(x_2)S_2(x_3)$, where x_1, x_2, and x_3 are spatial coordinates.

When the same function is used for field interpolation, the total momentum is identically conserved in the absence of roundoff errors [3, 4].

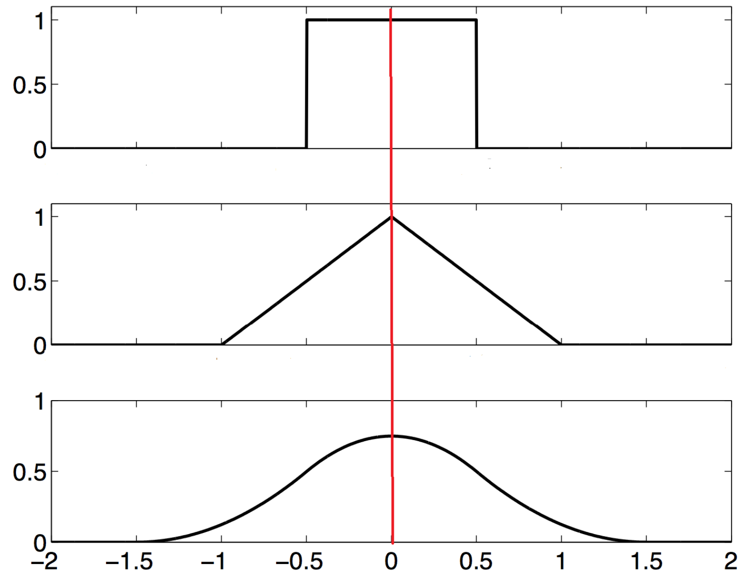

Figure 2.1: Charge assigning functions of order zeroth, first, and second, respectively. The horizontal coordinate is x_i / Δx_i where x_i and Δx_i denote i-th spatial coordinate and grid size of x_i coordinate.

Even though macroparticle is represented by point charge, in reality it has a shape or distribution of charge defined by the charge assigning function. Therefore, the charge assigning function is strongly related with current density implementation in a code. In order to balance the complexity and accuracy of advanced plasma chemistry algorithms, the code SPACE (Chapter 4) mainly uses the CIC, a bilinear (trilinear in 3D case) method. Hence the CIC is described more in detail. Figure 2.2 shows its concepts.

The CIC method assumes uniform charge density cloud having same volume with one mesh grid. In figure 2.2, straight lines mean mesh grid cells and broken lines mean the dual grids of the mesh grids. The particle points on mesh grid represent charge in the area (volume in 3D case) enclosed by the broken lines. The charge of each particle is weighted over the four (eight in 3D case) closest grid points made by the straight lines. The weighting is proportional to the intersecting area (volume in 3D case) with the dual cell including the grid point.

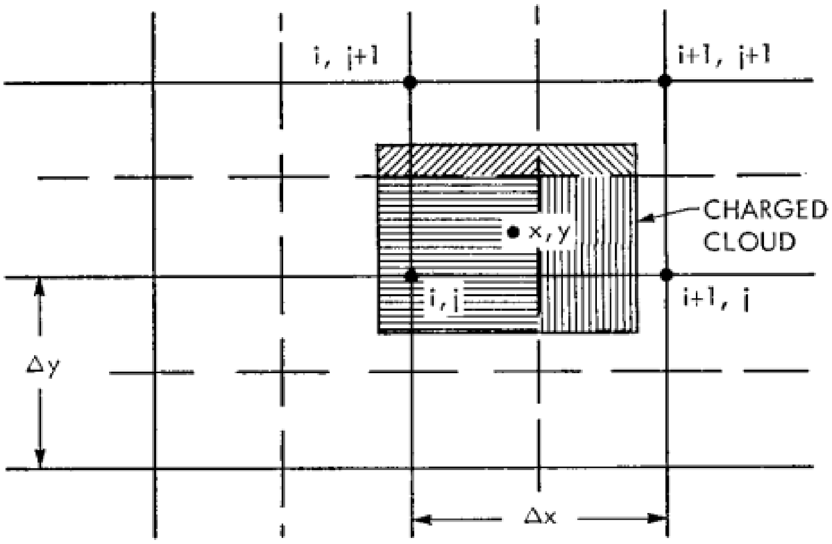

Figure 2.2: Cloud-in-Cell method [5]

In actual computation, we do not need to consider the dual grid. Instead, we can use the computation method explained by figure 2.3 formulae (2.10). We calculate weight of vertices by area (volume in 3D case) of opposite side.

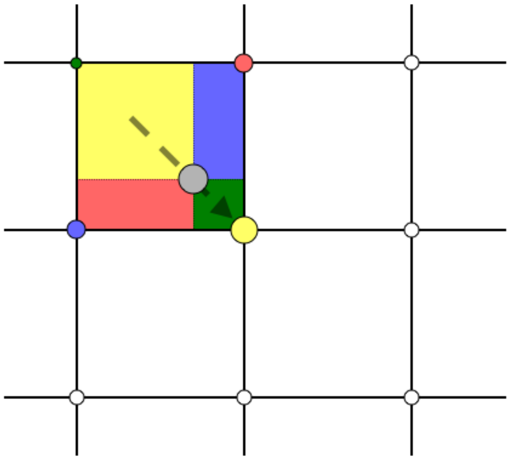

Figure 2.3: Distributing particle charge to mesh grid [6]

Then weight factors are given as following

$$\begin{cases} w_1 = (1-h_x)(1-h_y) \\ w_2 = h_x(1-h_y) \\ w_3 = (1-h_x)h_y \\ w_4 = h_xh_y \end{cases} \tag{2.10}$$

where w_1, w_2, w_3 and w_4 correspond to the blue, yellow, green and pink nodes, respectively and h_x is the fractional distance of the particle from the cell origin in the x direction.

2.2 PIC Method for Electrostatic Problems

Electrostatic problems usually deal with effects of electric charges at rest or moving at a low speed.

The governing equation of this problem is the Gauss law, $\nabla \cdot \mathbf{D} = \rho$.

Since the electric field intensity $\mathbf{E}$ can be described by a potential function ϕ, using the equation $\mathbf{E} = -\nabla\phi$ and the material equation $\mathbf{D} = \epsilon\mathbf{E}$, we obtain $\nabla^2\phi = -\frac{\rho}{\epsilon}$. By solving this Poisson's equation, we first can get the potential function ϕ. So we come to get electric field intensity from the potential ϕ. On the other hand, the force acting on particles is $\mathbf{F} = q\mathbf{E}$. Figure 2.4 shows processing flow in a time step of electrostatic problems.

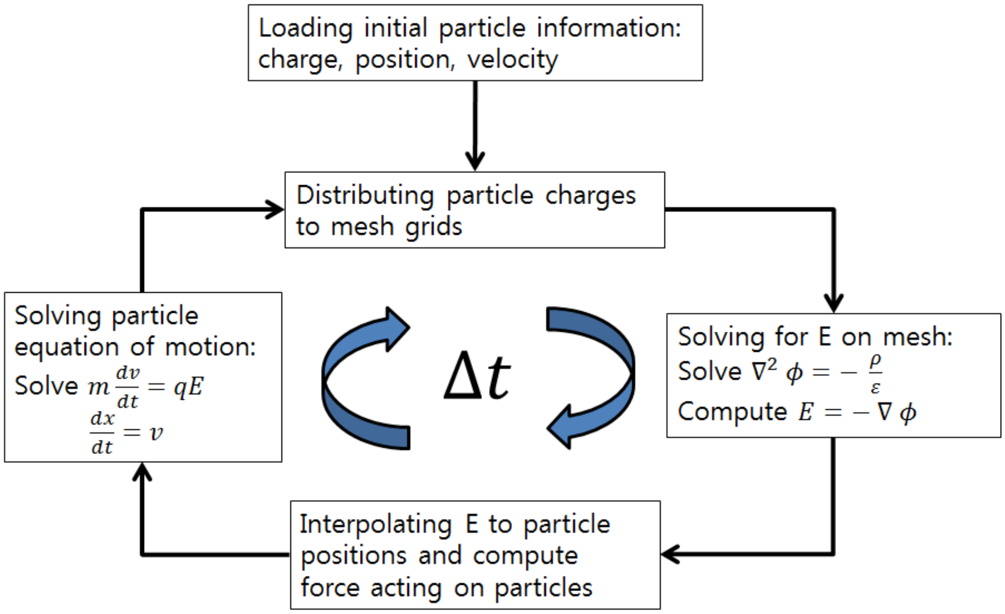

Figure 2.4: Processing flow in a time step of electrostatic problems

2.2.1 Adaptive Particle-in-Cloud Method

The PIC method for electrostatic problem is not optimal in terms of balance of errors of the differential operator discretization and source integral. Also, it is not accurate when the particle distribution is highly non-uniform.

The new method Adaptive Particle-in-Cloud (AP-Cloud) [7] replaces the

Cartesian grid of the PIC with adaptive computational particles (nodes). The charge of macroparticles of the PIC are assigned to the computational particles by a weighted least-square approximation. The partial differential equation, such as the Poisson's equation in the electrostatic problem, is discretized using the generalized finite difference (GFD) method and solved using a scalable linear solver. Since the density of computational particles is chosen adaptively, the error from GFD and the source integration is balanced and eventually the total error is approximately minimized. The method is also free of artifacts typical for some other adaptive methods such as AMR-PIC [8, 9].

Figure 2.5 and 2.6 show the benchmark simulation results in 2D halo problem. The graphs show that the solution of the Poisson's equation and its gradient by AP-Cloud are much more accurate than the PIC computation.

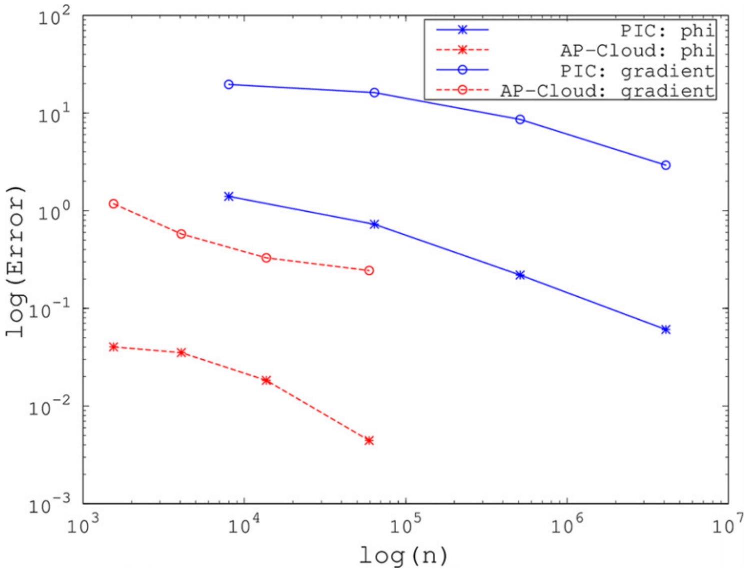

Figure 2.5: Dependence of errors on number of nodes for PIC and AP-Cloud in 2D Gaussian halo problem [7].

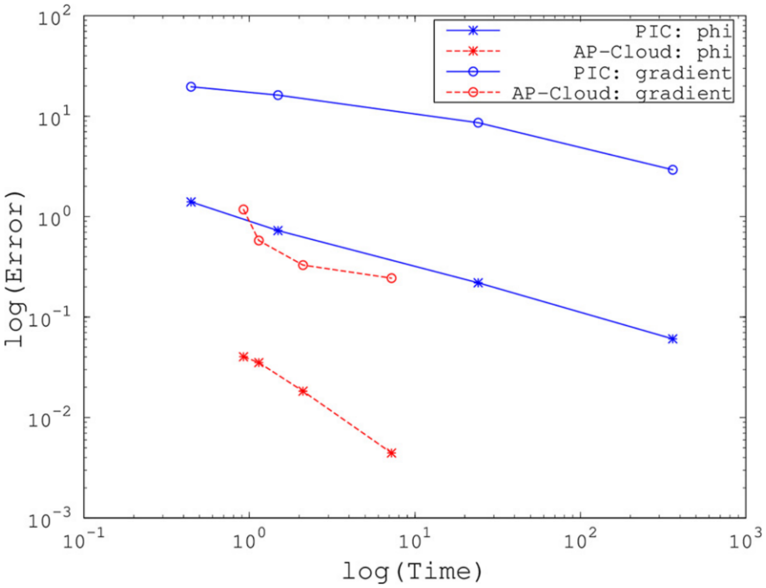

Figure 2.6: Dependence of errors on time for PIC and AP-Cloud in 2D Gaussian halo problem [7].

My contribution to the method is the design and implementation of a parallel octree data structure and the search algorithms for physical and computational particles.

2.3 PIC Method for Electromagnetic Problems

Contrary to electrostatic problems, electromagnetic problems require solving the full Maxwell's equations. The Maxwell's equations and its significance are listed in Table 2.1.

In the Maxwell's equations, the third and the forth equations hold if they are satisfied at the initial time together with the charge conservation law $\rho_t + \nabla \cdot \mathbf{J} = 0$. Therefore, solving the first and the second equations, the Faraday's law and the Ampère's circuital law respectively, in the Maxwell's

Table 2.1: The Maxwell's equations.

Differential Form	Integral Form	Significance
$\frac{\partial \mathbf{B}}{\partial t} = -\nabla \times \mathbf{E}$	$\oint_C \mathbf{E} \cdot dl = -\frac{d\Phi}{dt}$	Faraday's law
$\frac{\partial \mathbf{D}}{\partial t} = \nabla \times \mathbf{H} - \mathbf{J}$	$\oint_C \mathbf{H} \cdot dl = I + \int_S \frac{\partial \mathbf{D}}{\partial t} \cdot d\mathbf{s}$	Ampère's circuital law
$\nabla \cdot \mathbf{D} = \rho$	$\oint_C \mathbf{D} \cdot d\mathbf{s} = Q$	Gauss's law
$\nabla \cdot \mathbf{B} = 0$	$\oint_C \mathbf{B} \cdot d\mathbf{s} = 0$	No isolated magnetic charge

equations is sufficient if the charge conservation law is satisfied. In order to solve the first and the second equations in the Maxwell's equations, the Finite Difference Time Domain (FDTD) method [10] is proposed with restriction that the Ampère's circuital law doesn't have current density (or current). The current term which is not described in the FDTD is contributed by moving charge and the moving charge is computed by the Newton-Lorentz equation. The induced current by moving charge is combined in the second equation (Ampère's circuital law). In order to keep the charge conservation law in the numerical computation, the rigorous charge conservation method [11] is applied.

2.3.1 Finite Difference Time Domain Method and Yee Mesh

The Finite Difference Time Domain (FDTD) method approximates the Maxwell's equations without charge and source in the computational domain. Then the Ampère's circuital law becomes $\frac{\partial \mathbf{D}}{\partial t} = \nabla \times \mathbf{H}$ and the Gauss's law becomes $\nabla \cdot \mathbf{D} = 0$. In this modification, we first describe discretization of the Faraday's law and the Ampère's circuital law.

The FDTD method uses a staggered Cartesian grid called Yee cell [10]. Figure 2.7 shows an Yee cell and Figure 2.8 shows indexes of an Yee cell .

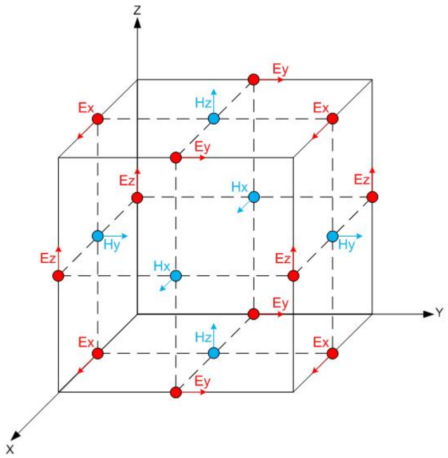

Figure 2.7: Yee Cell: Locations of the components in three dimensions

The FDTD method uses the second order central difference scheme in space and the second order Leapfrog scheme in time. Also it uses a staggered scheme in both space and time. Figure 2.9 shows the one dimensional space-time chart of the FDTD.

On this staggered grid, we have following discretization of the Ampère's

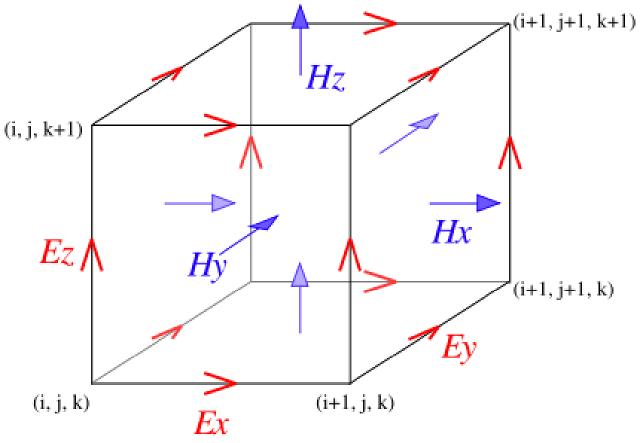

Figure 2.8: Yee Cell: Locations of grid indexes in three dimensions

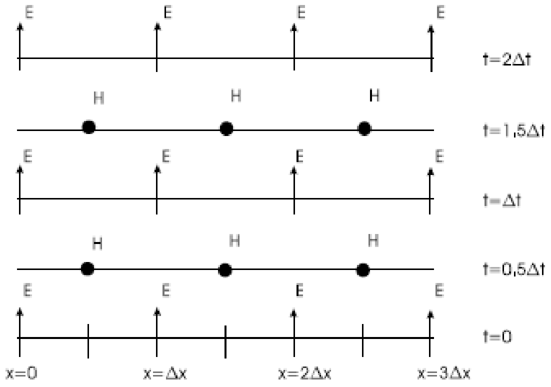

Figure 2.9: The one dimensional space-time chart of FDTD

circuital law

$$\begin{cases} (E_x)^{t+\Delta t}_{(i+1/2,j,k)} = (E_x)^{t}_{(i+1/2,j,k)} + \\ \frac{\Delta t}{\epsilon}\left(\left(\frac{(H_z)^{t+\Delta t/2}_{(i+\frac{1}{2},j+\frac{1}{2},k)} - (H_z)^{t+\Delta t/2}_{(i+\frac{1}{2},j-\frac{1}{2},k)}}{\Delta y}\right) - \left(\frac{(H_y)^{t+\Delta t/2}_{(i+\frac{1}{2},j,k+\frac{1}{2})} - (H_y)^{t+\Delta t/2}_{(i+\frac{1}{2},j,k-\frac{1}{2})}}{\Delta z}\right)\right) \\ (E_y)^{t+\Delta t}_{(i,j+1/2,k)} = (E_y)^{t}_{(i,j+1/2,k)} + \\ \frac{\Delta t}{\epsilon}\left(\left(\frac{(H_x)^{t+\Delta t/2}_{(i,j+\frac{1}{2},k+\frac{1}{2})} - (H_x)^{t+\Delta t/2}_{(i,j-\frac{1}{2},k-\frac{1}{2})}}{\Delta z}\right) - \left(\frac{(H_z)^{t+\Delta t/2}_{(i+\frac{1}{2},j+\frac{1}{2},k)} - (H_z)^{t+\Delta t/2}_{(i-\frac{1}{2},j+\frac{1}{2},k)}}{\Delta x}\right)\right) \\ (E_z)^{t+\Delta t}_{(i,j,k+1/2)} = (E_z)^{t}_{(i,j,k+1/2)} + \\ \frac{\Delta t}{\epsilon}\left(\left(\frac{(H_y)^{t+\Delta t/2}_{(i+\frac{1}{2},j,k+\frac{1}{2})} - (H_y)^{t+\Delta t/2}_{(i-\frac{1}{2},j,k+\frac{1}{2})}}{\Delta x}\right) - \left(\frac{(H_x)^{t+\Delta t/2}_{(i,j+\frac{1}{2},k+\frac{1}{2})} - (H_x)^{t+\Delta t/2}_{(i,j-\frac{1}{2},k+\frac{1}{2})}}{\Delta y}\right)\right) \end{cases} \tag{2.11}$$

and discretization of the Faraday's law

$$\begin{cases} (H_x)^{t+3/2\Delta t}_{(i,j+1/2,k+1/2)} = (H_x)^{t+1/2\Delta t}_{(i,j+1/2,k+1/2)} + \\ \dfrac{\Delta t}{\mu}\left(\left(\dfrac{(E_y)^{t+\Delta t}_{(i,j+\frac{1}{2},k+1)} - (E_y)^{t+\Delta t}_{(i,j+\frac{1}{2},k)}}{\Delta z}\right) - \left(\dfrac{(E_z)^{t+\Delta t}_{(i,j+1,k+\frac{1}{2})} - (E_z)^{t+\Delta t}_{(i,j,k+\frac{1}{2})}}{\Delta y}\right)\right) \\ (H_y)^{t+3/2\Delta t}_{(i+1/2,j,k+1/2)} = (H_y)^{t+1/2\Delta t}_{(i+1/2,j,k+1/2)} + \\ \dfrac{\Delta t}{\mu}\left(\left(\dfrac{(E_z)^{t+\Delta t}_{(i+1,j,k+\frac{1}{2})} - (E_z)^{t+\Delta t}_{(i,j,k+\frac{1}{2})}}{\Delta x}\right) - \left(\dfrac{(E_x)^{t+\Delta t}_{(i+\frac{1}{2},j,k+1)} - (E_x)^{t+\Delta t}_{(i+\frac{1}{2},j,k)}}{\Delta z}\right)\right) \\ (H_z)^{t+3/2\Delta t}_{(i+1/2,j+1/2,k)} = (H_z)^{t+1/2\Delta t}_{(i+1/2,j+1/2,k)} + \\ \dfrac{\Delta t}{\mu}\left(\left(\dfrac{(E_x)^{t+\Delta t}_{(i+\frac{1}{2},j+1,k)} - (E_x)^{t+\Delta t}_{(i+\frac{1}{2},j,k)}}{\Delta y}\right) - \left(\dfrac{(E_y)^{t+\Delta t}_{(i+1,j+\frac{1}{2},k)} - (E_y)^{t+\Delta t}_{(i,j+\frac{1}{2},k)}}{\Delta x}\right)\right). \end{cases} \tag{2.12}$$

On the first iteration, we need to calculate $H^{\Delta t/2}$ values. In this case, we use the Euler method. Although it is unstable, it is used for only one time step. The two divergence formulas, $\nabla \cdot \mathbf{B}$ and $\nabla \cdot \mathbf{E}$, remain zero if they are so initially. This is also true when we use space and time centered scheme for the the approximations of two divergences. Therefore it is sufficient to solve only the Faraday's law and the Ampère's circuital law.

2.3.2 The Newton-Lorentz Equation

Charges in a domain move by the electric and magnetic forces which are computed by solving the Maxwell's equations and given by external forces.

The motion is described by the Newton-Lorentz equations as following:

$$m\frac{d\mathbf{v}_p}{dt} = \mathbf{F}_p = q_p\left(\mathbf{E}(\mathbf{x}_p) + \mathbf{v}_p \times \mathbf{B}(\mathbf{x}_p)\right). \tag{2.13}$$

In order to solve the Newton-Lorentz equation numerically, it is needed to be discretized and approximated. The leapfrog scheme for the Newton-Lorentz equation is described as following:

$$\begin{cases} \dfrac{\mathbf{x}^{n+1} - \mathbf{x}^{n}}{\Delta t} = \mathbf{v}^{n+1/2} \\ \dfrac{\mathbf{v}^{n+\frac{3}{2}} - \mathbf{v}^{n+\frac{1}{2}}}{\Delta t} = \dfrac{q}{m}\left(\mathbf{E}^{n+1}(\mathbf{x}^{n+1}) + \left(\dfrac{\mathbf{v}^{n+\frac{3}{2}} + \mathbf{v}^{n+\frac{1}{2}}}{2} \times \mathbf{B}^{n+1}(\mathbf{x}^{n+1})\right)\right) \end{cases} \tag{2.14}$$

where $\mathbf{B}^{n+1} = \frac{\mathbf{B}^{n+1/2}+\mathbf{B}^{n+3/2}}{2}$. The leapfrog scheme is widely used for the Newton-Lorentz equation because it is a symplectic scheme [12]. The positions of a charge precedes the velocity of the charge by the half time step as **E** (Electric Field Intensity) precedes **H** (Magnetic Field Intensity) by the half time step. The computation sequence of the leapfrog scheme for the Newton-Lorentz equation in conjunction with the FDTD is schematized in Fig. 2.10.

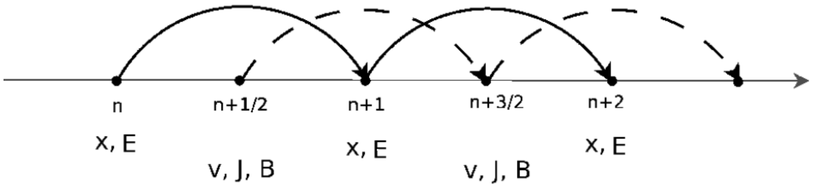

Figure 2.10: Computation sequence along time step

2.3.3 Explicit Conservative Time Integration

Even though the leapfrog scheme is symplectic, important for the conservation of energy during long time integration, the drawback of the scheme is that it is an implicit scheme.

The Boris scheme [13] makes an explicit scheme from

$$\frac{\mathbf{v}^{n+\frac{3}{2}} - \mathbf{v}^{n+\frac{1}{2}}}{\Delta t} = \frac{q}{m}\left(\mathbf{E}^{n+1}(\mathbf{x}^{n+1}) + \left(\frac{\mathbf{v}^{n+\frac{3}{2}} + \mathbf{v}^{n+\frac{1}{2}}}{2} \times \mathbf{B}^{n+1}(\mathbf{x}^{n+1})\right)\right). \tag{2.15}$$

Let

$$\begin{cases} u^{+} = u^{t+\Delta t/2} - \dfrac{q\mathbf{E}}{m}\dfrac{\Delta t}{2} \\ u^{-} = u^{t-\Delta t/2} + \dfrac{q\mathbf{E}}{m}\dfrac{\Delta t}{2}. \end{cases} \tag{2.16}$$

Then the equation (2.15) turns into

$$u^{+} - u^{-} = \frac{q\Delta t}{2m}\left(u^{+} + u^{-}\right) \times \mathbf{B}. \tag{2.17}$$

Here $\mathbf{E}$ means $\mathbf{E}_{n+1}(\mathbf{x}_{n+1})$ and $\mathbf{B}$ means $\mathbf{B}_{n+1}(\mathbf{x}_{n+1})$.

Then let

$$\mathbf{t} = \frac{q\Delta t}{2m}\mathbf{B}. \tag{2.18}$$

Then we can obtain

$$u^{+} - u^{-} = \left(u^{+} + u^{-}\right) \times \mathbf{t} \tag{2.19}$$

from (2.17).

By applying dot product $u^{+} + u^{-}$ on the both side of the equation (2.19), we obtain $|u^+|^2 = |u^-|^2$.

Next step is decomposing u^+ and u^- with parallel and orthogonal components with respect to $\mathbf{t}$. So let $u_\parallel = \alpha\mathbf{t}$ where $\alpha \geq 0$. That is, $u^+ = u_\perp^+ + u_\parallel^+$ where $u_\perp^+$ is the orthogonal component of $\mathbf{t}$ if the angle between u^+ and $\mathbf{t}$ is acute. If the angle is obtuse, then $u^+ = u_\perp^+ - u_\parallel^+$

From the equation (2.19), we have

$$\left(\left(u_\perp^+ + u_\parallel^+\right) - \left(u_\perp^- + u_\parallel^-\right)\right) = \left(\left(u_\perp^+ + u_\parallel^+\right) + \left(u_\perp^- + u_\parallel^-\right)\right) \times \mathbf{t} \tag{2.20}$$

by applying the above decomposition with the assumption that the angles are acute.

Then we obtain $|u_\perp^+|^2 = |u_\perp^-|^2$ by applying $(u_\perp^+ + u_\perp^-)$ on the both side of (2.20). So we can obtain $|u_\parallel^+| = |u_\parallel^-|$. So we have $u_\parallel^+ = \pm u_\parallel^-$. In fact, if both u^+ and u^- have acute or obtuse angles from $\mathbf{t}$, then we have $u_\parallel^+ = u_\parallel^-$. But if one is acute and another is obtuse, then we have $u_\parallel^+ = -u_\parallel^-$.

From the equation (2.19), we obtain

$$u_\perp^+ - u_\perp^- = \left(u_\perp^+ + u_\perp^-\right) \times \mathbf{t}. \tag{2.21}$$

By referring figure 2.11, let $u'_\perp = u_\perp^- + u_\perp^- \times \mathbf{t}$ and $x = \frac{|u_\perp^-|^2|\mathbf{t}|}{|u'_\perp|}$ where $|u'_\perp|^2 = (1 + |\mathbf{t}|^2)|u_\perp^-|^2$. Then we obtain the following relation

$$u_\perp^+ = u_\perp^- + 2x\frac{u'_\perp \times \mathbf{t}}{|u'_\perp \times \mathbf{t}|} = u_\perp^- + \frac{2}{1 + |\mathbf{t}|^2}\left(u'_\perp \times \mathbf{t}\right). \tag{2.22}$$

If we have acute angle assumption (although we have the same result

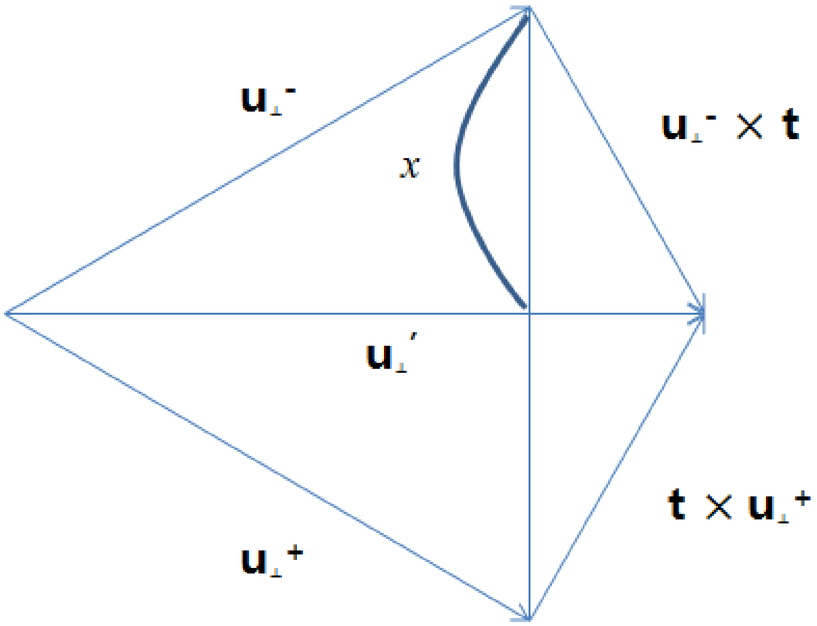

Figure 2.11: Geometric Relations

with the obtuse angle assumption), we obtain $u_\perp^+ = u_\perp^- + \frac{2}{1+|\mathbf{t}|^2}\left(u'_\perp \times \mathbf{t}\right) \Rightarrow$ $u^+ - u_\parallel^+ = u^- - u_\parallel^- + \frac{2}{1+|\mathbf{t}|^2}\left(\left(\left(u^- - u_\parallel^-\right) + \left(u^- - u_\parallel^-\right) \times \mathbf{t}\right) \times \mathbf{t}\right)$ since $u'_\perp = u_\perp^- + u_\perp^- \times \mathbf{t}$. Then we have

$$u^+ = u^- + \frac{2}{1+|\mathbf{t}|^2}\left(u' \times \mathbf{t}\right) \tag{2.23}$$

where $u' = u^- + u^- \times \mathbf{t}$.

In conclusion, we obtain

$$\begin{aligned} u^{t+\Delta t/2} &= u^{t-\Delta t/2} + \frac{q\Delta t}{m}\mathbf{E} \\ &+ \frac{2}{1+|\frac{q\Delta t}{2m}|^2|\mathbf{B}|^2}\left(\left(u^{t-\Delta t/2} + \frac{q\Delta t}{2m}\mathbf{E}\right) + \left(u^{t-\Delta t/2} + \frac{q\Delta t}{2m}\mathbf{E}\right) \times \left(\frac{q\Delta t}{2m}\mathbf{B}\right)\right) \\ &\times \left(\frac{q\Delta t}{2m}\mathbf{B}\right). \end{aligned} \tag{2.24}$$

In order to deal with moving charge of almost light speed (relativistic charge), the Lorentz factor γ should be considered. Since the Lorentz factor $\gamma = \frac{1}{\sqrt{1-\mathbf{v}^2/c^2}}$ is also a function of the charge velocity, it is not possible applying the Boris scheme. A new relativistic, explicit, and symplectic scheme is invented [14].

2.3.4 Rigorous Charge Conservative Method

When we solve the Maxwell's equation analytically, the forth equation always holds if it hold initially because we have $\nabla \cdot \mathbf{B}_t = -\nabla \cdot (\nabla \times \mathbf{E}) \Rightarrow (\nabla \cdot \mathbf{B})_t = 0$ by applying divergence to the Faraday's equation if $\mathbf{B}$ and $\mathbf{E}$ are sufficiently smooth.

On the other hand, if we assume charge density conservation, that is, $\rho_t = -\nabla \cdot \mathbf{J}$ holds in any open set in the given domain, the Ampère's circuital law equation implies the Gauss's law equation because we have $(\nabla \cdot \mathcal{D})_t = \nabla \cdot \mathcal{D}_t = \nabla \cdot (\nabla \times \mathbf{H}) - \nabla \cdot \mathbf{J} = -\nabla \cdot \mathbf{J} = \rho_t$ by applying divergence to the Ampère's circuital law if $\mathbf{B}$ and $\mathbf{E}$ are sufficiently smooth.

Therefore, if we assume charge density conservation and have $\nabla \cdot \mathcal{D} = \rho$

and $\nabla \cdot \mathbf{B} = 0$ as the initial condition, solving the first and the second equation in Maxwell's equations is sufficient in solving the full Maxwell's equations.

In section 2.3.1, we introduced the FDTD method solving the Ampère's circuital law and the Faraday's law. Although the numerical scheme solving the two equations automatically preserves consistency with $\nabla \cdot \mathbf{B} = 0$ equation, we still need to solve the Gauss's law equation. As introduced in section 2.2, we have to solve the Poisson's equation to solve the Gauss's equation in each time step if the numerical scheme does not conserve charge density.

However, the method [11] by Villasenor and Buneman offers the way preserves charge density approximated by the Cloud-in-Cell (CIC) method. Hence, as mentioned earlier, since we use the CIC approximation of charge, we can take advantage of the method. Therefore we do not need to solve the Poisson's equation except at the initial time.

Figure 2.12, 2.13, and 2.14 explain current density calculation on the each side of the dual grid. The coordinates x and y are the location of the "local origin". Actually, the local origin is the cell center of our grid cell. Δx and Δy are moving distance along x-coordinate and y-coordinate respectively. Figure 2.12 shows the simplest case in 2D when a particle moves in a grid cell. Figure 2.13 and 2.14 show that a particle moves in two cells and three cells respectively. Since the cases of particles moving over two and three cells are serial connections of the simplest case, we will explain the simplest case.

By assuming unit charge, unit grid size, and unit time, current density J_{y1} is the total charge passing the side J_{y1} representing. So it is $\int_0^{\Delta y} \frac{\Delta x}{\Delta y} t + (0.5 - x)\, dt = \Delta y \left(\frac{1}{2} - x - \frac{1}{2} \Delta x \right)$. In fact, this value is the area generated by

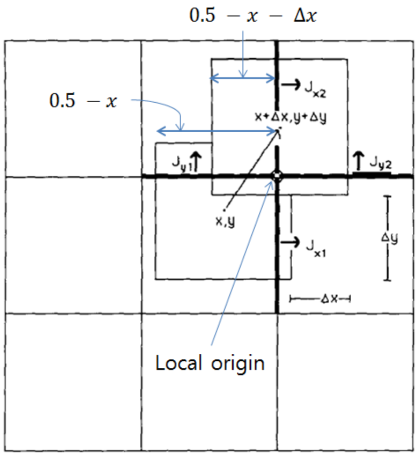

Figure 2.12: Current computation in one cell [11]

moving particle trace of the second quadrant. This method does not use any approximation. This method uses exact calculation by using approximated charges. Therefore, this method satisfies with our finite difference discretization of the charge conservation equation $\frac{\partial \rho}{\partial t} = -\nabla \mathbf{J}$. So this method guarantees that $\nabla \cdot \mathcal{D} = \rho$ is valid at every time step by the initial condition.

We obtain the following current density values in Figure 2.12.

$$\begin{cases} J_{x1} = \Delta x \left(\frac{1}{2} - y - \frac{1}{2} \Delta y \right) \\ J_{x2} = \Delta x \left(\frac{1}{2} + y + \frac{1}{2} \Delta y \right) \\ J_{y1} = \Delta y \left(\frac{1}{2} - x - \frac{1}{2} \Delta x \right) \\ J_{y2} = \Delta y \left(\frac{1}{2} + x + \frac{1}{2} \Delta x \right) \end{cases} \tag{2.25}$$

This method can be extended to 3D. The algorithm is summarized as following in the simplest case which a particle moves in a grid cell from $(i +$

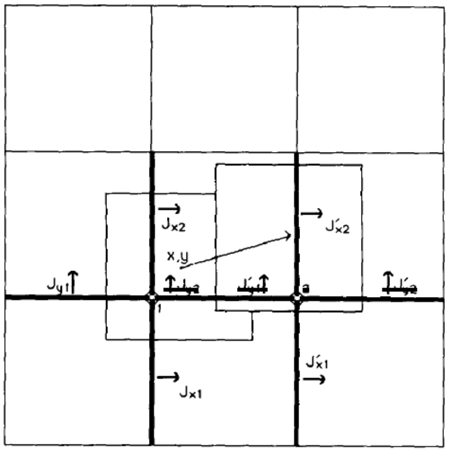

Figure 2.13: Current computation in two cells [11]

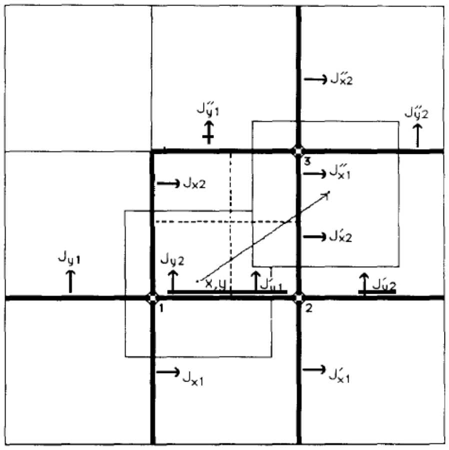

Figure 2.14: Current computation in three cells [11]

$\xi_1, j + \eta_1, k + \zeta_1)$ to $(i + \xi_2, j + \eta_2, k + \zeta_2)$.

$$\begin{cases} (J_x)_{(i+\frac{1}{2},j,k)} = \Delta x \left(1 - \overline{\eta}\right)\left(1 - \overline{\zeta}\right) + \Delta x \Delta y \Delta z / 12 \\ (J_x)_{(i+\frac{1}{2},j+1,k)} = \Delta x \overline{\eta}\left(1 - \overline{\zeta}\right) - \Delta x \Delta y \Delta z / 12 \\ (J_x)_{(i+\frac{1}{2},j,k+1)} = \Delta x \left(1 - \overline{\eta}\right)\overline{\zeta} - \Delta x \Delta y \Delta z / 12 \\ (J_x)_{(i+\frac{1}{2},j+1,k+1)} = \Delta x \overline{\eta}\overline{\zeta} + \Delta x \Delta y \Delta z / 12 \end{cases} \tag{2.26}$$

where ξ_n, η_n, ζ_n lie between 0 and 1, $\overline{\xi} = (\xi_1 + \xi_2)/2$, $\overline{\eta} = (\eta_1 + \eta_2)/2$, $\overline{\zeta} = (\zeta_1 + \zeta_2)/2$. The four contributions to $\mathbf{J}_y$ and $\mathbf{J}_z$ are obtained from equation (2.26) by the cyclic rotation $i, \Delta x, \overline{\xi} \Rightarrow j, \Delta y, \overline{\eta} \Rightarrow k, \Delta z, \overline{\zeta} \Rightarrow i, \Delta x, \overline{\xi}$. For higher charge assigning function, the Esirkepov algorithm has been invented [15].

2.3.5 Summary

The Maxwell's equations are solved by the FDTD scheme on the Yee mesh. The electric and magnetic fields, which may include external fields, push charge by the Newton-Lorentz equation and the equations is numerically solved by the Boris scheme (or the relativistic explicit leapfrog scheme). The motion of charge induces current. The induced current is computed by the rigorous charge conservation scheme and the current factor is updated on the Ampère's circuital law. Since the rigorous charge conservation is used, the charge conservation law holds exactly, which means that the computation does not have roundoff or approximation error. By the charge conservation law, the Maxwell's equation is solved by the first and the second equations without solving the Poisson's equation (the Gauss's law). The processing flow in a time step is schematized in Fig. 2.15.

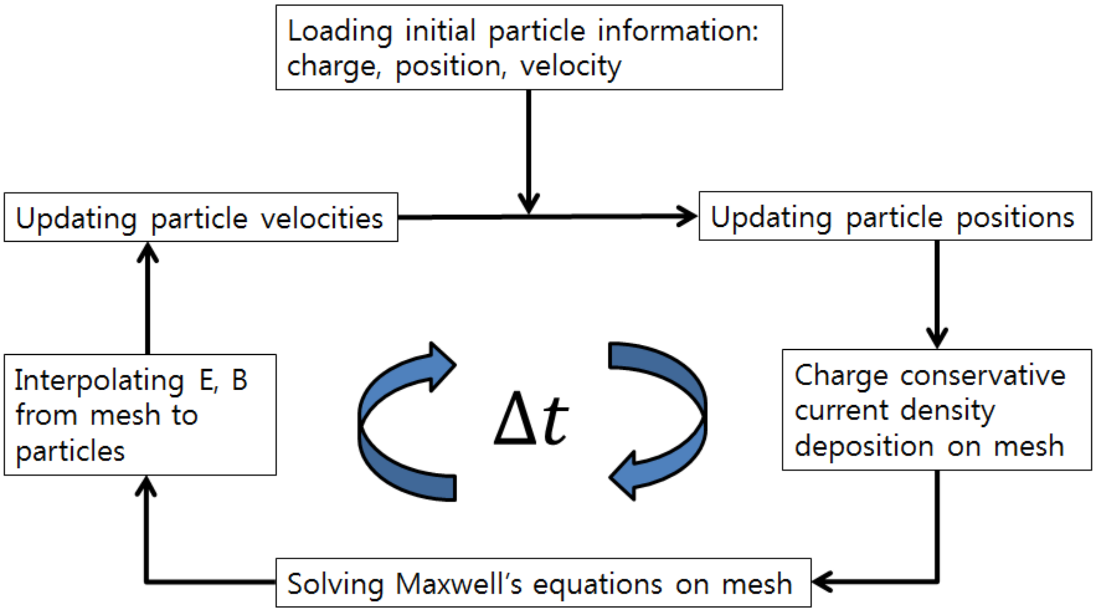

Figure 2.15: Processing flow in a time step of electromagnetic problems

Chapter 3

New Algorithms for Relativistic Electromagnetism and Atomic Physics

3.1 Base Algorithm: Stationary Ions

In simulations of neutral plasmas, positive charges (usually ions) and negative charges (usually electrons) are balanced, giving the total zero charge. When heavy ions are almost stationary and the total charge of the plasma is zero, the total number of plasma particles can be reduced by half by using only electron particles. This method is described in this section.

$$\frac{\partial \mathbf{B}}{\partial t} = -\nabla \times \mathbf{E} \tag{3.1a}$$

$$\frac{\partial \mathbf{E}}{\partial t} = \frac{1}{\epsilon_0 \mu_0} \nabla \times \mathbf{B} - \frac{1}{\epsilon_0} \mathbf{J} \tag{3.1b}$$

$$\nabla \cdot \mathbf{E} = \frac{\rho}{\epsilon_0} \tag{3.1c}$$

$$\nabla \cdot \mathbf{B} = 0. \tag{3.1d}$$

When one solves the Maxwell's equations analytically, solving Equation (3.1a) and Equation (3.1b) is sufficient: if Equation (3.1c) and Equation (3.1d) are satisfied at initial time, they remain invariants of motion at later time by the charge conservation law:

$$\frac{\partial \rho}{\partial t} + \nabla \mathbf{J} = 0. \tag{3.2}$$

This property is conserved by the rigorous charge conservation method [11]. That is, Equation 3.1c is solved once at the initial time and the equation holds during rest computation.

For plasma particle of total zero charge, only electron particles are generated and the plasma charges are not initialized. Thus, even though electron particles are generated, the total charge is still zero because the charges are not initialized. For one electron, Fig. 3.1a shows the initial stage of an electron particle. After the displacement of the particle, the rigorous charge conservation method carries the charge exactly to the new position. In other words, the negative charge is carried from the initial position to the new position as show Fig. 3.1b. Therefore, the positive charge is remained at the initial position.

The stationary ion method is validated by the plasma lens simulation. A muon beam of $\beta = 0.88$ is injected into 5 cm cavity. In the plasma filled cavity, only electrons are preformed (without ions) and the charge of electrons are not initialized. Thus the total charge and local charge in the cavity is zero. As the muon beam pass through the cavity, the space charge of the beam push away light electrons except heavy ions. Before the entrance of the beam, the

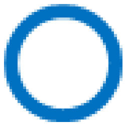

(a) Initial charge position with zero charge

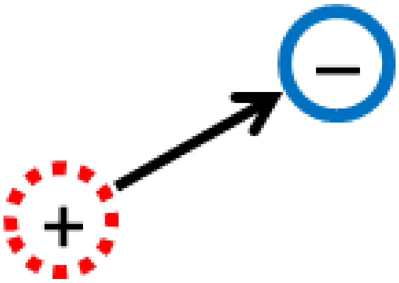

(b) Charge displacement

Figure 3.1: Schematic diagram of the stationary ion algorithm.

space charge of the beam and the induced magnetic field by moving charge of the beam are balanced. After the injection, since the beam push away only electrons and ions are remained in the center of the beam along its trace, the space charge of the beam is compensated and the induced magnetic field focus the beam. This effect is compared with the beam passing in vacuum cavity. In Fig. 3.2a and 3.2b, beam focusing does not happen. On the other hand, the focusing effect is observed in Fig. 3.2c and 3.2d

(a) 250 ps in vacuum (b) 300 ps in vacuum

(c) 250 ps in plasma (d) 300 ps in plasma

Figure 3.2: Plasma lens effect test for the stationary ion method validation. 3 cm length and 2 mm radius Gaussian muon beam of $\beta = 0.88$ is injected into 5cm length cavity. Two cases of cavity with vacuum and plasma filled are compared.

3.2 Algorithms for Beam Plasma Interaction

3.2.1 Generation of Plasma Macroparticles

Two algorithms for the dynamic generation of plasma have been developed. Here we describe the first algorithm that dynamically creates plasma macroparticle pairs. The second algorithm that changes the representing number, which is the real particle number one macroparticle stands for, of macroparticles is described in the next subsection. Consider an example of neutral gas ionization by a high energy particle beam. As each beam macroparticle passes through the gas, it loses energy and ionizes the medium in real time by creating electron - ion pairs. The process is described by the Bethe-Bloch equation [16]. At the same time, the energy lose is reflected to the beam particle by reducing its kinetic energy as shown in Fig. 3.3. Each pair of electron and ion macroparticles must be created in the same spatial location to satisfy the initial local neutrality. The mobility of ions is often very low throughout the simulation and the motion of ions can be ignored. In this case, we need to create only electron macroparticles.

3.2.2 Variable Representing Number of Macroparticle

Plasma density can change by orders of magnitude via ionization and recombination processes. When a fixed representing number is used for plasma, the plasma density variation involves changing the number of macroparticles of plasma. It may cause poor accuracy in the low density regions represented by small number of macroparticles or waste of computing resources in high

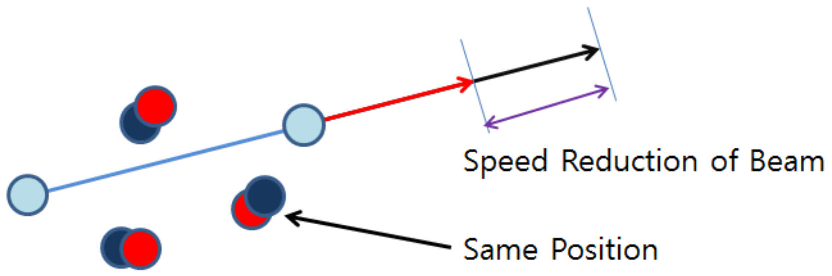

Figure 3.3: Schematic diagram of the ionization algorithm.

density regions containing large number of macroparticles. This problem is effectively eliminated by using variable representing number of macroparticles. In this algorithm, a preset cloud of massless neutral plasma macroparticles (with zero representing number) is initialized, and such macroparticles are charged during ionization processes. The representing number of a plasma macroparticle increases when ionization occurs and it decreases when recombination occurs. This algorithm also eliminates the effect of artificial charge separation if spatially displaced ion and electron macroparticles are removed in the recombination process within the method described above.

3.2.3 Ionization and Recombination

In the variable representing number algorithm, the total number of macroparticles remains constant while particle representing numbers increase or decrease according to ionization and recombination processes. Figure 3.4 shows the schematic description of the stopping power computation by a particle beam. By the movement of a beam particle (blue), its energy loss in gas is

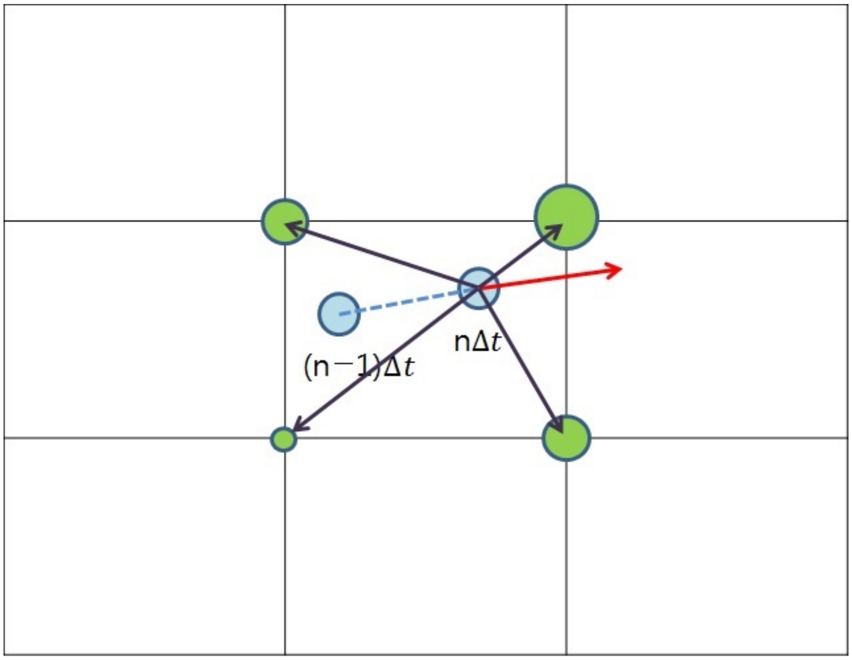

Figure 3.4: Schematic diagram of the stopping power computation algorithm.

estimated and distributed to the FDTD mesh (green). At the same time, the energy loss of the beam particle is counted and used to update the velocity of the beam particle. After that, the number of new plasma pairs is computed on the mesh. The number of new ionization events in each mesh block is distributed to the plasma macroparticles and used for to change of their representing number. The recombination has the reverse process.

3.3 Visualization Algorithms for Lorentz Boosted Frame Simulation

To study super relativistic beam, simulation in a moving frame has numerous advantages compared to simulations in a laboratory frame. The computational efficiency was estimated analytically [17]. Even though a simulation is performed in a Lorentz boosted frame, visualization or data representation in the laboratory frame is necessary to compare simulation results with experimental data since experimental measurements are represented in a laboratory frame. But the visualization in the laboratory frame after doing simulation in a Lorentz boosted frame is difficult due to the Lorentz transformation property: particles collected at a fixed time in the moving frame obtain different times after being transformed to the laboratory frame. Therefore, the beam particles after the Lorentz transformation are distributed in different time.

Let $\mathcal{L}^*$, $\mathcal{L}$ be a laboratory frame and a moving frame, respectively. The superscript $*$ denotes a laboratory frame. For example, z^* denotes z-coordinates in a laboratory frame and z denotes z-coordinates in a moving frame. Then the Lorentz transformation describes the relation between a moving frame and a laboratory frame. Let the moving frame be moving to z-coordinate direction with speed v with respect to the laboratory frame. Then we have following relations from the moving frame to the laboratory frame:

$$x^* = x \tag{3.3a}$$

$$y^* = y \tag{3.3b}$$

$$z^* = \gamma(z + \beta ct) \tag{3.3c}$$

$$ct^* = \gamma(\beta z + ct) \tag{3.3d}$$

where c is the light speed in vacuum and $\gamma(= 1/\sqrt{1 - v^2/c^2})$ is the relativistic factor.

By the Lorentz transformation, objects at the same time in the moving frame are transformed into the laboratory frame with different times. Thus particles after the Lorentz transformation have different time in the laboratory frame. In order to for all particles have same time after the Lorentz transformation, all particles should have same value

$$\frac{\beta}{c}z + t \tag{3.4}$$

in the moving frame, even though particles have different z-coordinates in the moving frame. This means that particles have different z-coordinates should be transformed from different time with the relation in formula (3.4) in the moving frame in order to have same time after the Lorentz transformation. For simulations, since time is discretized, let $t = n\Delta t$ where Δt is the time step size and $n \in \mathbb{Z}_+$. Even though, macroparticles should not be discretized in space, that is, the z coordinates of macroparticles can be any place in the domain without discretization, the space coordinate should be discretized properly to make formula (3.4) constant because time is discretized.

Although, the space discretization is required for the Lorentz transformation, particles can be placed at any location in the computational domain in PIC. For the space discretization of particles, the charge interpolation methods in PIC can be used. This discretization do not need to be consistent with the space discretization of the finite difference time domain (FDTD) solver in EM-PIC. In Figure 3.5, there are many macroparticles in the beam region.

The macroparticles can be placed at any position regardless of the background grids. But, by the charge assigning from particles to grids, particles can be placed on the grids. So we assume that all macroparticles are placed on the grids. In other words, we assume that particles are discretized well in the computational domain. Only one dimensional discretization is necessary in a 3D simulation if the moving frame is moving to a coordinate direction (z-axis direction in our case).

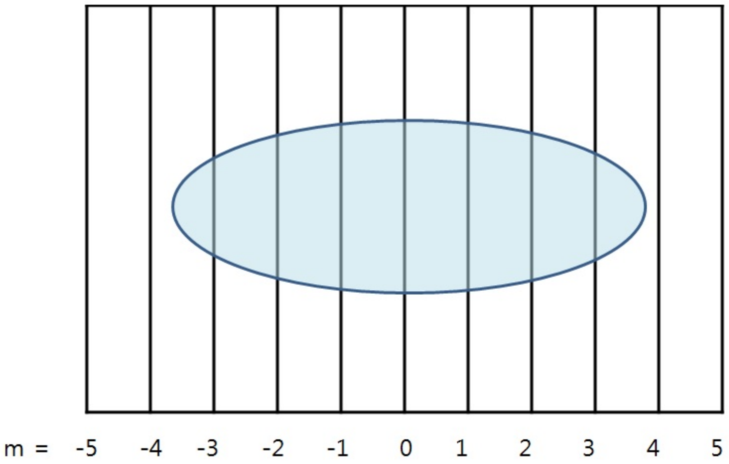

Figure 3.5: Schematic diagram of spatial discretization of a beam in a moving frame. There are many macroparticles in the blue and elliptic region. The macroparticles are not described in the beam region.

Let $z = m\Delta z$ where $m \in \mathbb{Z}$. To find relation of z and t satisfying formula (3.4) is constant, two method can be possible. The first method is using same time discretization with the computational time discretization and using new space discretization which is different from FDTD domain discretization to make formula (3.4) constant. The second method is using same domain discretization with the computational domain discretization and using new time discretization to make formula (3.4) constant. The former is described in section 3.3.1 and the latter is described in section 3.3.2.

3.3.1 Space Discretization Method

This method fixes time step size and find z satisfying the condition $\beta z+ct$ is constant. So Let

$$\frac{\beta}{c}z + t = n\Delta t \tag{3.5}$$

where $n \in \mathbb{Z}$ and fixed. In this method, since the time step sized is fixed, t in equation (3.5) can be described by $x\Delta t$. Also, since the domain is discretized, let $z = m\Delta z$. When we have $m = 0$, the z coordinate is called the "reference" position. Then the equation (3.5) becomes

$$\frac{\beta}{c}m\Delta z + x\Delta t = n\Delta t \Rightarrow \frac{\beta}{c}m\Delta z = (n-x)\Delta t \Rightarrow x = n - \frac{\beta}{c}\frac{\Delta z}{\Delta t}m. \tag{3.6}$$

Since m is the index of the space discretization and n and x are the indexes of the time discretization, x, n, and m are integers and m can be 1. So $(\beta\Delta z)/(c\Delta t)$ must be integer in order to make x integer.

Let α be $(\beta\Delta z)/(c\Delta t)$. The space discretization Δz in α do not need to be the same with the the discretization of $FDTD$. So Δz is not restricted by the CFL condition. But Δz could be the same one with the domain spacing of $FDTD$. In this case,

$$\Delta t \leq \frac{\Delta z}{c\sqrt{3}} \Rightarrow \frac{\beta}{c}\frac{\Delta z}{\Delta t} \geq \sqrt{3}\beta \tag{3.7}$$

$n=0$	m	x	$n=100$	m	x	z^*	$n=200$	m	x	z^*
	-5	50		-5	150	$\gamma 8.5\Delta z$		-5	250	$\gamma 17.5\Delta z$
	-4	40		-4	140	$\gamma 8.6\Delta z$		-4	240	$\gamma 17.6\Delta z$
	-3	30		-3	130	$\gamma 8.7\Delta z$		-3	230	$\gamma 17.7\Delta z$
	-2	20		-2	120	$\gamma 8.8\Delta z$		-2	220	$\gamma 17.8\Delta z$
	-1	10		-1	110	$\gamma 8.9\Delta z$		-1	210	$\gamma 17.9\Delta z$
	0	0		0	100	$\gamma 9.0\Delta z$		0	200	$\gamma 18.0\Delta z$
	1	-10		1	90	$\gamma 9.1\Delta z$		1	190	$\gamma 18.1\Delta z$
	2	-20		2	80	$\gamma 9.2\Delta z$		2	180	$\gamma 18.2\Delta z$
	3	-30		3	70	$\gamma 9.3\Delta z$		3	170	$\gamma 18.3\Delta z$
	4	-40		4	60	$\gamma 9.4\Delta z$		4	160	$\gamma 18.4\Delta z$
	5	-50		5	50	$\gamma 9.5\Delta z$		5	150	$\gamma 18.5\Delta z$

Table 3.1: Examples when when α is 10 and β^2 is 0.9. γ is the Lorentz factor of $\beta^2 = 0.9$ and Δz is the spatial discretization unit in the moving frame. n, m, and x are index of time step to visualize, space discretization, and time step to transform respectively.

when three space discretization sizes are same in 3 dimensional space ($\Delta x = \Delta y = \Delta z$). Since we have $0 \leq \beta < 1$, we have $\alpha \geq 2$. With the same analysis, α which is greater than 2 is sufficient to make x integer when $\Delta z \gg \Delta x,\ \Delta y$.

Table 3.1 shows an examples of time and z-coordinates when α is 10 and β^2 is 0.9. When we have $n = 0$, that is, at the initial time of the simulation in the moving frame, x has negative values when m is positive. This means the past data is required to visualize the result at the initial time. Also, when n is 200, the data of the head part of the beam ($m = 4$) comes from the past (x is 160 time step) and the data of the tail of the beam ($m = -4$) comes from the future (x is 240 time step). If we set the head position to the reference position, in other words, if we shift $m = 4$ to $m = 0$ (See Figure 3.6), the negative time at the initial time can be avoided.

In the implementation of the visualization, the simulation data which is front of the center can be stored for the visualization. For example, according to Table 3.1, when time t is $100\Delta t$ ($n = 100$), the data of the beam head should be saved at $t = 60\Delta t$. The visualization at $t = 100\Delta t$ is completed at $t = 140\Delta t$. Although, only longitudinal discretization is required but transversal discretization is not required. But since the transformation and discretization is used for visualization and several discretization data should be saved, the transversal discretization is used for efficiency of the visualization. The transversal discretization does not need to correspond to the FDTD discretization.

When we have time step 100, the length between $m = -5$ and $m = 5$ is $\gamma\Delta z (= \gamma 9.5\Delta z - \gamma 8.5\Delta z)$ in the laboratory frame. Since we have $\beta^2 = 0.9$, we have $\gamma^2 = 10 \Rightarrow \gamma = \frac{10}{\gamma}$. So the length between $m = -5$ and $m = 5$ is $\gamma\Delta z = \frac{10}{\gamma}\Delta z = \frac{1}{\gamma}(10\Delta z)$. This shows that the length in the laboratory frame L^* is equal to $\frac{L}{\gamma}$ where L is the length in the moving frame.

3.3.2 Time Discretization Method

This method uses same domain discretization with the computational domain discretization but uses new time discretization only for the Lorentz transformation. For the computational convenience, let the head of beam be the reference position as Figure 3.6.

As we discussed in Section 3.3.1, right side of the reference position is visualized from the past of the reference position visualization time and the left side is visualized from the future of the reference. In this method, the

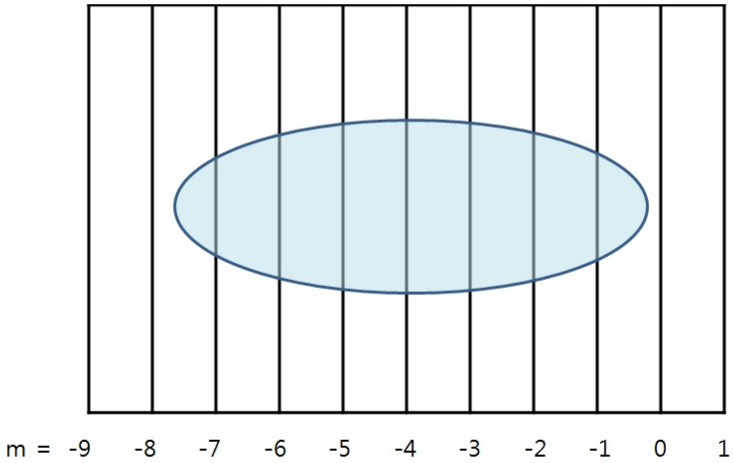

Figure 3.6: Schematic diagram of spatial discretization of a beam in a moving frame. There are many macroparticles in the blue and elliptic region. Particles are not described in the beam region.

reference is ahead of the beam head, the whole beam can be visualized

In order to make the left side of the Equation (3.5) constant, fix n which is the time step index for the visualization. Let $z = m\Delta z$ and $t = n\Delta t + \alpha'$ where $\alpha' > 0$. Then we have

$$\frac{\beta}{c}m\Delta z + (n\Delta t + \alpha') = n\Delta t \Rightarrow \alpha' = -\frac{\beta}{c}m\Delta z. \tag{3.8}$$

Since we have only negative m by the initial assumption, we have $\alpha' > 0$.

Then we have z-coordinate in the laboratory frame (lab frame) as following:

$$z^* = \gamma(m\Delta z + \beta c(n\Delta t + \alpha')) = \gamma(m(1-\beta^2)\Delta z + \beta cn\Delta t). \tag{3.9}$$

In this formula $\gamma\beta cn\Delta t$ denotes the position of the head in the laboratory

$n=0$	m	α'	relative z^*
	-9	$\frac{1}{c}9\sqrt{0.9}\Delta z$	$-\gamma 0.9\Delta z$
	-8	$\frac{1}{c}8\sqrt{0.9}\Delta z$	$-\gamma 0.8\Delta z$
	-7	$\frac{1}{c}7\sqrt{0.9}\Delta z$	$-\gamma 0.7\Delta z$
	-6	$\frac{1}{c}6\sqrt{0.9}\Delta z$	$-\gamma 0.6\Delta z$
	-5	$\frac{1}{c}5\sqrt{0.9}\Delta z$	$-\gamma 0.5\Delta z$
	-4	$\frac{1}{c}4\sqrt{0.9}\Delta z$	$-\gamma 0.4\Delta z$
	-3	$\frac{1}{c}3\sqrt{0.9}\Delta z$	$-\gamma 0.3\Delta z$
	-2	$\frac{1}{c}2\sqrt{0.9}\Delta z$	$-\gamma 0.2\Delta z$
	-1	$\frac{1}{c}\sqrt{0.9}\Delta z$	$-\gamma 0.1\Delta z$
	0	$\frac{1}{c}0.0\Delta z$	0.0
	1	$-\frac{1}{c}\sqrt{0.9}\Delta z$	$\gamma 0.1\Delta z$

Table 3.2: Examples when when β^2 is 0.9. γ is the Lorentz factor of $\beta^2 = 0.9$ and Δz is the spatial discretization unit in the moving frame. n, m, and α' are index of time step to visualize, space discretization, and time variance to transform respectively.

frame and $\gamma m(1-\beta^2)\Delta z$ denotes the relative distance from the reference position by m and α' in the laboratory frame. Table 3.2 shows examples of time and z-coordinates when β^2 is 0.9.

Chapter 4

The Implementation of Code SPACE

In this chapter, we describe the parallel electromagnetic PIC software we have been developing. Although we are developing a serial code for the purpose of debugging, we describe only the parallel code. The parallel code is written in C++ and using Message Passing Interface (MPI).

4.1 Code Structure and Implementation

The code is developed in C++ utilizing the advantages of Objected-Oriented programming. The code is composed of three major parts. The first part, FieldSolver class, contains the field solvers such as the FDTD solver or an elliptic solver. The second part, ParticleMover class, contains solvers for the Newton-Lorentz equation. This class also includes various physics models describing particle interactions and transformations by the atomic physics processes and drift velocity restriction for plasma. The code is capable of tracking numerous particle species. Finally, the third, TimeController class, controls the above classes and any miscellaneous classes such as classes performing the visualization of electromagnetic fields and particle data. The visualization is done using the visualization software called VisIt [18]. Since the main classes of the code are connected via the interface classes, the code can easily be extended by implementing additional functions and physics models. For convenience of a new problem setup, the initialization routines use XML (eXtensible Markup Language). At the initial time step, the FDTD solver solves the Poisson's equation in the Maxwell's equation (Equation 3.1c) from the initial charge distribution. When the Dirichlet boundary condition is imposed, the Poisson's equation is solved by PETSc [19] library.

4.2 Parallelization Methods

The electromagnetic PIC code is parallelized using a hybrid MPI / OpenMP programming for distributed memory multi-core supercomputers. FieldSolver uses domain decomposition for solving the Maxwell's equations or the Poisson's equation. ParticleMover uses a decomposition of particles that is independent of FieldSolver domain decomposition. Namely, particles in a parallel computing node can be distributed in the whole computational domain. As the distribution of particles is usually very non-uniform in the space, such decomposition maximizes the load balance. The described parallel decomposition minimizes the CPU computing time but require a large amount of communications between FieldSolver and ParticleMover. We have adopted ideas from the sparse matrix storage to minimize the amount of communications and send field data to ParticleMover from only those computational cells that contain macroparticles.

4.3 Poisson's Equation Solver for Electrostatics

The main difference of the electrostatic part of SPACE from the electromagnetic part of SPACE is that the electrostatic code solves the Poisson's equation instead of the Maxwell's equations. For the Dirichlet boundary condition, PETSc [19] library is used and the solver including the gradient of the potential, charge assign, and field interpolation are implemented by Jun Ma and Xingyu Wang [20]. For the periodic boundary condition, the Fourier transformation can be used. The elliptic solver with periodic boundary condition is implemented by Kwangmin Yu using FFTW [21] library. In the following sections, we describe the mathematical formulae and background to be used for the Discrete Fourier Transformation (DFT) method.

4.3.1 Discrete Fourier Transform (DFT)

Let W_N be $e^{-2\pi i/N}$. Then the DFT coefficient X of x is defined as following in $3D$ $(N_1 \times N_2 \times N_3)$ discretized domain:

$$X(k_1, k_2, k_3) = \sum_{n_1=0}^{N_1-1} \sum_{n_2=0}^{N_2-1} \sum_{n_3=0}^{N_3-1} x(n_1, n_2, n_3) W_{N_1}^{n_1 k_1} W_{N_2}^{n_2 k_2} W_{N_3}^{n_3 k_3} \tag{4.1}$$

where $k_1 = 0, 1, \cdots, N_1 - 1$, $k_2 = 0, 1, \cdots, N_2 - 1$, and $k_3 = 0, 1, \cdots, N_3 - 1$.

The inverse DFT with the DFT coefficients is defined as following:

$$x(n_1, n_2, n_3) = \frac{1}{N_1 N_2 N_3} \sum_{k_1=0}^{N_1-1} \sum_{k_2=0}^{N_2-1} \sum_{k_3=0}^{N_3-1} X(k_1, k_2, k_3) W_{N_1}^{-n_1 k_1} W_{N_2}^{-n_2 k_2} W_{N_3}^{-n_3 k_3} \tag{4.2}$$

where $n_1 = 0, 1, \cdots, N_1 - 1$, $n_2 = 0, 1, \cdots, N_2 - 1$, and $n_3 = 0, 1, \cdots, N_3 - 1$.

The DFT pair can be symbolically represented as following:

$$x(n_1, n_2, n_3) \Leftrightarrow X(k_1, k_2, k_3) \tag{4.3}$$

The Fourier transformation has many good properties such as transforming derivatives or integrals to algebraic computation. These properties hold on DFT. Following Lemma is introduced without proof since the property has essential role for the Poisson's equation solver by DFT.

Lemma 4.3.1 (Circular Shift Property)**.** *If* $x(n_1, n_2, n_3) \Leftrightarrow X(k_1, k_2, k_3)$ *in* $3D$ $(N_1 \times N_2 \times N_3)$ *discretized domain, then* $x(n_1 + m_1, n_2 + m_2, n_3 + m_3) \Leftrightarrow X(k_1, k_2, k_3) W_{N_1}^{-k_1 m_1} W_{N_2}^{-k_2 m_2} W_{N_3}^{-k_3 m_3}$

4.3.2 The Poission's Equation and its Solution by DFT

When we have the Poisson's equation

$$\nabla^2 \phi = -\rho, \tag{4.4}$$

the equation is discretized as following

$$
\begin{aligned}
&\left(\frac{\partial^2}{\partial x^2}+\frac{\partial^2}{\partial y^2}+\frac{\partial^2}{\partial z^2}\right)\phi(x,y,z) \simeq \\
&\frac{1}{{h_1}^2}\left(\phi(n_1+1,n_2,n_3)+\phi(n_1-1,n_2,n_3)-2\phi(n_1,n_2,n_3)\right)+ \\
&\frac{1}{{h_2}^2}\left(\phi(n_1,n_2+1,n_3)+\phi(n_1,n_2-1,n_3)-2\phi(n_1,n_2,n_3)\right)+ \\
&\frac{1}{{h_3}^2}\left(\phi(n_1,n_2,n_3+1)+\phi(n_1,n_2,n_3-1)-2\phi(n_1,n_2,n_3)\right)=-\rho(n_1,n_2,n_3)
\end{aligned}
\tag{4.5}
$$

in three dimensional space.

By applying DFT in both side, we have

$$
\begin{aligned}
&\frac{1}{{h_1}^2}\left(\hat{\phi}(k_1,k_2,k_3)W_{N_1}^{-k_1}+\hat{\phi}(k_1,k_2,k_3)W_{N_1}^{k_1}-2\hat{\phi}(k_1,k_2,k_3)\right)+ \\
&\frac{1}{{h_2}^2}\left(\hat{\phi}(k_1,k_2,k_3)W_{N_2}^{-k_2}+\hat{\phi}(k_1,k_2,k_3)W_{N_2}^{k_2}-2\hat{\phi}(k_1,k_2,k_3)\right)+ \\
&\frac{1}{{h_3}^2}\left(\hat{\phi}(k_1,k_2,k_3)W_{N_3}^{-k_3}+\hat{\phi}(k_1,k_2,k_3)W_{N_3}^{k_3}-2\hat{\phi}(k_1,k_2,k_3)\right)=-\hat{\rho}(k_1,k_2,k_3)
\end{aligned}
\tag{4.6}
$$

$\Rightarrow$

$$
\begin{aligned}
&\frac{1}{{h_1}^2}\left(W_{N_1}^{-k_1}+W_{N_1}^{k_1}-2\right)\hat{\phi}(k_1,k_2,k_3)+ \\
&\frac{1}{{h_2}^2}\left(W_{N_2}^{-k_2}+W_{N_2}^{k_2}-2\right)\hat{\phi}(k_1,k_2,k_3)+ \\
&\frac{1}{{h_3}^2}\left(W_{N_3}^{-k_3}+W_{N_3}^{k_3}-2\right)\hat{\phi}(k_1,k_2,k_3)=-\hat{\rho}(k_1,k_2,k_3)
\end{aligned}
\tag{4.7}
$$

$\Rightarrow$

$$\left(\frac{4}{{h_1}^2}\sin^2\left(\frac{\pi k_1}{N_1}\right)+\frac{4}{{h_2}^2}\sin^2\left(\frac{\pi k_2}{N_2}\right)+\frac{4}{{h_3}^2}\sin^2\left(\frac{\pi k_3}{N_3}\right)\right)\hat{\phi}(k_1,k_2,k_3)$$
$$=\hat{\rho}(k_1,k_2,k_3). \quad (4.8)$$

Let

$$\hat{L}(k_1,k_2,k_3)=$$
$$\frac{4}{{h_1}^2}\sin^2\left(\frac{\pi k_1}{N_1}\right)+\frac{4}{{h_2}^2}\sin^2\left(\frac{\pi k_2}{N_2}\right)+\frac{4}{{h_3}^2}\sin^2\left(\frac{\pi k_3}{N_3}\right). \quad (4.9)$$

Then we have

$$\hat{\phi}(k_1,k_2,k_3)=\hat{\rho}(k_1,k_2,k_3)/\hat{L}(k_1,k_2,k_3). \quad (4.10)$$

Finally, by applying IDFT to $\hat{\phi}(k_1,k_2,k_3)$, we have the solution of the Poisson's equation as following:

$$\phi(n_1,n_2,n_3)=$$
$$\frac{1}{N_1N_2N_3}\sum_{k_1=0}^{N_1-1}\sum_{k_2=0}^{N_2-1}\sum_{k_3=0}^{N_3-1}\hat{\phi}(k_1,k_2,k_3)W_{N_1}^{-n_1k_1}W_{N_2}^{-n_2k_2}W_{N_3}^{-n_3k_3} \quad (4.11)$$

where $n_1=0,1,\cdots,N_1-1$, $n_2=0,1,\cdots,N_2-1$, and $n_3=0,1,\cdots,N_3-1$.

4.4 Verification I: TM Waves in Rectangular Waveguides

As a first step of verification, the FDTD scheme is tested. Analytic solutions of transversal magnetic waves in rectangular waveguides are well known. The analytic solutions of TM_{11} mode are described followings [22]:

$$\begin{cases} E_x = & \frac{\beta}{h^2}\left(\frac{\pi}{a}\right)\cos\left(\frac{\pi}{a}x\right)\sin\left(\frac{\pi}{b}y\right) & \sin(\omega t-\beta z) \\ E_y = & \frac{\beta}{h^2}\left(\frac{\pi}{b}\right)\sin\left(\frac{\pi}{a}x\right)\cos\left(\frac{\pi}{b}y\right) & \sin(\omega t-\beta z) \\ E_z = & \sin\left(\frac{\pi}{a}x\right)\sin\left(\frac{\pi}{b}y\right) & \cos(\omega t-\beta z) \\ H_x = & -\frac{\omega\epsilon_0}{h^2}\left(\frac{\pi}{b}\right)\sin\left(\frac{\pi}{a}x\right)\cos\left(\frac{\pi}{b}y\right) & \sin(\omega t-\beta z) \\ H_y = & \frac{\omega\epsilon_0}{h^2}\left(\frac{\pi}{a}\right)\cos\left(\frac{\pi}{a}x\right)\sin\left(\frac{\pi}{b}y\right) & \sin(\omega t-\beta z) \\ H_z = 0 & & \end{cases} \tag{4.12}$$

where $h = \left(\frac{\pi}{a}\right)^2 + \left(\frac{\pi}{b}\right)^2$ and $\beta = \sqrt{\omega^2\mu_0\epsilon_0 - h^2}$.

Hence the FDTD solver is compared with the analytic solution of TM_{11} mode wave in the waveguide of $a = 0.256m$, $b = 0.256m$, and $\omega = 4.9\pi \times 10^9 Hz$. For simplicity, same mesh size in x, y, and z coordinates are chosen and 75% of the CFL condition of the FDTD ($\Delta t \le \frac{1}{v_{\max}\sqrt{\frac{1}{\Delta x^2}+\frac{1}{\Delta y^2}+\frac{1}{\Delta z^2}}}$ where $v_{\max}$ is the maximum wave phase velocity, typically the light speed.) The errors are measured in L_2 norm. The convergence result is shown in Table 4.1.

4.5 Verification II: Space Charge

The space charge effect of two bunches is tested.

Mesh size	0.016^3	0.008^3	0.004^3	0.002^3	0.001^3
E_x	9.12081E-05	1.34378E-05	1.70542E-06	2.12644E-07	2.66546E-08
Ratio		6.787428002	7.879466642	8.020071105	7.977759936
Order		2.762864989	2.978097977	3.003615027	2.995983711
E_y	9.12081E-05	1.34378E-05	1.70542E-06	2.12644E-07	2.66546E-08
Ratio		6.787428002	7.879466642	8.020071105	7.977759936
Order		2.762864989	2.978097977	3.003615027	2.995983711
E_z	4.84961E-05	7.10743E-06	9.1523E-07	1.14437E-07	1.43798E-08
Ratio		6.823296184	7.765731018	7.997675577	7.958177443
Order		2.770468842	2.957121737	2.99958076	2.992438067
H_x	2.43189E-07	1.89962E-08	2.19599E-09	2.77576E-10	3.4388E-11
Ratio		12.80198145	8.65040369	7.911310776	8.071885541
Order		3.678295218	3.112767461	2.983916746	3.012905717
H_y	2.43189E-07	1.89962E-08	2.19599E-09	2.77576E-10	3.4388E-11
Ratio		12.80198145	8.65040369	7.911310776	8.071885541
Order		3.678295218	3.112767461	2.983916746	3.012905717
H_z	1.5425E-22	2.31812E-23	3.95174E-24	6.81385E-25	1.19542E-25
Ratio		6.654099011	5.866074185	5.799569993	5.699963193
Order		2.734243333	2.552395316	2.535945936	2.510952603

Table 4.1: Convergence test of the FDTD.

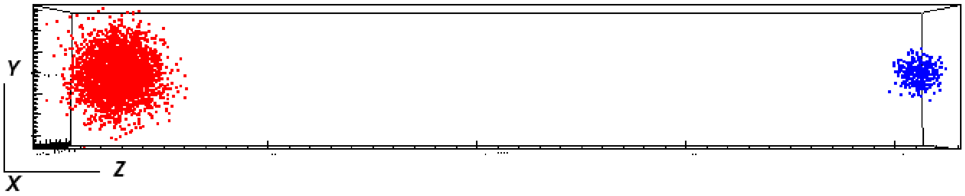

Figure 4.1: Code Validation

In Fig. 4.1, red particles in the left side describe 3000 particles and each particle has $-1.602e-9$ (C) charge and $9.109e-10$ (Kg) mass. On the other hand, blue particles in the right side describe 300 particles and each particle has $-1.602e-12$ (C) charge and $9.109e-24$ (Kg) mass. The distance between two particle bunch is 0.04 meter. Since red particles are sufficiently headier than blue particles, the red particle bunch rarely moves in the simulation. This simulates two charge particle, which the left side particle represents $4.806e-6$ (C), $2.7327e-6$ (Kg) and the right side particle represents $4.806e-10$ (C), $2.7327e-21$ (Table 4.2).

According to the analytic computation, the right side particle should gain $(0, 0, 2.0604e+6)$ (m/s) at the initial time. From the simulation, we obtained that the right side particles in the simulation gain $(-6.68e+03, 1.31e+04, 2.0624e+06)$ (m/s) average velocity at the initial time. When we simulated again with 3000 blue particles, we obtained $(-6.74e+02, 1.35e+03, 2.0604e+06)$ (m/s) average velocity (Table 4.3). In the simulation, two bunches are not symmetric, it produced non-zero velocity along x and y coordinates. However, we obtained accurate z directional velocity. When ten times more macro particles are used the accuracy increases by ten. It shows that the particle discretization has linear accuracy because Cloud-in-Cell method (first order interpolation) is used.

4.6 Verification III: Acceleration

In this test, a stationary bunch is accelerated by the electric field. After 498.31 picosecond (2300 time steps), the analytic computation and the

	Left Bunch	Right Bunch
Charge/Particle	-1.602e-9 (C)	-1.602e-12 (C)
Mass/Particle	-1.602e-9 (C)	-1.602e-12 (C)
# of Particles	3000	300 or 3000

Table 4.2: Simulation parameters.

# of Particles of the Right	Average Velocity (m/s)
300	(-6.68e+3, 1.31e+4, 2.0604e+6)
3000	(-6.74e+2, 1.35e+3, 2.0604e+6)
Analytic Velocity	(0.0, 0.0, 2.0604e+6)

Table 4.3: Simulation results.

simulation result are compared.

Table 4.4 shows the parameter of the simulation. Table 4.5 shows the result of the simulation. The result shows good consistency of the simulation with the analytic computation.

Parameter	Value
Charge	-1.602e-6 (C)
Mass	9.109e-12 (Kg)
Electric Field Intensity	2e+9 (V/m)
Initial Position of Bunch	0.02 (m)
Initial Velocity of Bunch	0 (m/s)
# of Particles	3000

Table 4.4: Simulation parameters.

	Analytic Computation	Simulation	Relative Error
Position (m)	-1.602e-6 (C)	2.0259e-2	0.1%
Velocity (m/s)	9.5454e+5	9.5750e+5	0.3%

Table 4.5: Simulation results.

4.7 Verification IV: Plasma Oscillation

Plasma oscillation is tested in a gas-filled RF cavity. A proton beam passes through a hydrogen gas-filled RF cavity. The proton beam ionizes the gas and generates plasma. Because of the high pressure in the cavity, the thermal velocity of the plasma is ignored. That is, the cold plasma is used. The beam-induced plasma oscillates. The plasma oscillation frequency of cold plasma is described by ω

$$\omega = \sqrt{\frac{ne^2}{m\epsilon_0}} \tag{4.13}$$

where n, e, m, and ϵ_0 denote the number density of particle in unit cm^{-3}, the charge of particle, mass of particle, and the permittivity of free space, respectively [23].

The plasma oscillation frequency $\omega_p = \sqrt{{\omega_e}^2 + {\omega_i}^2}$ where ω_e and ω_i are the plasma frequency of electron and ion respectively. When the ion plasma frequency is negligible, $\omega_p \simeq \omega_e \simeq 2\pi \cdot 8980\sqrt{n_e}$ where n_e is the electron number density in unit cm^{-3} [23]. Table 4.6 shows the parameters used in the simulation. The electric field intensity (V/m) at the cavity center is recorded as shown in Fig. 4.2.

After the simulation, the electron number density is 3.742e+13 cm^{-3}.

Parameters	Values
Kinetic Energy of beams	400 MeV
Beam distribution	Uniform
Beam velocity	2.14e+8 m/s ($\beta = 71\%$)
Beam Length	1 cm
Beam Radius	1 mm
H_2 gas pressure	100 atm
dE/dx	6.33 MeVcm^2/g
Average Ionization Energy	36.2 eV
Population per Bunch	2.546×10^8

Table 4.6: Parameters of plasma oscillation test.

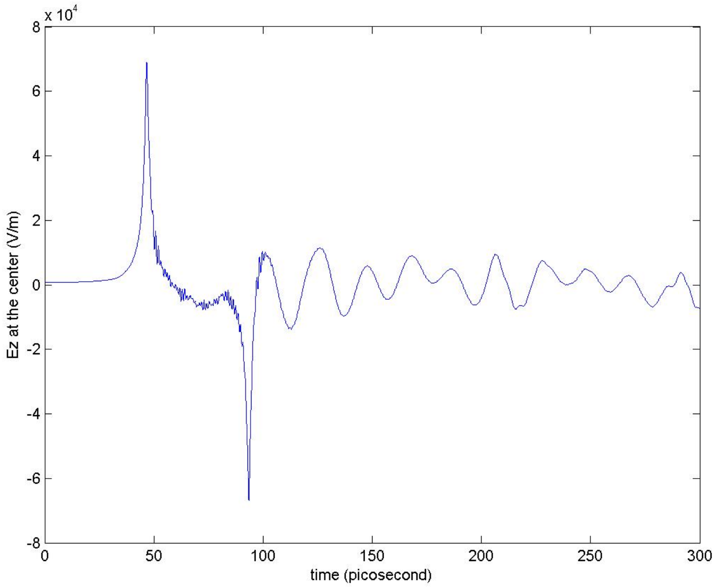

Figure 4.2: The electric field intensity at the cavity center.

According to Equation 4.13, ω_p is 3.451 Hz. On the other hand, the average oscillation period in Fig. 4.2 is 347 time steps. Since one time step is 2.0048e-011 second, the oscillation period is 5.7775e-14. Therefore, the plasma frequency ω_{ps} by the simulation is 3.134e+11. The relative error is 9.2%. Since the plasma distribution is affected by the electromagnetic wave induced by the beam, the electron density in the cavity center is different from the density $3.742e + 13\ cm^{-3}$. This discrepancy is the source of the error. In spite of the relative error, the simulation is consistent with the plasma frequency theory.

4.8 Scalability Test and Running Time Analysis

The weak-scalability test and the running time record of internal module of the electromagnetic code of SPACE is accomplished on IBM Blue Gene P in BNL. SPACE uses two different decomposition. One is for fields and the other is for particles. Because of the MPI decomposition method of SPACE and the fundamental reason of electromagnetic PIC, the code has good weak-scalability on particle decomposition, but poor weak-scalability on field decomposition. In electromagnetic PIC, more mesh grid requires more computations of particle for current update.

Both Table 4.7 and Table 4.8 show good weak-scalability on particles (Particle Moving Time). In Table 4.8, the current update time increases rapidly in particle moving part but the current update time is almost constant in Table 4.7. This is because finer mesh grid causes more current update of particle. The increase of fetching field time in Table 4.8 is caused by the MPI decomposition method used in the code SPACE since the global field

# of MPI nodes	64	128	256
# of mesh grids	64^3	64^3	64^3
# of particles	64^3	2×64^3	4×64^3
Field Solving Time	0.003487	0.001899	0.019620
Particle Moving Time	0.309206	0.311139	0.319392
Init Memory	0.013589	0.013749	0.013749
Position Update	0.011562	0.011639	0.011654
Current Update	0.117648	0.119792	0.123630
Current Update Ratio (%)	38.0484	38.5011	38.7079
Fetching Fields	0.150998	0.150624	0.154907
Fetching Fields Ratio (%)	48.8341	48.4105	48.5006
Velocity Computing	0.014667	0.014590	0.014711
Running Time of 20 time steps	6.261	6.264	6.786

Table 4.7: Scalability test result of fixed grid number and variable particle number.

values should be distributed to all MPI nodes.

In spite of the weakness of poor weak-scalability on field decomposition, the code has good weak-scalability in actually simulations because thousand times more particle discretization is used than the discretization of mesh grid.

# of MPI nodes		64	128	256
# of mesh grids		$64 \times 64 \times 64$	$128 \times 64 \times 64$	$128 \times 128 \times 64$
# of particles		64^3	2×64^3	4×64^3
Field Solving Time		0.003487	0.003594	0.013197
Particle Moving Time		0.309206	0.592586	1.198720
	Init Memory	0.013589	0.026952	0.053481
	Position Update	0.011562	0.011561	0.011624
	Current Update	0.117648	0.238719	0.501392
	Current Update Ratio (%)	38.0484	40.2843	41.8273
	Fetching Fields	0.150998	0.299991	0.616706
	Fetching Fields Ratio (%)	48.8341	50.6240	51.4470
	Velocity Computing	0.014667	0.014703	0.014730
Running Time of 20 time steps		6.261	11.928	24.245

Table 4.8: Scalability test result of variable grid number and variable particle number.

Chapter 5

Application I: Simulation of Beam-Induced Plasma in a Gas-Filled RF Cavity

5.1 Introduction

Using muons is an attractive choice for realizing a multi-TeV lepton collider and producing a well-defined intense neutrino beam for neutrino experiment. Because muons are a tertiary particle in production, the phase space volume of muon beam needs to be shrunken to fit into the accelerator optics. Ionization cooling is a viable method for low energy muons to quickly cool down the beam temperature within their lifetime [16]. Muons proparate through an ionization material with strong magnetic focusing and loose their kinetic energy via ionization process. The lost energy is immediately and adiabatically recovered by RF cavities. Better cooling efficiency is obtained with higher RF gradient. However, the achievable RF gradient is limited by the presence of a static magnetic field in a vacuum cavity because the density of dark current, which is a seed of electric breakdown in an RF cavity, is increased by magnetic focusing [24]. To resolve this problem, a high-pressure hydrogen gas-filled RF (HPRF) cavity was proposed. Hydrogen gas serves the dual role: it buffers the dark current and serves as the ionization material for the cooling process. A novel ionization cooling channel by using the dual function cavity was proposed and its high cooling efficiency was demonstrated via simulations [25, 26].

Experimental efforts have been made to characterize the HPRF cavity (Fig. 5.3) by using intense proton beams in the Mucool Test Area (MTA) at Fermilab [27, 28, 29]. In particular, the plasma loading effect has been investigated [27]. Plasma loading takes place when a beam-induced gas plasma in the HPRF cavity absorbs the stored energy of the electromagnetic field in the cavity and causes significant reduction of the electric field. The plasma loading depends on the amount and mobility of charged particles in the gas. To decrease the plasma loading effect, adding a small amount of dopant to the hydrogen gas was proposed and successfully tested in experiments.

To better utilize experimental results and enable the design of a practical ionization cooling channel, a new algorithm to resolve plasma chemistry and plasma loading have been developed and implemented in the code SPACE [30]. The code reproduces complex plasma chemistry processes, including hydrogen recombination, electron attachment, and various recombination mechanisms that depend on plasma temperature. The plasma temperature is determined by a localized electric field, generated by the plasma dynamics and the wakefield of the intense beam as well as the RF field.

A big challenge in such a plasma simulation is the need to simulate a

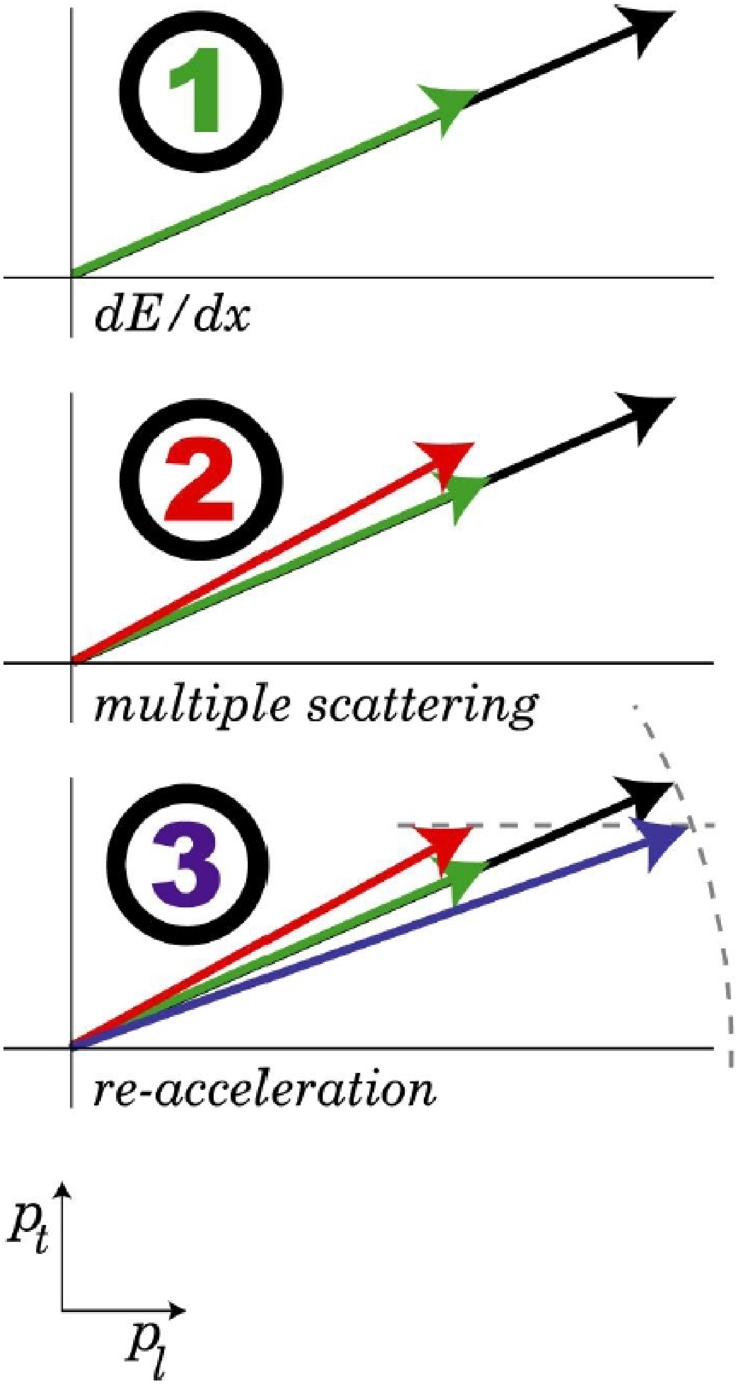

Figure 5.1: Schematic of muon ionization cooling from [31].

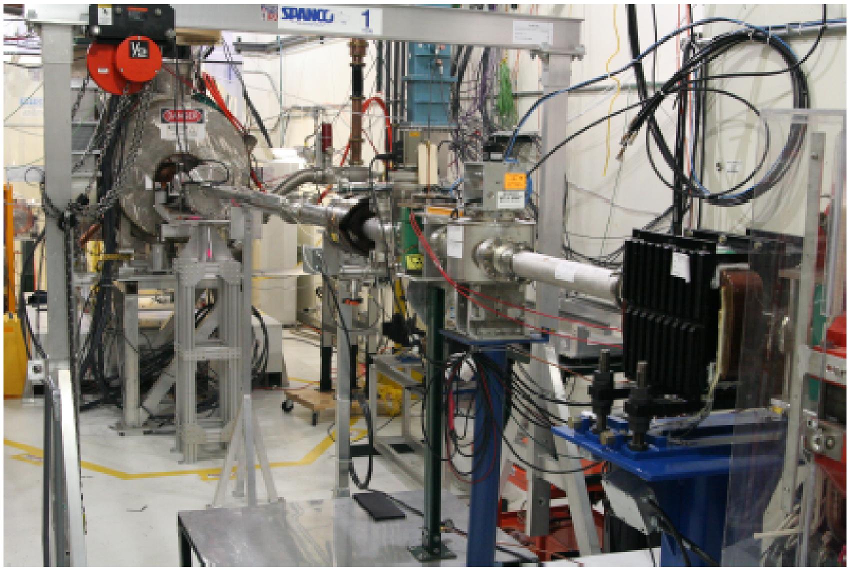

Figure 5.2: The MuCool Test Area (MTA) at Fermilab focused on R&D toward operating RF cavities in strong magnetic field [28].

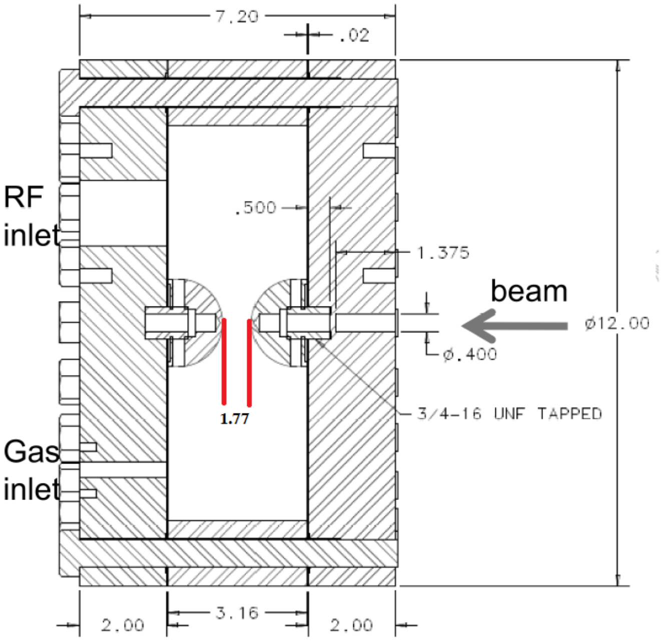

Figure 5.3: Cross sectional drawing of the HPRF cavity from [28]. The unit is centimeter. Optical and probe ports which are located on the face with the RF port is omitted.

very wide range of time scales, extending from the wake field characteristic time of picoseconds to millisecond intervals typical for plasma neutralization processes. This problem was resolved by utilizing our new algorithms that perform simulations of the particle beam and plasma at different computational time steps. The main purpose of this paper is to validate new simulation algorithms by comparing with experimental results. The second goal is quantification of uncertain values characterizing plasma processes. Even though the recombination rates and the attachment time were measured experimentally, the range of measurements were restricted to a narrow region and the measured values contained significant uncertainties due to experimental errors and the use of indirect measurement methods [28]. Comparison of simulation results with experimental data helps to improve the estimate of parameters characterizing plasma properties and extend their values beyond the current experimental range.

5.2 Models and Numerical Algorithms for Atomic Physics Processes in Plasma in Gas-Filled RF Cavity

5.2.1 Plasma formation

As an intense proton beam propagates in the high-pressure gas-filled RF (HPRF) cavity, plasma is created by ionization of hydrogen gas molecules due to collisions with beam particles [32, 33]. Some generated electrons have enough kinetic energy to cause secondary ionization. The process is described as

$$\begin{aligned} p + H_2 &\rightarrow p + {H_2}^+ + e^- \\ e^- + H_2 &\rightarrow {H_2}^+ + 2e^- \end{aligned} \tag{5.1}$$

where p, H_2, and e are a beam particle (proton), hydrogen molecule, and electron, respectively.

The number of electron-ion pairs N_{pairs}, produced in an elementary volume dV of the cavity during time dt, is estimated based on the stopping power of the proton beam in hydrogen gas:

$$N_{pairs} = \frac{N_b}{W_i} \left(\frac{dE}{dx}(\mathbf{x}(t)) \right) \rho h. \tag{5.2}$$

Here (dE/dx) is a normalized stopping power of a beam particle per unit density of the absorber material, ρ, h, W_i, N_b, and $\mathbf{x}(t)$ denote the gas mass density, length of the volume dV along the beam path, average ionization energy, the number of beam particles that traverse dV in time dt, and position of the beam particle at time t, respectively. In Eq. (5.2), W_i accounts for both processes described in (5.1). The Bethe-Bloch formula [16] is used for calculating the stopping power. The stopping power is a function of the beam particle momentum [28]. The ionization-induced reduction of momentum of beam particles changes the stopping power and the ionization rate (5.2).

The Bethe-Bloch formula is described as following:

$$-\frac{dE}{dx} = 4\pi \frac{r_e^2 m_e c^2 z^2}{\beta^2} n \left(\frac{1}{2} \ln \frac{2 m_e c^2 \gamma^2 \beta^2 T_{\max}}{I^2} - \beta^2 - \frac{\delta(\beta)}{2} - \frac{C(\beta)}{Z} \right)$$

where

$$\begin{cases}
\beta : \text{the normalized particle speed by the light speed} \\
r_e : \text{classical electron radius}(2.82 \times 10^{-13}\ cm) \\
m_e : \text{rest mass of electron} \\
z : \text{charge of incident particle} \\
n : \text{(electron number density)} = \dfrac{N_A Z \rho}{A} \\
T_{\max} : \text{maximum energy transfer to a single electron} \\
N_A : \text{Avogadro number} \\
Z : \text{atomic number} \\
\rho : \text{density of the material} \\
A : \text{molar mass constant } (ex.H_2 = 1.00794 \times 2 = 2.01588\ g/\text{mol}) \\
I : \text{mean excitation potential} \\
\delta : \text{density correction} \\
C : \text{shell correction,}
\end{cases}$$

and $T_{\max} = 2 m_e c^2 \beta^2 \gamma^2 \left(1 + 2\gamma \frac{m_e}{M} + \frac{m_e^2}{M^2}\right)^{-1}$. $T_{\max}$ is often approximated by $2 m_e c^2 \beta^2 \gamma^2$. The δ arises from the screening of remote electrons by close electrons, which results in a reduction of energy loss for higher energies. The effect is largest in dense matter, that is, in solids and liquids. The C is only important for low energies where the particle velocity has the same order of magnitude as the "velocity" of the atomic electrons. So we can ignore this correction. The secondary ionization in the Equation 5.1 is included in I by adjusting the value.

The the stopping power of a beam particle depends on the momentum of the particle as shown in Fig. 5.4 and Equation (5.3) Also the stopping power variation effect of beam passing in the RF cavity is about 18% [34]. Therefore, the code SPACE implemented not only ionization process but also the kinetic energy reduction of beam particles.

Let $-\Delta E = -\frac{dE}{dx} = f(v)$. Then we have $-\Delta E^{n+1/2} = -\frac{E^{n+1}-E^{n}}{x^{n+1}-x^{n}} = f(v^{n+1/2})$. Followings describe particle position and velocity update sequence in a time step.

(1) Calculate x^{n+1} with x^{n} and $v^{n+1/2}$.

(2) Calculate $v^{n+3/2}$ with E, B, and $v^{n+1/2}$.

(3) Calculate $\Delta E^{n+3/2}$ with $v^{n+3/2}$.

(4) Update $v^{n+3/2}$ by $\Delta E^{n+3/2}$. Decrease the kinetic energy of the particle by $\Delta E^{n+3/2}$. The decrease of the kinetic energy preserve the direction of the particle.

In conjunction with the Maxwell's equation and the Lorentz equation (Fig. 2.9, 2.15), following is the whole process to produce ionized charges and update reduced velocity of the beam particles.

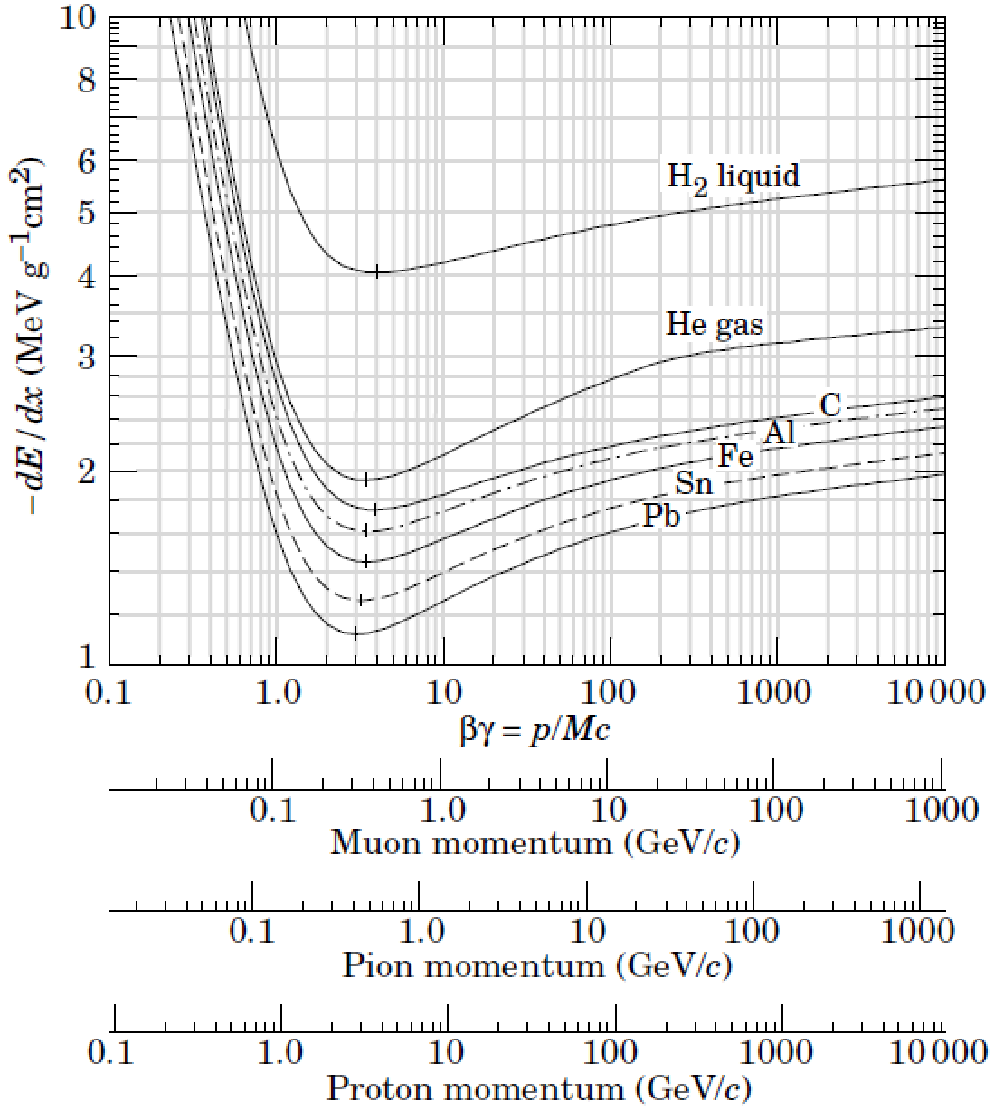

Figure 5.4: The average stopping power of particle momentum in various materials [35]

(1) Calculate $\mathbf{E}^{n+1} = \mathbf{E}^{n} + \frac{\Delta t}{\epsilon}\left(\nabla \times \mathbf{H}^{n+1/2} - \mathbf{J}^{n+1/2}\right)$.

(2) Calculate $\mathbf{H}^{n+3/2} = \mathbf{H}^{n+1/2} + \frac{\Delta t}{\mu}\left(-\nabla \times \mathbf{E}^{n+1}\right)$ by using FDTD solver.

(3) Calculate $\mathbf{x}^{n+1} = \mathbf{x}^{n} + \Delta t \mathbf{v}^{n+1/2}$.

(4) Generate ion-electron pairs by the ionization with x^n, x^{n+1}, and $\Delta E^{n+1/2}$.

(5) Calculate $J^{n+1/2}$ by using $\mathbf{x}^{n+1}$ and $\mathbf{x}^{n}$ with rigorous charge conservation scheme.

(6) Update $\mathbf{E}^{n+1}$ by subtracting $\frac{\Delta t}{\epsilon}\mathbf{J}^{n+1/2}$ on itself.

(7) Gather $\mathbf{E}^{n+1}$ and $\mathbf{H}^{n+1}$ to a particle. Let $\mathbf{E}_p^{n+1}$ and $\mathbf{H}_p^{n+1}$ be electric and magnetic field intensity on a particle respectively.

(8) Calculate $\mathbf{v}^{n+3/2} = \mathbf{v}^{n+1/2} + \frac{q\Delta t}{m}\left(\mathbf{E}_p^{n+1}(\mathbf{x}^{n+1}) + \left(\frac{\mathbf{v}^{n+3/2}+\mathbf{v}^{n+1/2}}{2} \times \mathbf{B}_p^{n+1}(\mathbf{x}^{n+1})\right)\right)$ using Boris scheme where q is the particle charge and m is the particle mass.

(9) Calculate $\Delta E^{n+3/2}$ with $v^{n+3/2}$.

(10) Update $v^{n+3/2}$ by $\Delta E^{n+3/2}$.

The algorithms described in section 3.2.1 and 3.2.2 are used for the sequence (4).

At high pressures over 20 atm, typical for the HPRF cavity, the H_2^+ ions quickly form other clusters of hydrogen [32]:

$$\begin{aligned} H_2^+ + H_2 &\rightarrow {H_3}^+ + H \\ H_{j-2}^+ + 2H_2 &\rightleftharpoons {H_j}^+ + H_2 \ (j = 5, 7, 9, \ldots). \end{aligned} \tag{5.3}$$

5.2.2 Plasma Loading

Due to high frequency collisions with neutral gas atoms, plasma electrons and ions reach their equilibrium drift speeds in a short period of time, and drift by the external RF field [27]. The average energy loss by one plasma particle pair during one RF cycle, called dw, was introduced in [27, 29]. When the RF field is given by $E_0 \sin(\omega t)$, where E_0, ω, and t denote the amplitude of the RF cycle, angular frequency of the RF field, and time, respectively, dw is

$$dw = q \int_0^T \left(p_e v_e + v_+ + (1 - p_e) v_-\right) E_0 \sin(\omega t) dt. \tag{5.4}$$

Here subscripts "e", "+", and "-" denote electron, positive ion (hydrogen), and negative ion (dopant), respectively, and q, T, and v, are the particle charge, the RF field period, and the drift velocity of a charged particle. The coefficient p_e denotes relative population of electrons in the total negative charges. By the attachment process, the electron population in the plasma becomes less than one. In pure hydrogen gas filled case, p_e is equal to 1. When the drift velocity of charges has the form $v = \mu E_0 \sin(\omega t)$ where μ is the mobility of the charge, Equation (5.4) becomes

$$dw = q \int_0^T \left(p_e \mu_e + \mu_+ + (1 - p_e) \mu_-\right) E_0^2 \sin^2(\omega t) dt. \tag{5.5}$$

The mobility or drift velocity of electrons in pure hydrogen gas has been well studies. It is represented as a function of $X = (E/P)$, the ratio of electric field intensity to the gas pressure [36, 37]. Numerical simulations of SPACE use

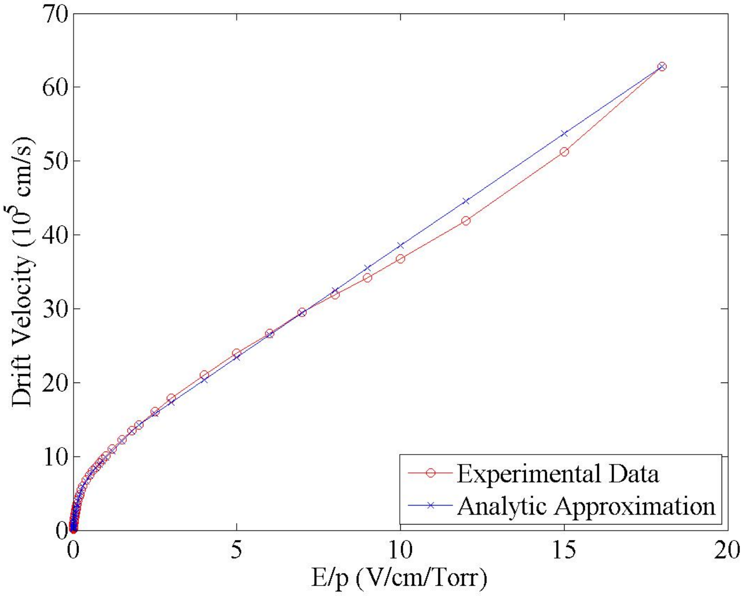

Figure 5.5: The electron draft velocity from experiment [37] and the approximation used in SPACE.

an interpolation function (Fig. 5.5) based on the drift velocity measurement in [37].

The dominant ion clusters in the plasma are H_5^+ or larger. Since experimental data on the effective mobility of hydrogen ion clusters contain some uncertainty, validation simulations tested various mobility values. On the other hand, measured values for the mobility of dopant oxygen ions, formed by the electron attachment, are relatively accurate. Simulations used measurement values reported in [38, 28, 39].

Another factor contributing to the plasma loading simulations is the distribution of the RF field (E_0) in the cavity. The amplitude of the RF field (E_0) fed to the HPRF cavity is not constant. The amplitude distribution is studied [28, 34]. Figure 5.9 shows the distribution. Since the

Ion	Reduced Mobility ($\frac{cm^2}{V\,s}$)
H_3^+	11.2
H_5^+	9.6
O_2^-	11.4

Figure 5.6: Ion mobilities from [28]

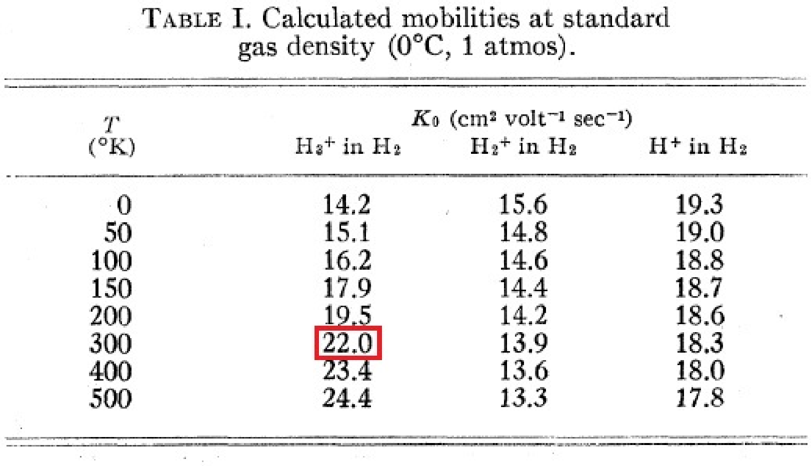

TABLE I. Calculated mobilities at standard gas density (0°C, 1 atmos).

T (°K)	K_0 (cm² volt⁻¹ sec⁻¹)		
	H_3^+ in H_2	H_2^+ in H_2	H^+ in H_2
0	14.2	15.6	19.3
50	15.1	14.8	19.0
100	16.2	14.6	18.8
150	17.9	14.4	18.7
200	19.5	14.2	18.6
300	22.0	13.9	18.3
400	23.4	13.6	18.0
500	24.4	13.3	17.8

Figure 5.7: Hydrogen ion mobilities in hydrogen gas from [39]

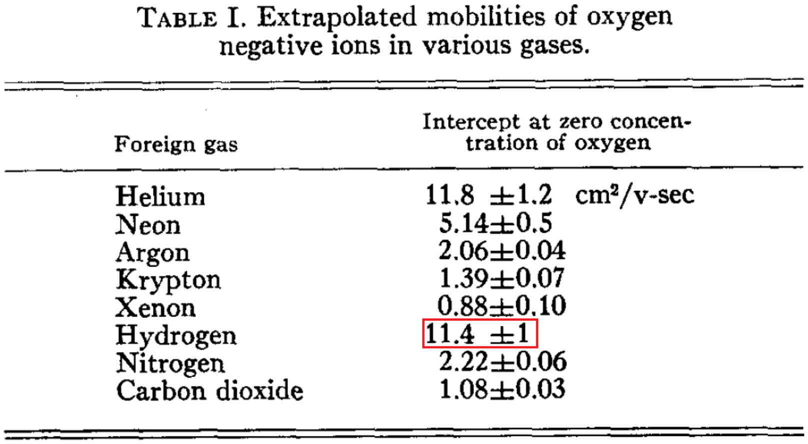

TABLE I. Extrapolated mobilities of oxygen negative ions in various gases.

Foreign gas	Intercept at zero concentration of oxygen
Helium	11.8 ±1.2 cm²/v-sec
Neon	5.14±0.5
Argon	2.06±0.04
Krypton	1.39±0.07
Xenon	0.88±0.10
Hydrogen	11.4 ±1
Nitrogen	2.22±0.06
Carbon dioxide	1.08±0.03

Figure 5.8: Oxygen ion mobilities in various gas from [38]

beam radius used in the experiments and the simulations is $2mm$, we have constant E_r. On the other hand, E_z has large variation around the center, simulations of SPACE reflect the variation by the normalized E_z ratio $f(z) = 0.00448361291z^2 - 0.3631830091z + 8.24927707$. Figure 5.10 shows the normalized E_z estimation in [28, 34] and the E_z used in SPACE. The differences between the $f(z)$ and the two distributions when $r = 0.0mm$ and $r = 2.29058mm$ in [28, 34] are less than 2%.

The changing external RF field due to plasma loading can be approximated by an LRC resonant circuit formula [40]. In particular, the RF power dissipation can be described as

$$P = \frac{V(t)[V_{\max} - V(t)]}{R} - CV(t)\frac{dV(t)}{dt}, \tag{5.6}$$

where P, R, C, $V_{\max}$, $V(t)$ are the RF field power, the shunt impedance, the cavity capacitance, the magnitude of the external RF voltage, and the

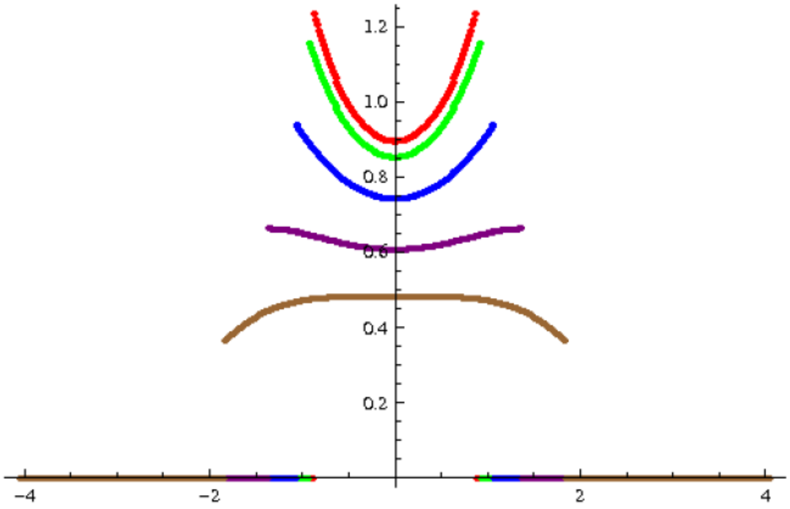

(a) E_z, normalized by 1

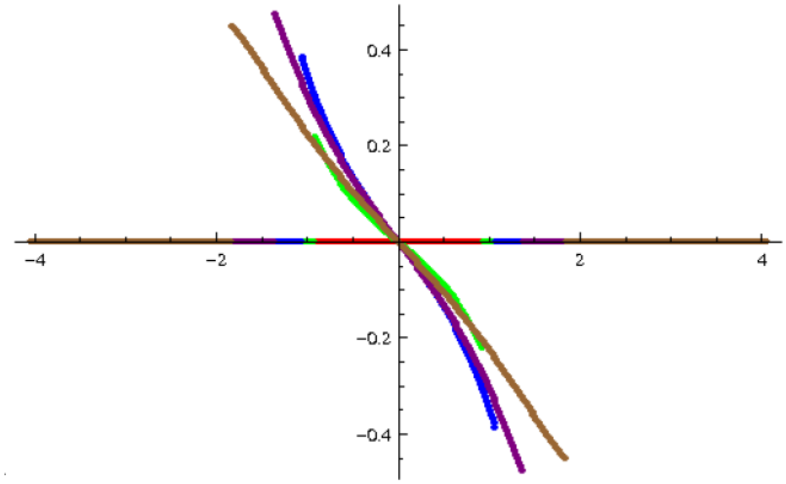

(b) E_r

Figure 5.9: Electric field as a function of z inside the HPRF cavity. The colors correspond to different radii: Red = 0.0 cm, Green = 0.5 cm, Blue = 1.0 cm, Purple = 1.5 cm and Brown = 2.0 cm. At r = 0mm the gap spacing is 1.77 cm.[28]

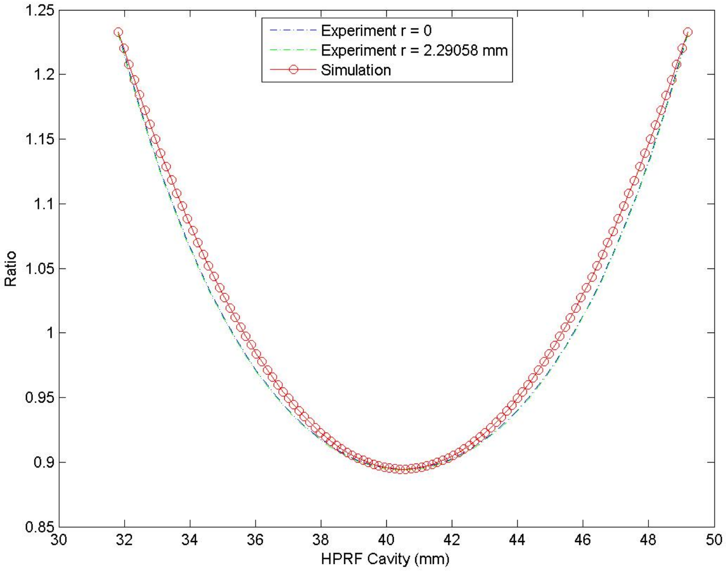

Figure 5.10: The normalized E_z distribution at radius $r = 0.0mm$, $r = 2.29058mm$, and in SPACE code.

instantaneous voltage value, respectively [27, 40]. In the simulations, the total power of plasma loading is computed at each time steps, and this value is used to compute the RF field voltage $V(t)$ and compare it with experimentally measured values.

5.2.3 Recombination

In the RF cavity, filled initially with pure hydrogen gas, ionization electrons recombine with hydrogen clusters through either binary or ternary recombination processes:

$$e^- + {H_j}^+ \rightarrow neutrals,$$
$$e^- + {H_j}^+ + H_2 \rightarrow neutrals + H_2 \tag{5.7}$$

where $j = 3, 5, 7, \cdots$. At the HPRF conditions, ternary recombination is dominant [27]. The time evolution of the electron number density is given by the following equation

$$\frac{dn_e}{dt} = \dot{N}_e - \sum_j \beta_j n_e n_{{H_j}^+} \tag{5.8}$$

where $j = 3, 5, 7, \cdots$, and n_e, $\dot{N}_e$, and β_j denote the number density of electrons, the production rate of electrons, and the recombination rate of electrons and ${H_j}^+$, respectively. As individual recombination rates are unknown, an effective recombination rate β_e for an averaged hydrogen ion cluster is used. The effective recombination rate was measured in the MTA experiments at the equilibrium state of plasma (i.e. $dn_e/dt = 0$). In our model, we use the following fit for the effective recombination rate, applicable to transient processes in the plasma

$$\beta_e = aX^b, \tag{5.9}$$

where $X = E/P$ is the ratio of electric field intensity to the gas pressure. As described in Section 5.3, values for the parameters a and b are obtained via comparison of HPRF simulations and various experimentally measures quantities, in particular, the plasma loading.

5.2.4 Attachment and Ion - Ion Recombination

When an electronegative gas such as oxygen is added to the hydrogen gas, a three-body attachment process takes place in the plasma, which is significantly faster than the electron - ion recombination [28]. The negative ions produced by the attachment process recombine with hydrogen ions. The governing equations are

$$\begin{aligned} \frac{dn_e}{dt} &= \dot{N}_e - \beta_e n_e n_{H^+} - \frac{n_e}{\tau} \\ \frac{dn_{H^+}}{dt} &= \dot{N}_e - \beta_e n_e n_{H^+} - \eta n_{H^+} n_{O_2^-} \\ \frac{dn_{O_2^-}}{dt} &= \frac{n_e}{\tau} - \eta n_{H^+} n_{O_2^-} \end{aligned} \tag{5.10}$$

where τ, η, and $n_{O_2^-}$ are the attachment time, effective ion - ion recombination rate, and the number density of dopant gas ions, respectively. The averaged hydrogen ion cluster that represents the sum $\sum_j n_{H_j{}^+}$ is denoted as n_{H^+}.

The attachment time and the ion - ion recombination rate have been measured experimentally, but only over a narrow range of RF field intensities. Based on measured values, simulations establish accurate fit functions for the attachment time and the ion - ion recombination rate.

5.3 Simulation Results

5.3.1 Hydrogen Gas-Filled RF Cavity

In the RF cavity filled with pure hydrogen gas, ionization and electron - ion recombination are the main processes in the plasma. The main physics

Parameters	Values
Kinetic Energy of beams	400 MeV
Beam Length	25 cm
Beam Radius	2 mm
H_2 gas pressure	100 / 20.4 atm
dE/dx	6.33 MeVcm^2/g
Average Ionization Energy	36.2 eV
External Electric Field	20.46 MV/m
(Frequency)	(801.6 MHz)
Population per Bunch	2.23×10^8
Bunch Spacing	5 ns
Total Number of Beam Bunches	2000 / 1500

Table 5.1: Parameters of HPRF cavity at 100 atm of pure hydrogen gas.

parameters are described in Table 5.1.

The computational domain setting is shown in Fig. 5.11. Proton beams of $2mm$ radius and $25cm$ length are injected into the computational domain with $5ns$ time spacing.

Using the effective recombination rate measured at the MTA [41], simulations established accurate fit functions for the recombination rate and particle mobilities that result in excellent agreement with experimentally measured quantities. In particular, the obtained fit for the recombination rate is $\beta = 1.5 \times 10^{-10}\ X^{-1.2}\ (cm^3/s)$ where X = E/P (MV/m/psi). Figures 5.12, 5.13, 5.14, and 5.15 show good agreement between simulations and experiment in terms of dw and the plasma loading of the HPRF cavity.

Figure 5.14 shows that the simulated magnitude of the electric field is in error bars. The error bars include 10% measurement errors and standard deviations of 8 experiments. After the beam is turned off at 10 μs, the external

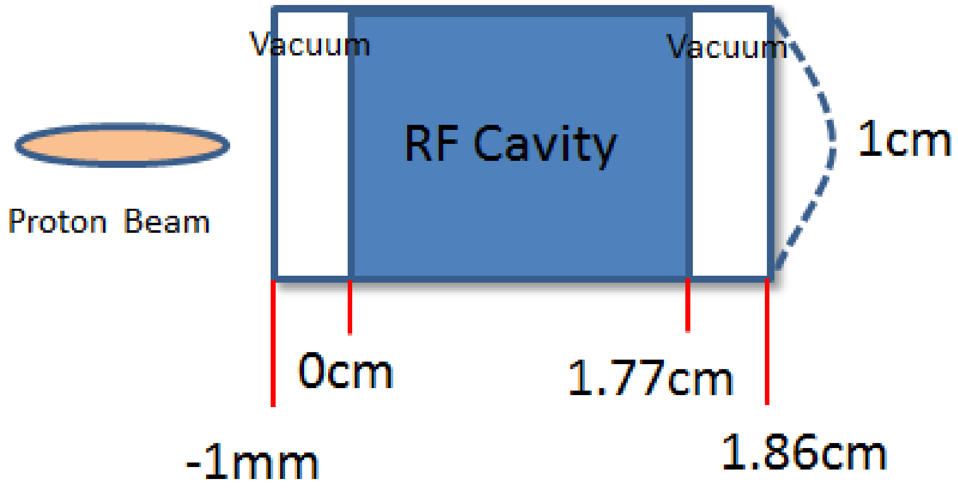

Figure 5.11: The schematic diagram of the computational domain of the HPRF simulations. Refer to Fig. 5.3 for the engineering drawing of the cavity.

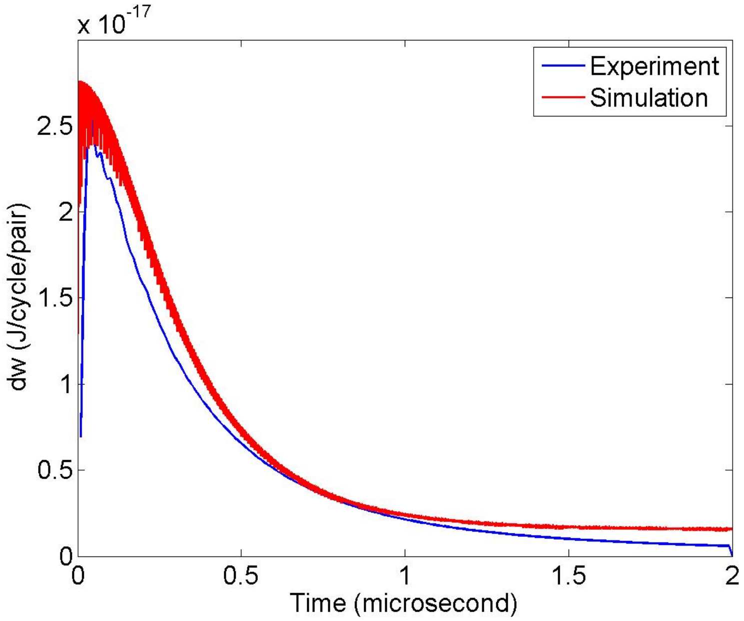

Figure 5.12: Comparison of simulated and experimental values of dw for HPRF cavity filled with pure hydrogen gas at 100 atm.

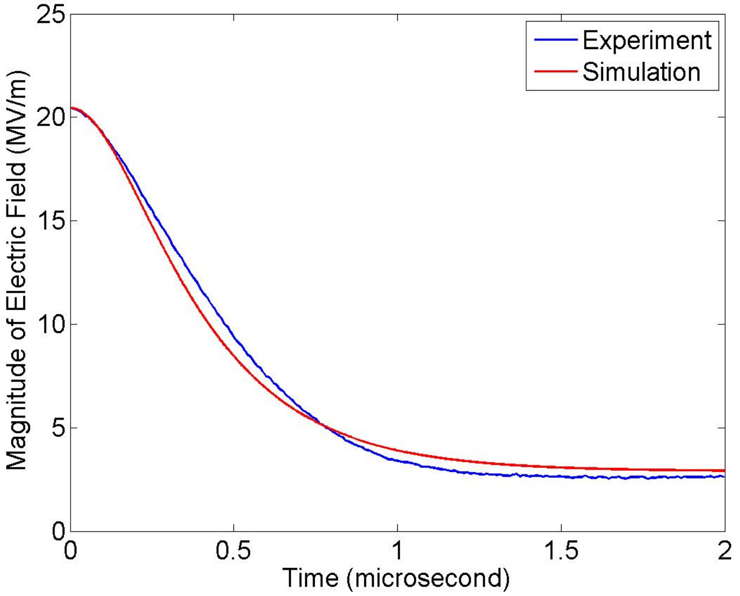

(a) 2 μs

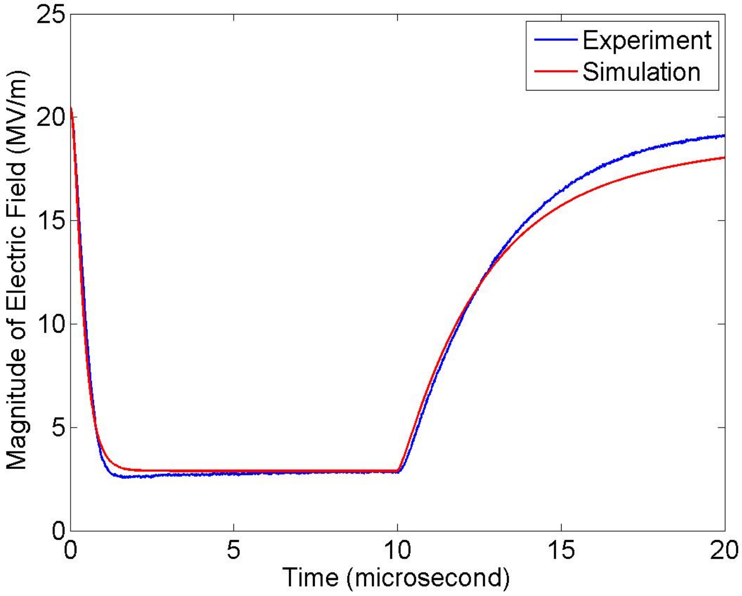

(b) 20 μs

Figure 5.13: Comparison of simulated and experimental values of the magnitude of the external electric field in HPRF cavity filled with pure hydrogen gas at 100 atm.

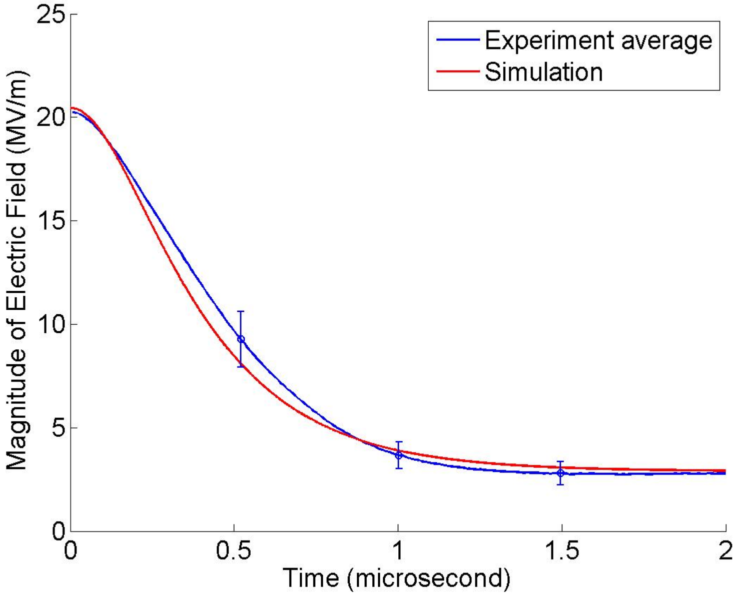

(a) 2 μs

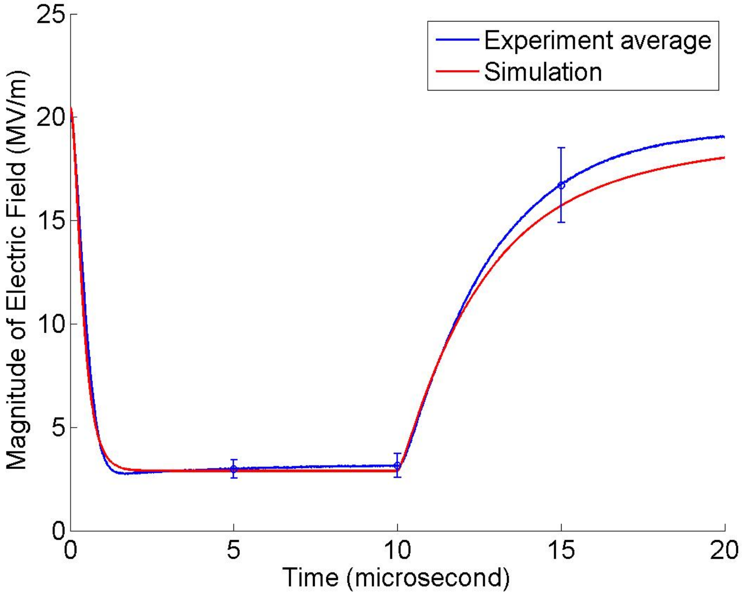

(b) 20 μs

Figure 5.14: Comparison of simulated values of the magnitude of the external electric field with experimental error estimates in HPRF cavity filled with pure hydrogen gas at 100 atm.

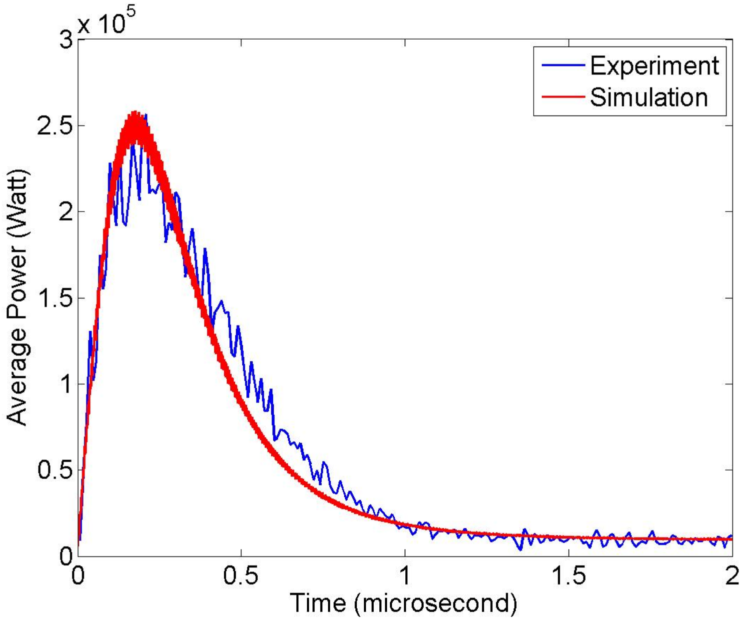

(a) 2 μs

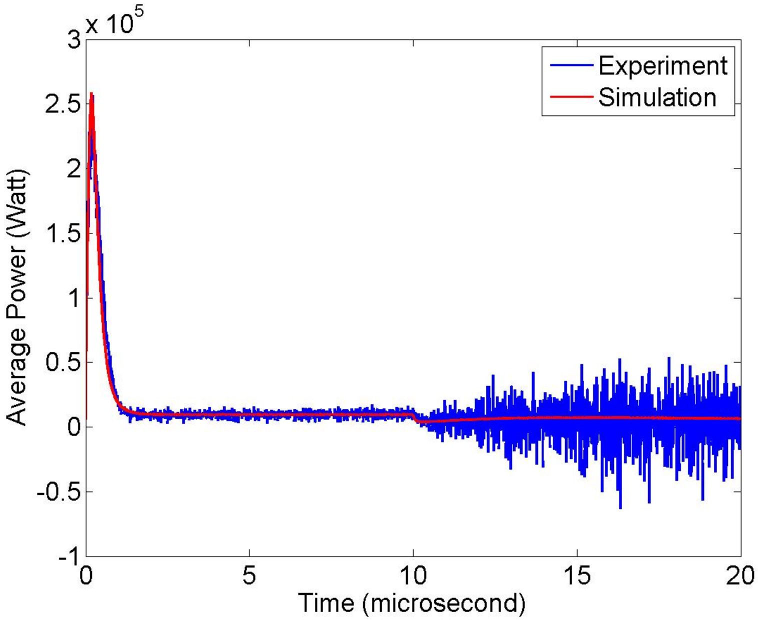

(b) 20 μs

Figure 5.15: Comparison of simulated and experimental values of power in the HPRF cavity filled with pure hydrogen gas at 100 atm.

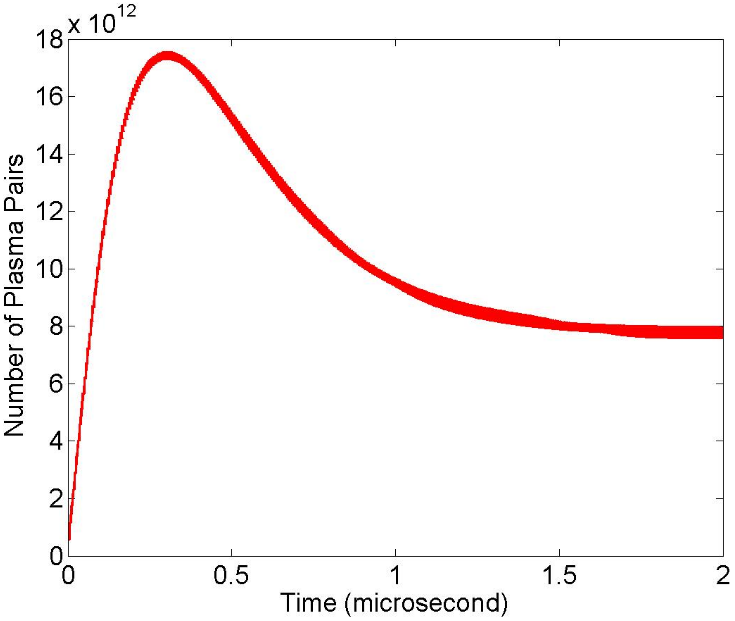

(a) 2 μs

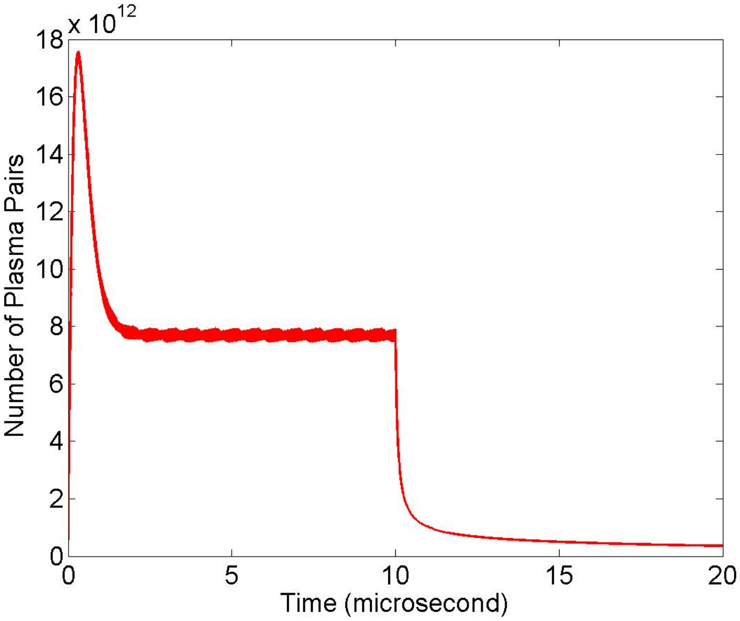

(b) 20 μs

Figure 5.16: Simulated values of number of electrons in the HPRF cavity filled with pure hydrogen gas at 100 atm.

electric field (Fig. 5.13b) recovers as the number of electrons (Fig. 5.16b) decrease via recombination.

The equilibrium state of the plasma, when ionization is balanced by recombination, is achieved between 2 μs and 10 μs (see Fig. 5.13, 5.15, and 5.16). The electron - ion recombination rate was experimentally measured only in this region [28] while the fit function, established in simulations, is applicable to the transient region as well. Figure 5.13 shows that the magnitude of the external RF field is reduced by the factor of 7 at the equilibrium. Such a large reduction is explained by a slow electron - ion recombination rate, resulting in a high density of plasma particles.

The thick (red) band shown in Fig. 5.12, 5.15, and 5.16 is caused by high frequency oscillation of the corresponding quantities in simulations. These oscillations are caused by the structure of the beam, in particular the recombination processes in 5 ns intervals between bunches. In Fig. 5.15, the measurement of power is noisy, especially after the beam off time (10 μs) shown in Fig. 5.15b.

Another simulation of 20.4 atm with 1500 bunches has been accomplished. Based on the effective recombination rate measured at the MTA [41], the recombination rate $\beta = 1.5 \times 10^{-10}\ X^{-1.0}$ (cm^3/s) is obtained where $X =$ E/P (MV/m/psi). Figures 5.17, and 5.18 show good agreement between simulations and experiment. The fit $\beta = 1.5 \times 10^{-10}\ X^{-1.0}$ is used for dopant added case in the following section.

The amplitude of the external electric field falls to 0.16 MV/m. After the beam is turned off at 7.5 μs, the external electric field (Fig. 5.17) recovers as the number of electrons (Fig. 5.19) decrease via the recombination.

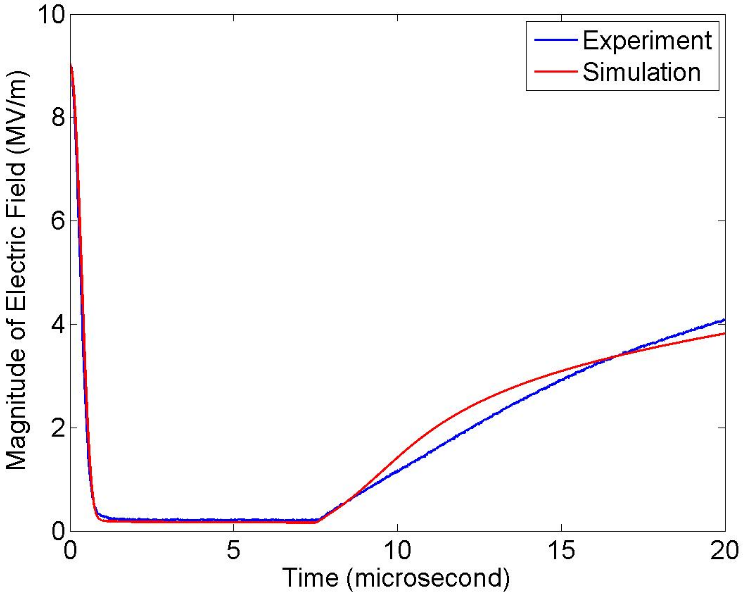

Figure 5.17: Comparison of simulated and experimental values of the magnitude of the external electric field in HPRF cavity filled with pure hydrogen gas at 20.4 atm.

5.3.2 Hydrogen Gas with Dry Air Dopant

When an electronegative gas dopant is added to the hydrogen gas in the HPRF cavity, the electron attachment to dopant molecules and ion - ion recombination take place in addition to the electron - ion recombination process. The main parameters are described in Table 5.2.

The attachment time and the ion - ion recombination were measured in the MTA experiment, albeit in a narrow range. Similar to the pure hydrogen gas case, simulations achieved good agreement with experimentally measured quantities characterizing the plasma loading by finding the best fit functions.

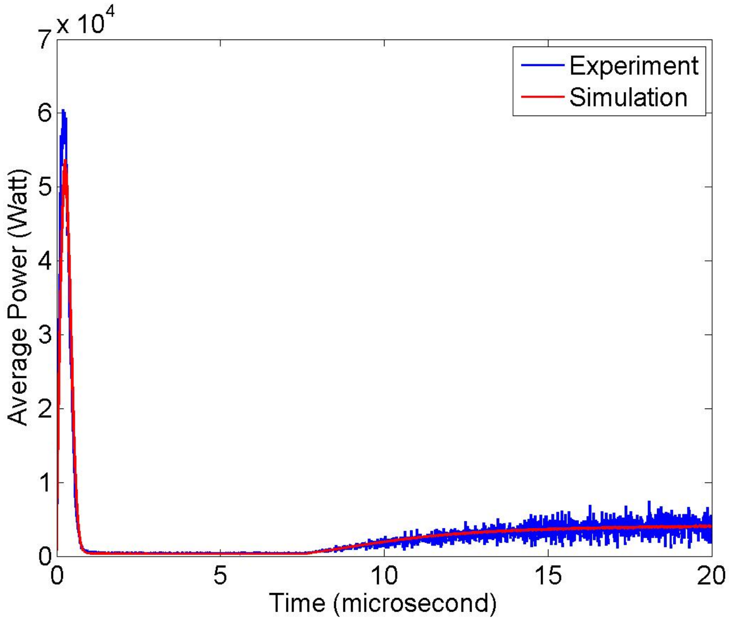

Figure 5.18: Comparison of simulated and experimental values of power in the HPRF cavity filled with pure hydrogen gas at 20.4 atm.

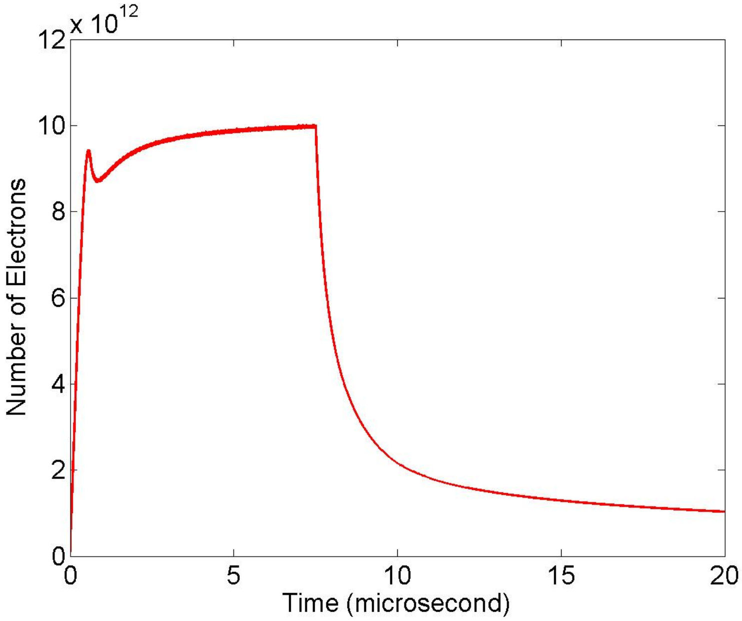

Figure 5.19: Simulated values of number of electrons in the HPRF cavity filled with pure hydrogen gas at 20.4 atm.

Parameters	Values
H_2 gas pressure (Dopant)	20.4 atm (1% dry air)
External Electric Field	8.84 MV/m
(Frequency)	(808.4 MHz)
Population per Bunch	1.61×10^8

Table 5.2: Parameters of HPRF cavity at 20.4 atm of hydrogen gas with 1 % dry air. Only quantities with different values compared to Table 5.1 are shown.

In particular, $\tau = 4.0 \times 10^{-7}\ X^{1.0}\ (s)$ and $\eta = 1.6 \times 10^{-10}\ X^{-1.0}$, where $X =$ E/P (MV/m/psi), were used.

Plasma electrons become attached to dopant molecules in a short period of time. Fig. 5.23, 5.21, and 5.22 shows that the densities of hydrogen ions and dopant ions exceed the electron density by a factor of 50 even at 1 μs, and this ratio increases with time. We would like to note that quantities shown in Fig. 5.23, 5.21, and 5.22 fluctuate with the beam period of 5 ns. To eliminate this effect, all quantities are shown at the same phase of the proton beam, in particular when the proton bunch is in the center of the cavity.

In general, the effect of plasma loading of the HPRF cavity is governed by three processes: the electron attachment to dopant, the electron - ion recombination, and the ion-ion recombination. During the injection of the proton beam, the first process is dominant at early times, defining the initial slope of the external RF field magnitude in Fig. 5.24a. Both the attachment and ion-ion recombination are important after $0.5\mu s$, and the ion-ion recombination plays a much bigger role compared to the electron - ion recombination. After the beam is turned off (see Fig. 5.20), the electron density rapidly de-

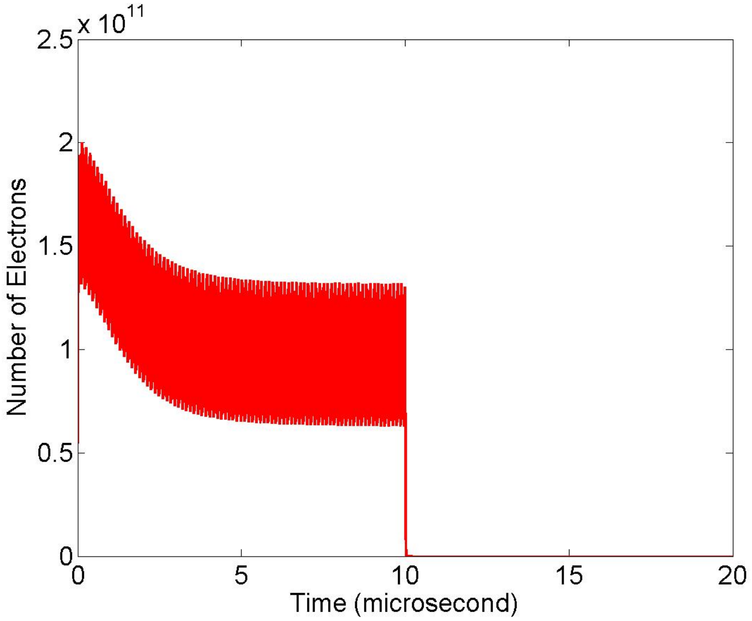

Figure 5.20: Total number of electrons in the cavity along time in the HPRF cavity filled with 20.4 atm hydrogen gas and 1% dry air dopant.

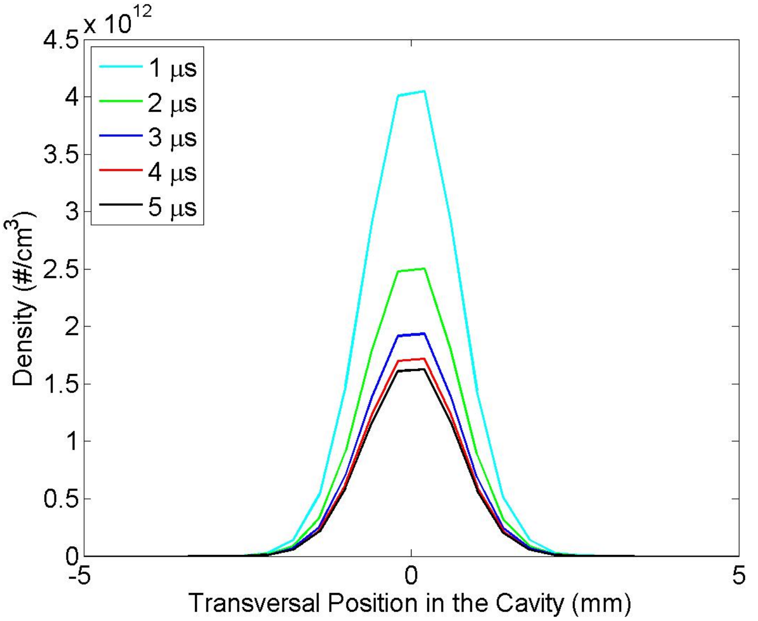

Figure 5.21: Charge distribution of electrons at the center of the HPRF cavity filled with 20.4 atm hydrogen gas and 1% dry air dopant.

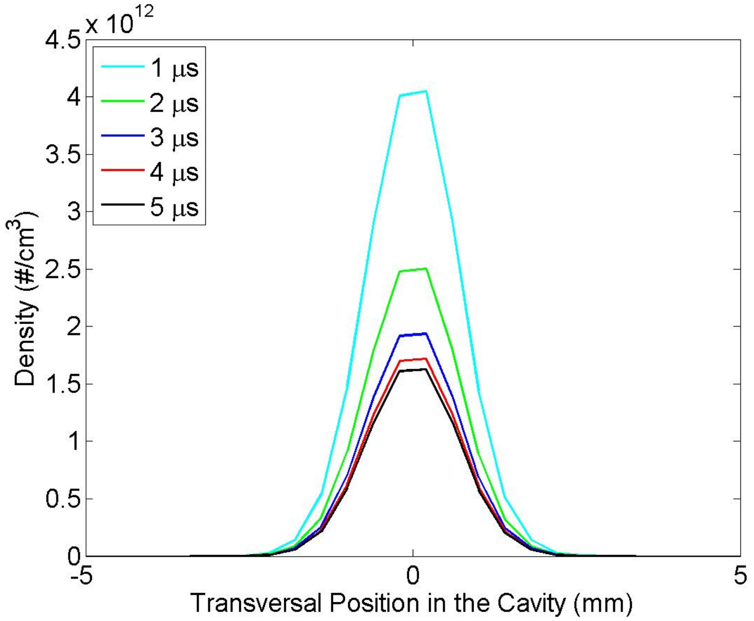

Figure 5.22: Charge distribution of hydrogen ions at the center of the HPRF cavity filled with 20.4 atm hydrogen gas and 1% dry air dopant.

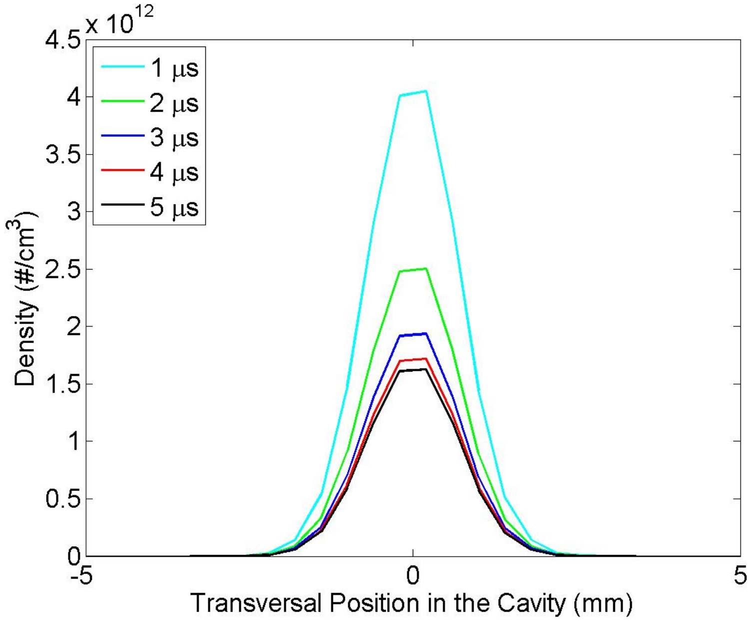

Figure 5.23: Charge distribution of dopant (oxygen) ions at the center of the HPRF cavity filled with 20.4 atm hydrogen gas and 1% dry air dopant.

creases through attachment, and only the ion-ion recombination is effectively responsible for the recovery of the external RF field magnitude. Fluctuations of experimental values of the power in Fig. 5.24b are explained by measurement errors of the RF signal. There is noise in the RF signal record and it makes power record in Fig. 5.24b worse by $\frac{dV(t)}{dt}$ term in Eq. (5.6). But the simulation result of the power shows similar tendency with the experiment in Fig. 5.24b. Fig. 5.24a shows that the external electric field magnitude is reduced only by a factor of 1.7 at the equilibrium. This is a great improvement compared to the pure hydrogen case: simulations with pure hydrogen at the same conditions (20.4 atm) show that the RF field magnitude at equilibrium is reduced by a factor of 44.

5.4 Conclusion

Models and algorithms for plasma dynamics in the HPRF cavity have been developed and implemented in the code SPACE. Numerical studies of the HPRF cavity have been performed, compared with experiments in the Fermilab MTA facility, and a very good agreement has been obtained. Dominant effects of the plasma dynamics in the HPRF cavity have been quantified in numerical simulations and previous analytical studies. They showed that ionized electrons are immediately thermalized by interacting with neutral particles and follow the conventional electron transport model. As reported in the experimental paper [27], electrons mobility is significantly reduced by the pressure effect. Electron capture by electronegative dopant is also explained by the conventional three body model. It concludes that the electron cap-

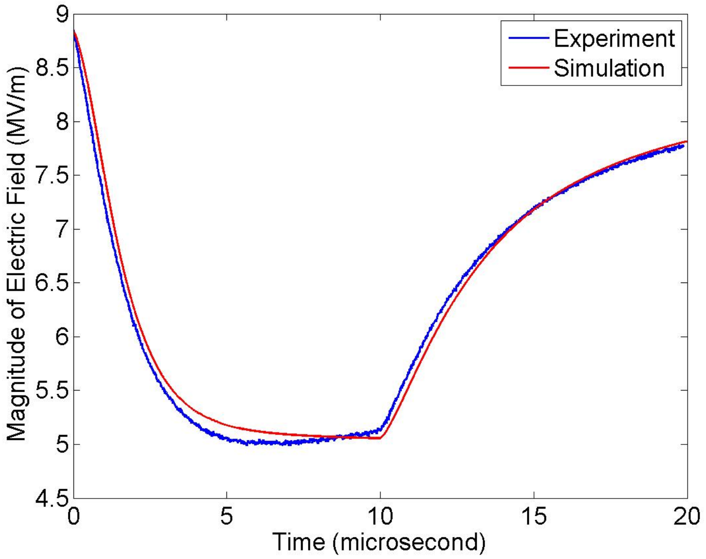

(a) Amplitude of the external electric field at the center of the cavity.

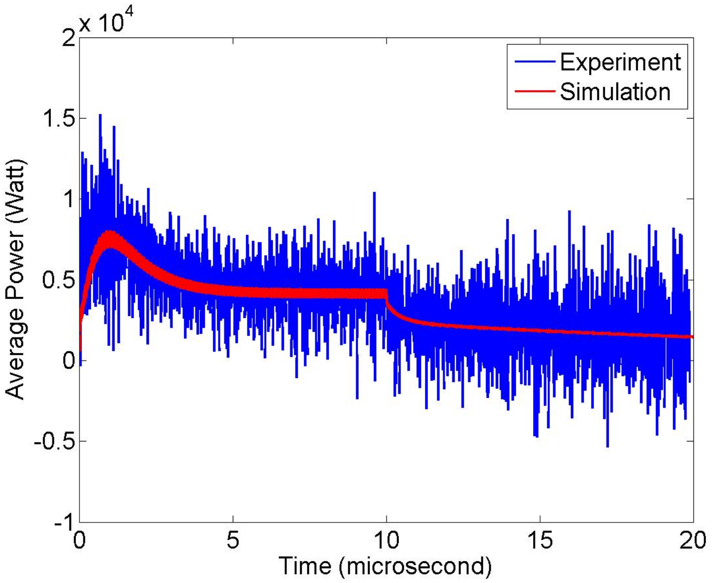

(b) Power dissipated by plasma loading

Figure 5.24: Comparison of simulations and experiments for HPRF cavity filled with 20.4 atm hydrogen gas with 1% dry air dopant.

ture time can be much shorter than nanosecond. As a result, plasma spatial distribution can now be determined accurately in SPACE.

On the other hand, simulations show a very strong reduction of the external RF field magnitude in equilibrium for pure hydrogen plasma: the field is reduced by the factor of 7 at the pressure of 100 atm, and by the factor of 44 at 20.4 atm. The larger reduction of the electric field at low pressure is due to smaller recombination rates, and therefore, a higher electron density. If a 1 % dry air dopant is added to the hydrogen gas, the reduction of the RF field is greatly mitigated: the reduction factor at 20.4 atm is only 1.7. Simulations have achieved very good agreement with experiments on plasma loading and related processes.

Simulations also contributed to a better understanding of plasma properties. In a series of simulations and their comparison with experimentally measured quantities characterizing the plasma loading process, several uncertain properties of the plasma, such as effective recombination rates and the attachment time of electrons to dopant molecules have been quantified and accurate fit functions for these quantities, which is valid over a wide parameter range, have been found. We could not find such a non-linear process in analytic investigation.

In the next step, SPACE will be used for prediction of the plasma loading in the practical ionization cooling channel and investigation of the beam-plasma interaction with intense muon beam.

Chapter 6

Application II: Simulation for Advanced Coherent Electron Cooling

Cooling intense high-energy hadron beams remains a major challenge in modern accelerator physics. Free Electron Laser (FEL) based coherent electron cooling is a promising technique offering potential to cool high-energy hadron beams [42]. Figure 6.1 illustrate the general schematic layout of the coherent electron cooling, which comprises three sections: a modulator, an amplifier, and a kicker. Principles of coherent electron cooling are introduced in [42, 43]. In modulator, electrons are modulated due to the attraction of hadrons. In amplifier, the modulation of charge density in electron beam is amplified using the Free Electron Laser (FEL) in classic coherent electron cooling. In advanced coherent electron cooling, FEL is replaced by wiggler. A three pole wiggler is used in the numerical simulations. In the kicker, the hadron beam is cooled by the amplified electron beam. The modulator and the wiggler are studied by the numerical simulations.

This application study is mainly accomplished by Jun Ma [20] and all

Parameters	Values
Beam velocity	$\gamma = 42.9$
Peak current	100 A
Full bunch length	10 ps
Bunch charge	10 nC
R.M.S. emittance	5 π mm mrad
R.M.S. energy spread	1e-3
Beta function at modulator and kicker	4 m

Table 6.1: Electron Beam Parameters

graphs in this chapter are results of his work.

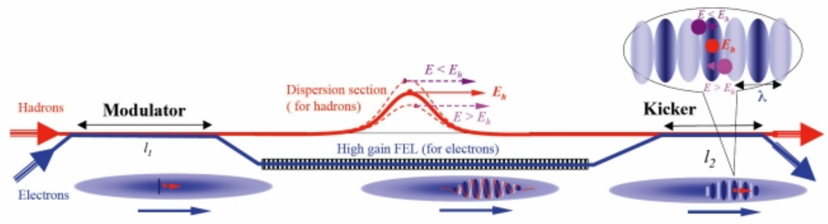

Figure 6.1: General schematic of the Coherent Electron Cooling [44].

6.1 Modulator

Table 6.1 and Table 6.2 give the physical parameters of electron beam and ion beam. We compute some secondary parameters from these two tables, such as number density and plasma oscillation frequency, in order to design the setup of our numerical simulations.

In order to add the effect of thermal velocity on electron, The kappa-2 velocity distribution is used to model the random motion of electron beam [45]. Equation (6.1) [45] gives the 3D density function of kappa-2 velocity

Parameters	Values
Beam velocity	$\gamma = 42.9$
Species	Au^{+79}
Bunch intensity	1e+9
R.M.S. bunch length	2 ns
R.M.S. emittance	2 π mm mrad

Table 6.2: Ion Beam Parameters

distribution where β_x, β_y and β_z are the parameters describing the electron beam's three-dimensional temperatures respectively and $\vec{v}_0$ denotes the ion velocity.

$$f_0(\vec{v}) = \frac{n_0}{\pi^2 \beta_x \beta_y \beta_z} \left(1 + \frac{(v_x + v_{0x})^2}{\beta_x^2} + \frac{(v_y + v_{0y})^2}{\beta_y^2} + \frac{(v_z + v_{0z})^2}{\beta_z^2}\right)^{-2} \tag{6.1}$$

In simulations, only one ion is used instead of using the whole ion beam because this is sufficient to resolve the modulation of electron beam by ion. The moving frame of $\gamma = 42.9$ is used with kappa-2 velocity distribution of $\beta_x = \beta_y = 2e+6m/s$ and $\beta_z = 3e+5m/s$. The computational domain size is determined by the Debye length based on the velocity distribution. The ion is located in the center of the computational domain. In such a small domain, we could assume uniform distribution of electron beam, and periodic boundary condition is used. According to physical setup, the modulator length is 3 m, which will be the co-propagation distance of ions and electrons.

In modulator simulation, we measure the density distribution of electrons to observe the electrons beam dynamics due to the ion. Strong shot noise makes it difficult to obtain meaningful redistribution of electrons. There are two sources of the shot noise. One is the randomness in initial distribution. We have a huge number of electrons in computational domain, and we use random function to generate the initial distribution of those electrons. The random distribution generates shot noise, which is shown in Figure 6.2. And the physical redistribution of density is orders smaller than the shot noise. Another reason of shot noise is the random motion of electrons. In previous section, we introduce the kappa-2 velocity distribution which models the electron temperature. These random motions also contribute to the shot noise.

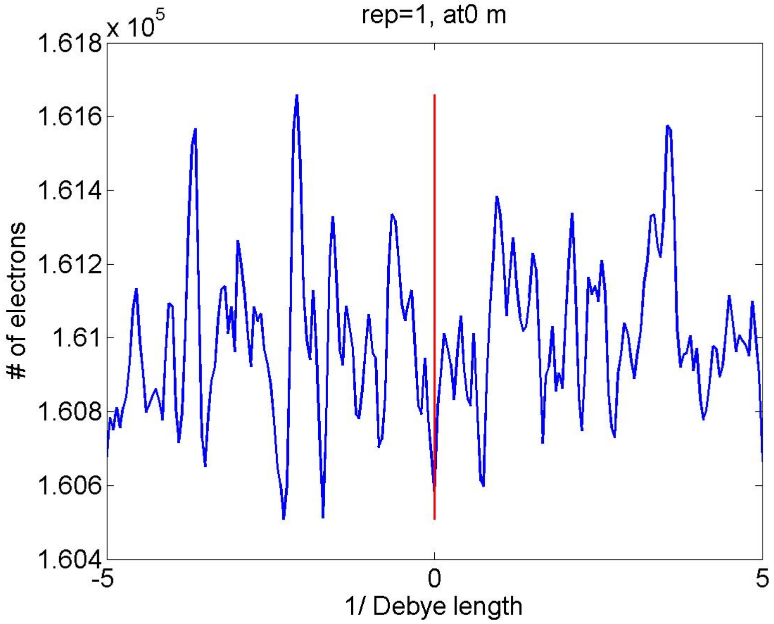

Figure 6.2: Initial distribution of electrons in modulator.

In order to reduce the shot noise, comparison is used. In one run, only electron beam is used. On the other hand, the same electron beam with the former having the ion is simulated. After that, the difference of these two run is recorded. This method eliminates all shot noise caused by randomness of electron particle position and of the electron thermal velocity. Figure 6.3 shows the high density in the center of the ion location.

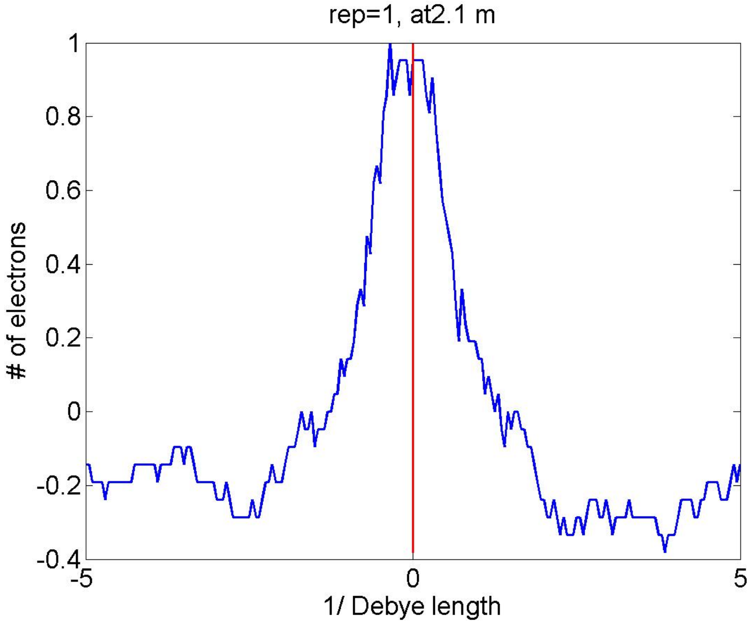

Figure 6.3: Redistribution of electrons using eliminating of background shot noise

Because of the flexibility of using representing number in SPACE, various representing number of ions are test. The redistributions of electrons are shown in Fig. 6.4. We observe that the amount of electrons attracted by ions is linearly proportional to the representing number of ion when we use ion representing number 1, 10, 100, but not so linear when it comes to 1000. This gives us a guidance that, as long as we are in the linear regime, we can use ion representing number larger than 1. And dividing the resulting distribution of electrons by that representing number gives the correct redistribution of using one real ion.

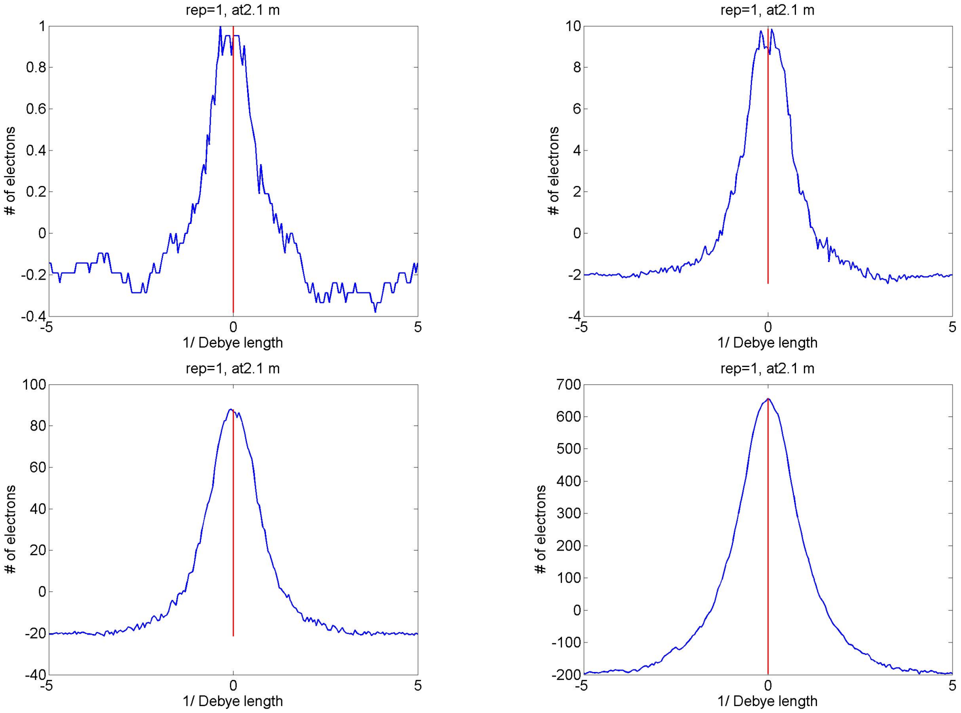

Figure 6.4: Redistribution of electrons with ion representing number equal to 1 (upper left), 10 (upper right), 100 (lower left), 1000 (lower right)

For validation of the modulator simulation, different numerical settings are tested. Figure 6.5, we use electron cloud around a macro ion with 1000 representing number, and plot the electrons number redistribution at the co-propagation distance of 2.1m. In Figure 6.6, the same electron and ion are used as Fig. 6.5, but mesh is coarser. In Figure 6.7, the same mesh as Fig. 6.6 which is coarser than Fig. 6.5, and 100 times more representing number (100 times less macroparticle number) in the preserved total charge.

From the comparison of Figure 6.5 and Figure 6.6, the electrons redistribution is independent on the mesh size. Figure 6.7 shows inaccuracy because of worse statics, as we use coarser mesh and less macro particles, but it still shows consistent redistribution. These validation simulations show that the modulator simulations depend on only physical values and the numerical values affects on the accuracy.

In addition to the former validation, the results of the modulator simulations are compared with the analytical computations of density modulation [46] and velocity modulation [47]. Figure 6.8 and 6.9 show that the modulator simulations are consistent with the analytical computations.

6.2 Wiggler

The amplifier is the second part of the advanced coherent electron cooler, in which the modulated electron beam will be amplified via passing through a series of magnetic pole. Advanced electron electron cooling use wiggler as the amplifier instead of free electron laser. The mechanism of wiggler is that the passing time of electrons of difference velocity is different. When a

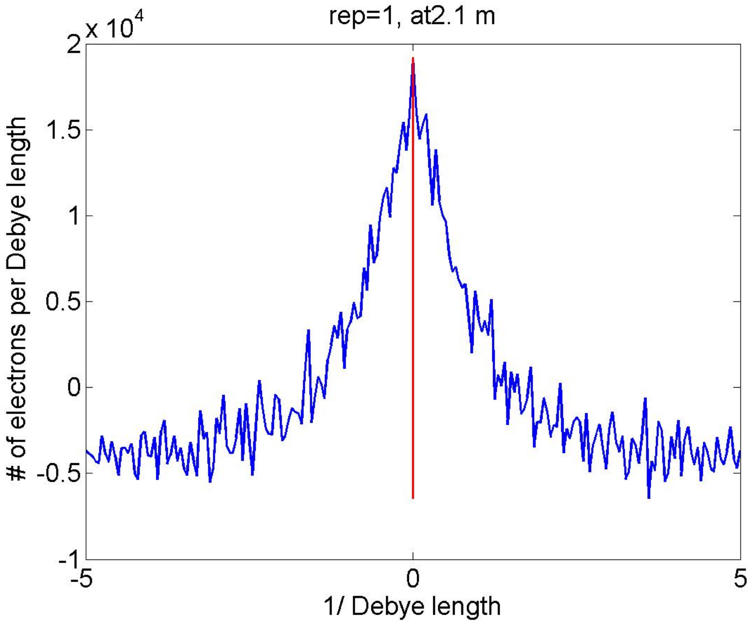

Figure 6.5: Electrons number redistribution with the 1000 representing number of ion

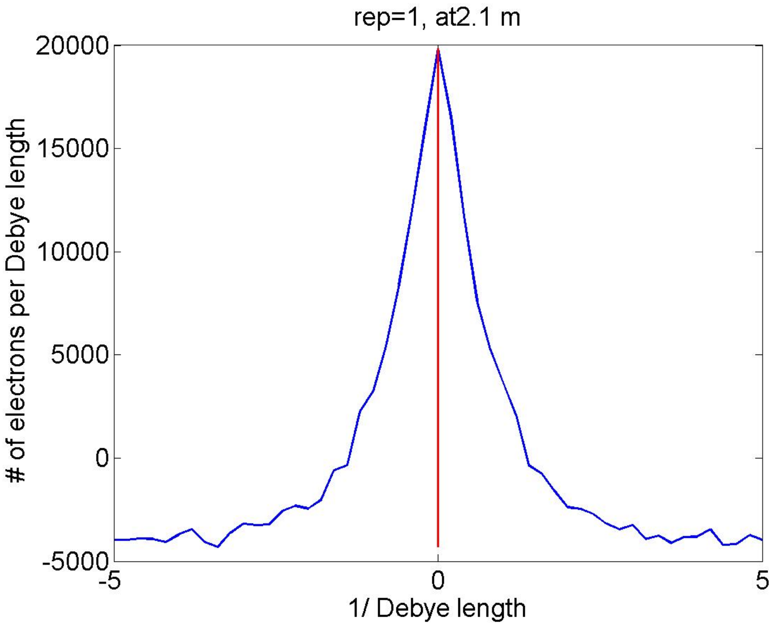

Figure 6.6: Electrons number redistribution with the 1000 representing number of ion and coarser mesh

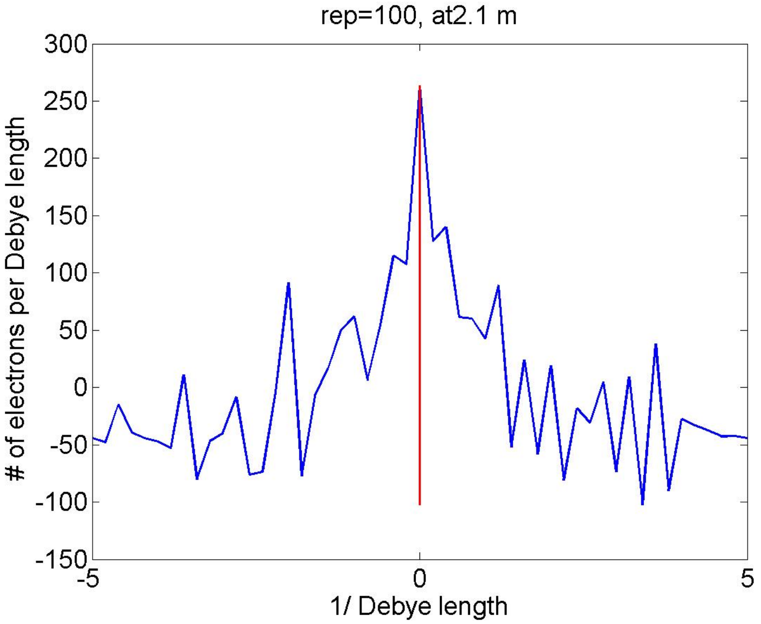

Figure 6.7: Electrons number redistribution with the 1000 representing number of ion, coarser mesh, and larger representing number or electron (smaller number of macro particles)

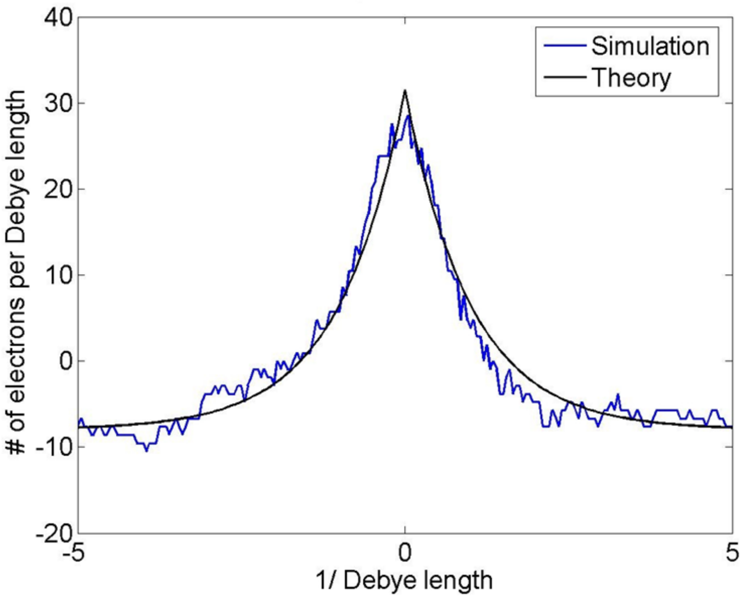

Figure 6.8: The density modulation comparison

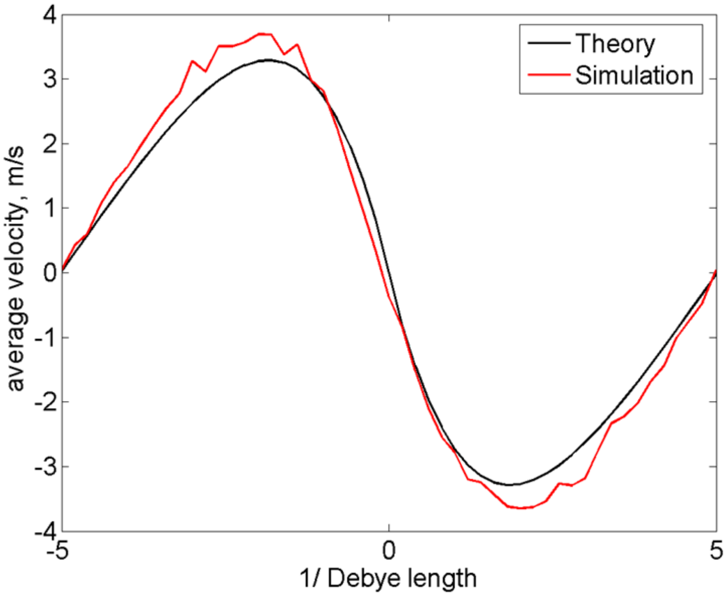

Figure 6.9: The velocity modulation comparison.

beam passes through the magnetic poles, the gyro-radius of the electrons are different according to their velocities. The tail part with larger velocities has larger gyro-radius, so they will bend less during the wiggler, and the passing time is less. A wiggler affects the head part of the electron beam in the opposite way: head part with smaller velocities has smaller gyro-radius, which bends them more during the wiggler, and the passing time is more. Therefore a wiggler slows down the faster electrons and speeds up the slower electrons. Hence the tail part moves forward and the head part moves backward, which makes the electron beam more compressed. Although the electron beam is already modulated by the ion, they can not get much closer because of the space charge effect. The strong magnetic field of wiggler is able to focus the electron beam much further.

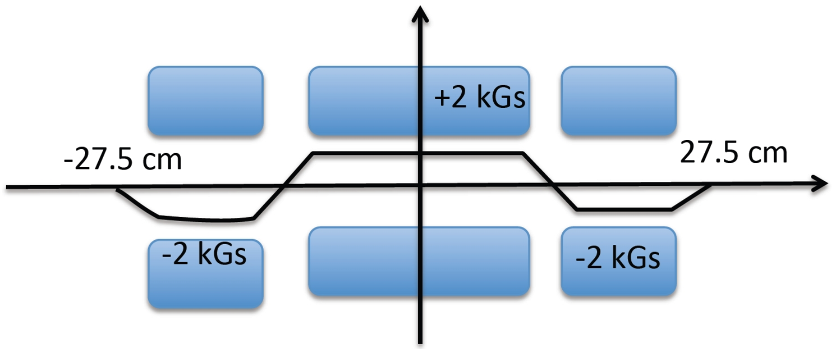

Figure 6.10: A three pole wiggler.

We use a three pole wiggler in the simulation, which is shown in Figure 6.10. The magnetic field is in transversal direction with peak value 0.2 T. We assume linear increase and decrease in the gaps between poles. The three pole wiggler is implemented as an external magnetic field in SPACE. As we are using moving frame for wiggler simulation, we keep the computational domain and move the wiggler in opposite direction towards the electrons. The Lorentz transform equation for particle (Equation 6.3) and for field (Equation 6.3) are used to obtain field values in moving frame (*) from lab frame.

$$\begin{aligned} z^* &= \gamma(z - ut) \\ t^* &= \gamma(t - \frac{uz}{c^2}) \\ v_x^* &= \frac{v_x}{\gamma(1 - \frac{uv_z}{c^2})} \\ v_y^* &= \frac{v_y}{\gamma(1 - \frac{uv_z}{c^2})} \\ v_z^* &= \frac{v_z - u}{1 - \frac{uv_z}{c^2}} \end{aligned} \tag{6.2}$$

$$
\begin{aligned}
E_x^* &= \gamma E_x - \gamma\beta c B_y \\
E_y^* &= \gamma E_y + \gamma\beta c B_x \\
E_z^* &= E_z \\
B_x^* &= \gamma B_x + \frac{\gamma\beta}{c} E_y \\
B_y^* &= \gamma B_y - \frac{\gamma\beta}{c} E_x \\
B_z^* &= B_z
\end{aligned}
\tag{6.3}
$$

The result of modulation is used for the input date for the wiggler simulation. The preliminary simulation result is shown in Fig. 6.10. After the wiggler, the electron beam is compressed more.

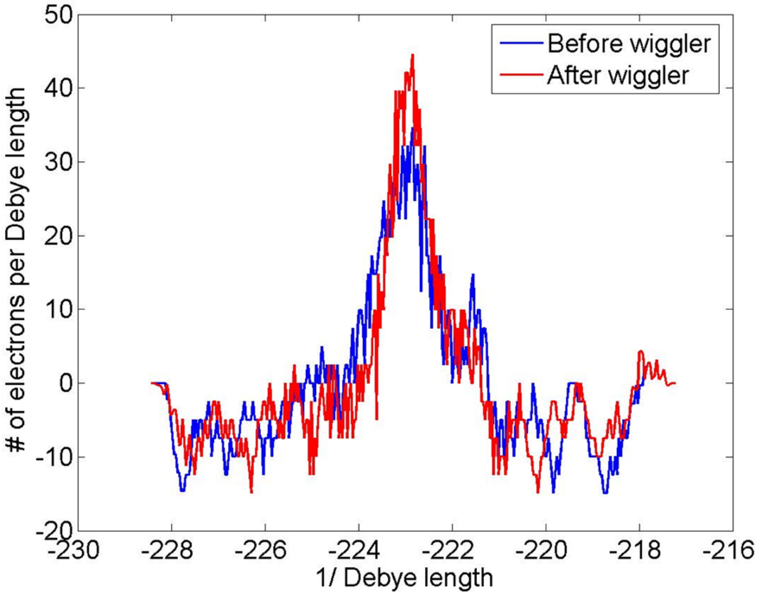

Figure 6.11: The density distribution comparison before and after the wiggler.

6.3 Conclusion and Future Work

In the modulator simulations of advanced coherent electron cooling, shot noise eliminating techniques is developed and redistribution of electron beam due to the presence of ion is obtained. The modulator simulation shows the results are consistent with the theory based on uniform distribution of electron. Therefore the simulation will study various non-uniform electron distributions and ions of different velocities. The preliminary wiggler simulations shows more compression of the electron beam. Strong compression effect of three pole wiggler is demonstrated. After the validation of the code for the wiggler, the amplification effect by the wiggler will be studied by the code with various results from the modulator. The results of the wiggler study will be used to study the kicker the last stage of the advanced coherent electron cooling. Through the simulation study in the whole stage of the advanced coherent electron cooling, the performance of the cooling method will be estimated and the result will be used to design a new coherent electron cooler which will be essential to hadron collider.

Chapter 7

Code Parallelization Effort

This chapter describes the code parallelization effort for the high performance computing.

Nowadays, high performance computing technique has been being developed and most computers support parallel running capability (at least multi-core processors). But many famous scientific codes are not able to utilize the parallel environment or partially benefit from them.

The one main reason is that the famous code usually has been developing for several decades and it is not considered to utilized the parallel computing capability at the initial time of the code development. Also, taking advantage from parallel computing such as Message Passing Interface (MPI) method or Graphic Processing Unit (GPU), usually involve significant code structure change or re-design of the code. In addition, the structure is usually strongly coupled with the physics implementation because of the performance issues and others. Therefore, it is not easy task converting a code to use parallel computing capability.

In the following sections, successful code parallelization accomplished during my Ph.D study is described briefly.

7.1 MADX-SC

MADX-SC is the specialized code of MAD-X [48] developed at the BE/ABP Accelerator Beam Physics Group at CERN for space-charge (SC) evaluation. By applying OpenMP parallelization, we achieved speed-up of the code [49]. In the speed-up test, we used 100 turns and varied the number of particles. The hardware consisted of an Intel(R) Xeon(R) CPU E5-2670 @ 2.60GHz CPU with 128 GBytes of RAM. Two different compilers IFORT of Intel(R) and GFORTRAN of GNU are tested and compared.

According to Fig. 7.1 and 7.2, both compilers show linear speed-up when we apply OpenMP parallelization and speed up improves with the number of particles. This is due to good weak scaling as the parallelization is applied to loops over the number of particles [49].

7.2 Quantum ESPRESSO

Quantum ESPRESSO [50] is a software package for quantum chemistry method based on the Density Functional Theory, plane wave basis sets, and pseudo-potential. The code is composed of several modules and the main module, Plane-Wave Self-Consistent Field, is accelerated by GPU. I accelerated the PHonon module by GPU. According to Fig. 7.3, since the H_PISQ subroutine takes 80% of the module running time, the subroutine is converted to CUDA

EX09-Large	FORTRAN	CUDA	Speed-up
H_PSIQ	20.86 sec	7.71 sec	2.71
H_PSIQ	25.99 sec	14.79 sec	1.76

Table 7.1: Speed-up of Example09 by GPU in the PHonon package.

EX09-Large	FORTRAN	CUDA	Speed-up
H_PSIQ	5598.41 sec	2065.06 sec	2.71
H_PSIQ	1 hour 39 min	41 min 37 sec	2.41

Table 7.2: Speed-up of the extend Example09 by GPU in the PHonon package.

code.

The speed-up test is accomplished on Example09 which is the example offered by the package. Since the computational domain size is not large enough, the extend example of the Example09 is also tested. Table 7.1 and 7.2 show the speed up results respectively.

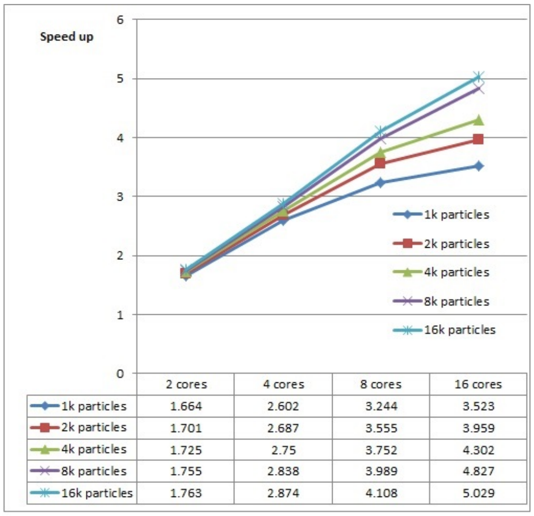

	2 cores	4 cores	8 cores	16 cores
1k particles	1.664	2.602	3.244	3.523
2k particles	1.701	2.687	3.555	3.959
4k particles	1.725	2.75	3.752	4.302
8k particles	1.755	2.838	3.989	4.827
16k particles	1.763	2.874	4.108	5.029

Figure 7.1: Speed-up comparison for the IFORT compiler case

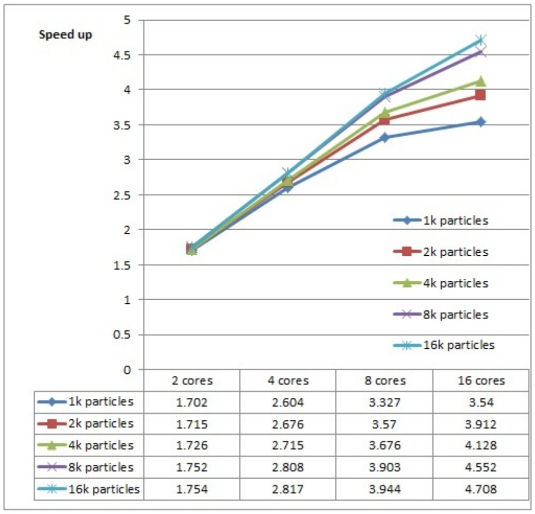

	2 cores	4 cores	8 cores	16 cores
1k particles	1.702	2.604	3.327	3.54
2k particles	1.715	2.676	3.57	3.912
4k particles	1.726	2.715	3.676	4.128
8k particles	1.752	2.808	3.903	4.552
16k particles	1.754	2.817	3.944	4.708

Figure 7.2: Speed-up comparison for the GFORTRAN compiler case

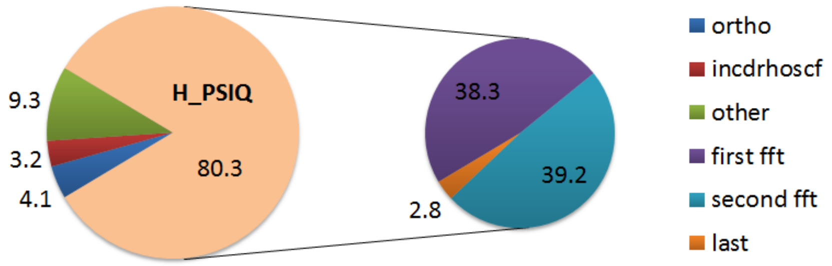

Figure 7.3: [Courtesy of Deyu Lu] PHonon module running time distribution. H_PSIQ subroutine takes about 80%.

Chapter 8

Conclusion and Future Work

A parallel, fully relativistic, and 3D electromagnetic and electrostatic Particle-in-Cell code, named SPACE, has been developed. The electromagnetic part of the code shows good weak-scalability. Based on the basic implementation of the PIC method, new atomic process algorithm dealing with beam-plasma interaction and plasma chemistry such as recombination is developed and implemented. The code has been verified by several benchmark simulations and has been being applied to actual simulation projects.

In the high pressure gas-filled RF cavity (HPRF) simulation study, the simulations show good agreement with the experiments accomplished in the MTA facility at Fermilab and the result validates the code. By a series of simulations and their comparison with experimentally measured quantities, simulations contributed to a better understanding of plasma properties and several uncertain properties of the plasma have been quantified and accurate fit functions for these quantities, which is valid over a wide parameter range, have been found. The code will be also able to be used for the prediction of the plasma loading in the ionization cooling channel and study of the beam-plasma interaction with intense muon beams.

In the simulation study for advanced coherent electron cooling (ACeC), the electrostatic part of SPACE is verified by the uniform electron distribution in the modulator. Various electron distributions are studied by simulations of SPACE. The benchmark for wiggler shows compression effect by magnetic poles and the result of modulator simulation of various distributions will be used for the wiggler simulation. The result of the wiggler study will be used to study the kicker and the performance of the whole cooling method of the ACeC will be estimated. This study will be also applied to the design of a new coherent electron cooler.

Parallelization of scientific codes is accomplished by OpenMP and GPU. The OpenMP parallelization for MADX-SC shows good speed-up. The effort of GPU acceleration for the Quantum ESPRESSO code continues for more speed-up. The experience from the code parallelization will be applied to the SPACE code for more speed-up. Especially, the GPU acceleration will be applied to SPACE.

Bibliography

[1] J. Ma, R. Samulyak, K. Yu, V. N. Litvinenko, G. Wang, Simulation of beam-induced plasma for the mitigation of beam-beam effects, in Proceedings of *IPAC 2015*, MOPMN015.

[2] K. Yu, R. Samulyak, A. Tollestrup, K. Yonehara, B. Freemire, M. Chung, Simulation of beam-induced plasma in gas filled cavities, in Proceedings of *IPAC 2015*, MOPMN013.

[3] R.W. Hockney, J.W. Eastwood, Computer simulation using particles, *CRC Press*, (1988).

[4] C.K. Birdsall and A.B. Langdon, Plasma Physics Via Computer Simulation, *New york: McGraw-Hill*, (1985).

[5] C. K. Birdsall, D. Fuss, Clouds-in-Clouds, Clouds-in-Cells Physics for Many-Body Plasma Simulation, *J. Comput. Phys.*, 135 (1997) 141-148.

[6] https://www.particleincell.com/2010/es-pic-method/

[7] X. Wang, R. Samulyak, X. Jiao, K. Yu, AP-Cloud: Adaptive Particle-in-Cloud method for optimal solutions to Vlasov-Poisson equation, *J. Comput. Phys.*, 316 (2016) 682-699

[8] J-L. Vay et al., Mesh refinement for particle-in-cell plasma simulations: applications to and benefits for heavy ion fusion, *Laser Part. Beams* 20 (04) (2002) 569-575.

[9] J-L. Vay et al., Application of adaptive mesh refinement to particle-in-cell simulations of plasmas and beams, *Phys. Plasmas* 11 (5) (2004) 2928-2934

[10] K. Yee, Numerical solution of initial boundary value problems involving maxwell's equations in isotropic media, *IEEE Transactions on Antennas and Propagation*, 14 (3) (1966) 302-307.

[11] J. Villasenor, O. Buneman, Rigorous charge conservation for local electromagnetic field solvers, *Comput. Phys. Commun.*, 69 (1992) 306-316.

[12] E. Hairer, C. Lubich, G. Wanner, Geometric Numerical Integration: Structure-Preserving Algorithms for Ordinary Differential Equations, Springer, (2006).

[13] J. Boris, in Proceedings of *the 4th Conf. on Numerical Simulation of Plasmas*, (1971) 3-67.

[14] J.-L. Vay, Simulation of beams or plasmas crossing at relativistic velocity, *Physics of Plasmas*, 15 (056701) (2008) .

[15] T. Esirkepov, Exact charge conservation scheme for particle-in-cell simulation with an arbitrary form-factor, *Comput. Phys. Commun.*, 135 (2) (2001) 144-153.

[16] D. Neuffer, Introduction to muon cooling, *Nuclear Instruments and Methods in Physics Research*, A 532 (2004) 26-31.

[17] J.-L. Vay, Noninvariance of space- and time- scale ranges under a Lorentz transformation and the implications for the study of relativistic interactions, *Phys. Rev. Lett.* 98 (130405) (2007).

[18] https://wci.llnl.gov/simulation/computer-codes/visit/

[19] https://www.mcs.anl.gov/petsc/

[20] J. Ma, Models and Algorithms for Interaction of Relativistic Particle Beams with Plasma and Applications to Accelerator Design, Preliminary Exam Report, Stony Brook University (2015).

[21] http://www.fftw.org/

[22] D. Cheng, Field and Wave Electromagnetics 2nd edition, *Addison Wesley*, (1989)

[23] D. R. Nicholson, Introduction to Plasma Theory, *John Wiley & Sons* (1983)

[24] A. Moretti, Z. Qian, J. Norem, Y. Torun, D. Li, M. Zisman, Effects of high solenoidal magnetic fields on rf accelerating cavities, *Phys. Rev. ST Accel. Beams*, 8 (072001) (2005).

[25] Ya.S. Derbenev and R. P. Johnson, *Six-dimensional muon beam cooling using a homogeneous absorber: Concepts, beam dynamics, cooling decrements, and equilibrium emittances in a helical dipole channe*, *Phys. Rev. ST - Accelerators and Beams*, 8 (041002) (2005)

[26] K. Yonehara, D. Kaplan, K. Beard, S.A. Bogacz, Y.S. Derbenev, R.P. Johnson, K. Paul, T.J. Roberts, Simulations of a Gas-Filled Helical Muon Beam Cooling Channel, in Proceedings of *PAC 2005*, TPPP052.

[27] M. Chung, M. G. Collura, G. Flanagan, B. Freemire, P. M. Hanlet, M. R. Jana, R. P. Johnson, D. M. Kaplan, M. Leonova, A. Moretti, M. Popovic, T. Schwarz, A. Tollestrup, Y. Torun, K. Yonehara, Pressurized H_2 rf cavities in ionizing beams and magnetic fields, *Phys. Rev. Lett.*, 111 (184802) (2013).

[28] B. Freemire, High pressure gas filled rf cavity beam test at the fermilab mucool test area, *Doctoral Thesis*, Illinois Institute of Technology (2013).

[29] K. Yonehara, M. Chung, M. Jana, M. Leonova, A. Moretti, A. Tollestrup, R. Johnson, B. Freemire, Y. Torun, P. Hanlet, Summary of dense hydrogen gas filled rf cavity tests for muon acceleration, in Proceedings of *IPAC 2013*, TUPFI059.

[30] K. Yu, R. Samulyak, SPACE code for beam-plasma interaction, in Proceedings of *IPAC 2015*, MOPMN012.

[31] S. Holmes, The Physics of Muon Cooling for a Neutrino Factory, *Doctoral Thesis*, University of Oxford (2006).

[32] B. Freemire et al., Beam induced plasma dynamics in a high pressure gas-filled rf test cell for use in a muon cooling channel, in Proceedings of *IPAC 2013*, TUPFI064.

[33] K. Yu, R. Samulyak, M. Chung, A. Tollestrup, K. Yonehara, B. Freemire, Modeling and simulation of beam-induced plasma in muon cooling devices, in Proceedings of *IPAC 2014*, MOPME043.

[34] K. Yonehara, Simulation of Gas Plasma Distribution in High Pressure Gas Filled RF Test Cell, Version 6 (Unpublished), Sept. (2012).

[35] K. Nakamura et al. (Particle Data Group), The Review of Particle Physics, *J. Phys. G*, 37 (075021) (2010).

[36] R. Grünberg, *Z. Physik*, 204 (2) (1967).

[37] J.J. Lowke, *The drift velocity of electrons in hydrogen and nitrogen*, *Aust. J. Phys.*, 16 (1962) 115-135.

[38] E. W. McDaniel and H. R. Crane, Measurements of the mobilities of the negative ions in oxygen and in mixtures of oxygen with the noble gases, hydrogen, nitrogen, and carbon dioxide, *Rev. Sci. Instrum.*, 28 (1957) 684-689.

[39] E. A. Mason and J. T. Vanderslice, Mobility of Hydrogen Ions (H^+, H_2^+, H_3^+) in Hydrogen, *Phys. Rev.*, 114 (497) (1959).

[40] K. Yonehara et al., Influence of intense beam in high pressure hydrogen gas filled rf cavities, in Proceedings of *IPAC 2012*, MOPPC036.

[41] B. Freemire, Y. Torun, M. Chung, M. Jana, M. Leonova, A. Moretti, T. Schwarz, A. Tollestrup, K. Yonehara, R. Johnson, Plasma chemistry in a high pressure gas filled rf test cell for use in a muon cooling channel, in Proceedings of *IPAC 2014*, THPRI064.

[42] V.N. Litvinenko, Y.S. Derbenev, Coherent Electron Cooling, *Phys. Rev. Lett.*, 102 (114801) (2009).

[43] V. N. Litvinenko, Y. S. Derbenev, Free Electron Lasers and High-Energy Electron Cooling, in Proceedings of the *FEL07*, BNL-79509-2007-CP.

[44] V. N. Litvinenko, Coherent Electron Cooling, in Proceedings of *PAC09*, (FR1GRI01).

[45] G. Wang, M. Blaskiewicz, Dynamics of ion shielding in an anisotropic electron plasma, *Phys. Rev. E*, 78 (026413) (2008).

[46] G. Bell et al., Vlasov and PIC simulations of a modulator section for coherent electron cooling, in Proceedings of *PAC 2011*, MOP067.

[47] G. Wang et al., Energy Modulation in Coherent Electron Cooling, in Proceedings of *IPAC 2013*, MOPEA083.

[48] L. Deniau et al., MAD - Methodical Accelerator Design, CERN web page: http://mad.web.cern.ch/mad/.

[49] N. D'Imperio, C. Montag, K. Yu, V. Kapin, E. McIntosh, H. Renshall, F. Schmidt, Experience with OpenMP for MADX-SC, BNL-105538-2014-IR, (2014).

[50] http://www.quantum-espresso.org/